bioRxiv preprint doi: https://doi.org/10.1101/2020.11.23.394098; this version posted November 23, 2020. The copyright holder for this preprint (which was not certified by peer review) is the author/funder, who has granted bioRxiv a license to display the preprint in perpetuity. It is made available under aCC-BY 4.0 International license.

A novel, ataxic mouse model of Ataxia Telangiectasia caused by a clinically relevant nonsense mutation

Perez, Harvey [¥1]; Abdallah, May, F.[¥1]; Chavira, Jose, I. [¥1]; Egeland, Martin, T. [1]; Vo, Karen, L. [1]; Buechsenschuetz, Callan, L. [1]; Sanghez, Valentina [1]; Kim, Jeannie, L. [1]; Pind, Molly [2], Nakamura, Kotoka [3], Hicks, Geoffrey, G. [2]; Gatti, Richard, A. [3]; Madrenas, Joaquin [1,5]; Iacovino, Michelina [1,4]; McKinnon, Peter, J. [6]; Mathews, Paul, J. [*1,7]

1. *The Lundquist Institute for Biomedical Innovation, Harbor-UCLA Medical Center, Torrance, CA*
2. *Department of Biochemistry & Medical Genetics, Max Rady College of Medicine, University of Manitoba*
3. *Department of Pathology & Laboratory Medicine, David Geffen School of Medicine, University of California, Los Angeles, CA*
4. *Department of Pediatrics, Harbor-UCLA Medical Center, Torrance, CA*
5. *Department of Medicine, Harbor-UCLA Medical Center, Torrance, CA*
6. *Center for Pediatric Neurological Disease Research, St. Jude Translational Neuroscience, St. Jude Children's Research Hospital, Memphis, TN, USA*
7. *Department of Neurology, Harbor-UCLA Medical Center, Torrance, CA*

¥Contributed equally

**Corresponding Author*

Abstract

Ataxia Telangiectasia (A-T) is caused by null mutations in the genome stability gene, *ATM* (A-T mutated). In mice, similar null mutations do not replicate A-T's characteristic severe ataxia with associated cerebellar dysfunction and atrophy. By increasing genotoxic stress, through the insertion of null mutations in the *Atm* (nonsense) and related *Aptx* (knockout) genes, we have generated a novel A-T mouse that first develops mild ataxia, associated with abnormal Purkinje neuron (PN) activity and decreased size, progressing to severe ataxia correlated with further reduced PN activity as well as PN loss and overall cerebellar atrophy. These mice also exhibit high incidences of cancer and immune abnormalities that are all hallmarks of the human disorder. Enabled by the insertion of a clinically relevant nonsense mutation in *Atm*, we demonstrate that small molecule readthrough (SMRT) compounds can restore ATM production, indicating their potential as a future A-T therapeutic.

bioRxiv preprint doi: https://doi.org/10.1101/2020.11.23.394098; this version posted November 23, 2020. The copyright holder for this preprint (which was not certified by peer review) is the author/funder, who has granted bioRxiv a license to display the preprint in perpetuity. It is made available under aCC-BY 4.0 International license.

1.0 Introduction

Ataxia Telangiectasia (A-T) is a rare (1 in ~100,000) (Swift et al. 1986), autosomal recessive genetic disorder characterized by cancer predisposition, immune deficiency, and a progressive and severe ataxia linked to cerebellar atrophy (Rothblum-Oviatt et al. 2016; Levy and Lang 2018; Boder and Sedgwick 1958). A-T patients typically die by their third decade of life (Crawford et al. 2006) from lymphatic cancers, respiratory infections, or debilitating ataxia—unfortunately, survivability has not dramatically changed since the 1950s (Micol et al. 2011; Rothblum-Oviatt et al. 2016). While disease progression and cause of death vary widely across patients, the progressive decline in motor coordination is reported as having the greatest negative impact on a patient's quality of life (Jackson et al. 2016). Care is generally palliative, directed at reducing, limiting, or eliminating cancers or infections. No long-term therapies are available for treating the ataxia and associated cerebellar atrophy.

A-T is caused by deficiency or dysfunction of the ATM (AT mutated) protein (Savitsky et al. 1995). Premature termination codon (PTC) causing nonsense mutations account for over a third of known cases with missense and deletions also contributing (Concannon and Gatti 1997; Sandoval et al. 1999). ATM is a serine/threonine PIKK family kinase that is a key regulator of the DNA damage response (DDR), in particular, responding to double stranded DNA breaks (Kastan and Bartek 2004; Shiloh and Ziv 2013). In the active monomeric form, ATM phosphorylates several key proteins halting the production of new DNA (cell cycle arrest) (Ando et al. 2012), and then, depending on severity of the damage, initiating DNA repair or programmed cell death (apoptosis) (Ando et al. 2012; Rashi-Elkeles et al. 2006). Several downstream DDR pathway targets of ATM have been identified, including p53, CHK2, BRCA1, SMC1, and NBS1 (Matsuoka et al. 2007). ATM's role in DNA repair is also implicated in normal immune system development, where it is proposed to contribute to the recombination of natural DNA breaks that occur during gene rearrangement in T- and B-lymphocyte maturation (Chao, Yang, and Xu 2000; Matei, Guidos, and Danska 2006; Vacchio et al. 2007; Schubert, Reichenbach, and Zielen 2002). Although its roles are still emerging, ATM has also been implicated in oxidative stress homeostasis (Guo et al. 2010) and mitophagy (Valentin-Vega and Kastan 2012; Pizzamiglio, Focchi, and Antonucci 2020).

bioRxiv preprint doi: https://doi.org/10.1101/2020.11.23.394098; this version posted November 23, 2020. The copyright holder for this preprint (which was not certified by peer review) is the author/funder, who has granted bioRxiv a license to display the preprint in perpetuity. It is made available under aCC-BY 4.0 International license.

A mechanistic understanding of why ATM deficiency causes ataxia is still under debate, but it is far from the only DDR protein linked to ataxia, as aprataxin (APTX) (Aicardi et al. 1988), meiotic recombination 11 homolog 1 (MRE11) (Sedghi et al. 2018), nibrin (NBS1) (van der Burgt et al. 1996), senataxin (SETX) (Moreira et al. 2004), and tyrosyl-DNA phosphodiesterase 1 (TDP1) (Takashima et al. 2002) when absent or dysfunctional usually results in cerebellar related ataxia. This suggests that the neurological features of genome instability syndromes have a common underlying cause, although this idea is still to be clearly demonstrated (McKinnon 2009; Rass, Ahel, and West 2007).

Our understanding of why loss of DDR proteins like ATM selectively affect the cerebellum to cause ataxia has been considerably hampered by the lack of animal models that recapitulate the neurological symptoms (Lavin 2013). A number of A-T rodent models (Herzog et al. 1998; Xu and Baltimore 1996; Elson et al. 1996; Barlow et al. 1996; Spring et al. 2001; Campbell et al. 2015; Quek et al. 2016; Tal et al. 2018) as well as a porcine model (Beraldi et al. 2017) have been created by inserting gene mutations that cause protein dysfunction (lack kinase activity) or complete deficiency. Unfortunately, none develop an overt ataxic phenotype with marked cerebellar dysfunction and atrophy that recapitulates the human disease. This has severely limited experimental studies from identifying the cellular and molecular mechanisms by which DDR protein deficiency disrupts cerebellar function and atrophy.

We have created a novel mouse model that recapitulates the broadest set of A-T symptomology of any A-T animal model to date, this includes for the first time a progressive and severe ataxia along with cerebellar atrophy, a predisposition to cancer, and deficits in immune development. This model was created by using a double-hit strategy, whereby the mouse is deficient not only in ATM, but also the DDR protein APTX (aprataxin). As hypothesized, we found that deficiency in either ATM or APTX alone does not lead to an overtly ataxic phenotype (Lavin 2013; Ahel et al. 2006), whereas deficiency in both DDR genes resulted in mice that developed a progressive and profound ataxia. To improve the clinical relevance of the *Atm* null mutation over prior A-T knockout mice, we inserted a clinically relevant point mutation in the *Atm* gene (103C>T) that causes ATM deficiency due to the creation of a premature termination codon (PTC). Moreover, the expression of the primary PTC allowed us to demonstrate that

bioRxiv preprint doi: https://doi.org/10.1101/2020.11.23.394098; this version posted November 23, 2020. The copyright holder for this preprint (which was not certified by peer review) is the author/funder, who has granted bioRxiv a license to display the preprint in perpetuity. It is made available under aCC-BY 4.0 International license.

a clinically related nonsense mutation in the A-T gene can be overcome by therapeutics capable of enabling readthrough of PTCs. This includes the Small Molecule Readthrough (SMRT) compound we have developed (Du et al. 2013).

2.0 Results

2.1 Creation of a new AT mutant mouse model expressing a clinically relevant nonsense mutation

To create a more clinically relevant mouse model of A-T we used a gateway recombination cloning and site-directed mutagenesis method to recapitulate a c.103C>T (p.R35X) mutation in the *ATM* gene found in a large population of North African A-T patients (**Fig. 1A and Methods**) (Gilad et al. 1996). The insertion of thymine in place of cytosine at this site in exon 3 results in a premature termination codon (PTC) causing nonsense mutation in the ATM gene. Since the 103C>T mutation results in different PTCs in the human compared to the mouse *Atm* gene, TGA *vs.* TAG respectively, we created two different mice by exchanging the mouse *Atm* exon 3 with either a human or mouse exon 3 variant with the 103C>T mutation (**Fig. 1B**). In the human version, a 103 CAG>TGA mutation of the mouse codon, where the arginine (R) encoding codon becomes a TGA stop codon, results in a mouse we denote as Atm^{R35X}. In the mouse version, the 103C>T mutation transforms a glutamine (Q) encoding CAG codon into a TAG stop codon and is denoted Atm^{Q35X}. The presence of the PTC results in a loss of ATM expression, either partially in the heterozygote, or completely in the homozygote (**Fig. 1C**).

Like prior ATM deficient A-T mouse models, neither the Atm^{R35X} nor Atm^{Q35X} mice develop a severe, progressive ataxia, a hallmark characteristic of the human disease (**Video S1**). We therefore exploited a double-hit strategy to increase genotoxic stress by eliminating expression of an additional DNA repair pathway protein, specifically APTX, in order to overcome the apparent compensation for ATM deficiency in mice. APTX deficiency alone in humans results in the disorder ataxia with ocular apraxia type 1 (AOA-1). In mice, ATM or APTX deficiency alone <u>does not</u> result in mice with an ataxic phenotype (**Video S1 and S2**). However, deficiency in both proteins, as in the $Atm^{R35X/R35X}$; $Aptx^{-/-}$ mouse results in the development of a severe and progressively ataxic phenotype (**Video S3 and S4**).

bioRxiv preprint doi: https://doi.org/10.1101/2020.11.23.394098; this version posted November 23, 2020. The copyright holder for this preprint (which was not certified by peer review) is the author/funder, who has granted bioRxiv a license to display the preprint in perpetuity. It is made available under aCC-BY 4.0 International license.

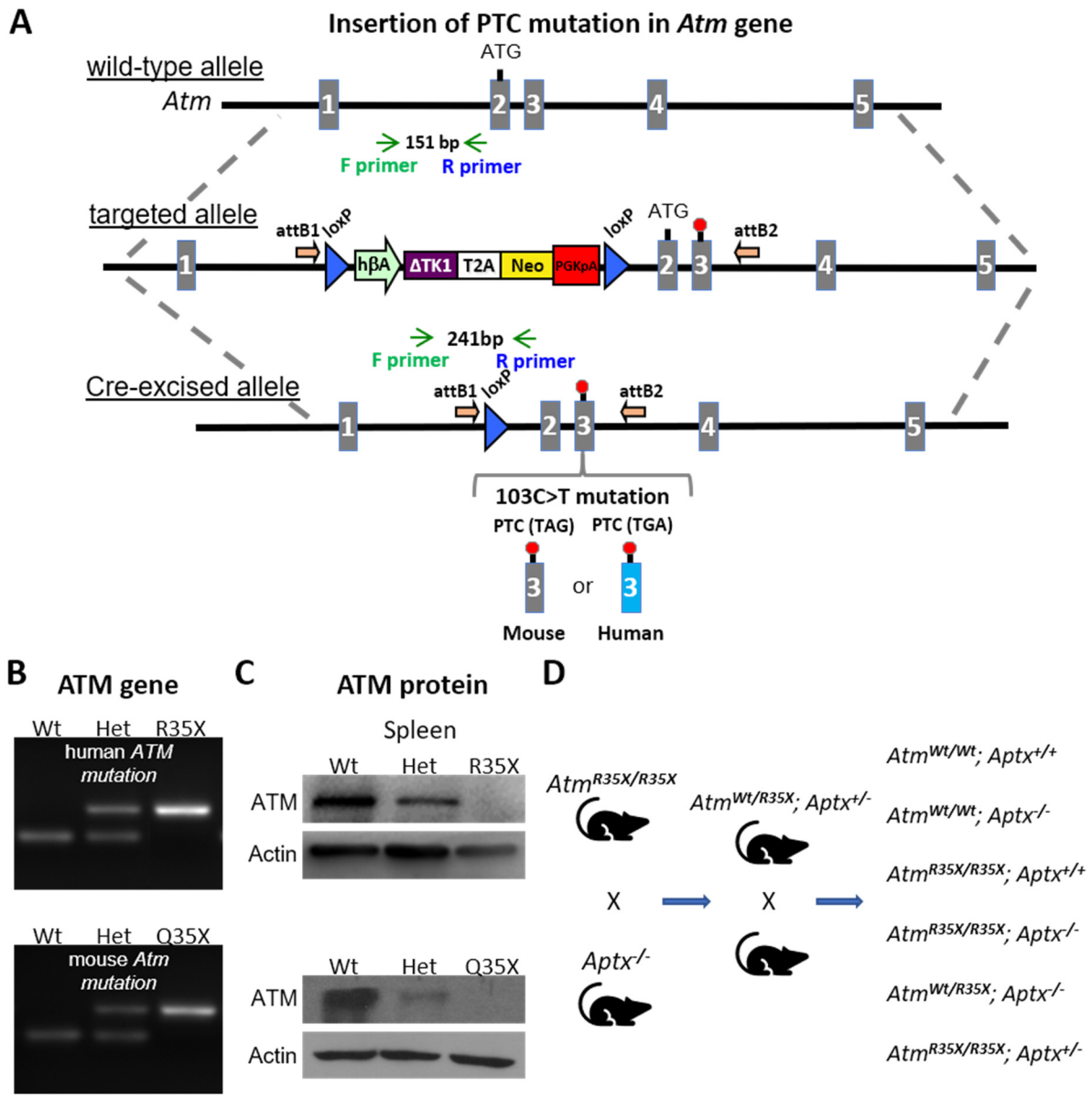

Figure 1. New A-T mouse models expressing clinically related PTCs. A) The *Atm* gene locus was targeted by homologous recombination of a targeting vector containing a modified NorCOMM cassette in intron one and the corresponding A-T PTC mutation in exon 3 to create the targeted Atm^{R35X} and Atm^{Q35X} ES cell lines. Following germline transmission of these alleles in mice, the floxed NorCOMM cassette was removed by Cre excision *in vivo* to produce the final Atm^{R35X} and Atm^{Q35X} mouse lines. **B)** Genotyping of AT mouse models. PCR agarose gel of mouse DNA shows 151 bp wt allele band and 241 bp Cre-excised targeted allele band. **C)** ATM immunoblot analyses from the indicated tissues in wildtype (Wt), heterozygous (het), and homozygous Atm^{R35x} Atm^{Q35X} mice shows a gene dose effect of ATM protein expression. **D)** Breeding scheme schematic for double mutant and control mice for this study. **hβA**: human beta Actin promotor. Δ**TK1**: delta TK1, inactivated Thymidine Kinase 1. **T2A**: self-cleaving peptide sequence. **Neo**: Neomycin gene. **PGKpA**: Phosphoglycerate kinase poly A tail. **loxP** recombination elements are show as a blue triangle, orientation of the Gateway **attB** recombination elements by an orange arrow, orientation of the genotyping **F** and **R** primers is shown by green and blue arrows respectively, and engineered PTC sites are shown in exon 3 by a red stop sign.

bioRxiv preprint doi: https://doi.org/10.1101/2020.11.23.394098; this version posted November 23, 2020. The copyright holder for this preprint (which was not certified by peer review) is the author/funder, who has granted bioRxiv a license to display the preprint in perpetuity. It is made available under aCC-BY 4.0 International license.

Atm$^{R35X/R35X}$; *Aptx*$^{-/-}$ mice were created by first crossing single mutant *Atm*$^{R35X/R35X}$ (congenic on the C57BL/6J background) and *Aptx*$^{-/-}$ (mixed C57BL/6J and 129 background) mice to generate double mutant heterozygote *Atm*$^{R35X/Wt}$; *Aptx*$^{-/+}$ mice. F1-5 littermate *Atm*$^{R35X/Wt}$; *Aptx*$^{-/+}$ mice were then crossed within litters to create sufficient numbers of the desired experimental and control genotypes to understand how loss of ATM and APTX affects the animal's phenotype (**Fig. 1D**). We found both male and female *Atm*$^{R35X/R35X}$ and *Atm*$^{Q35X/Q35X}$ mice to be reproductive, indicating functional reproductive systems.

2.2 ATM deficient mice have lowered survivability and a high incidence of thymic cancer

We assessed the general health and development of control and experimental mice expressing different levels of ATM and APTX (**Fig. 2**). We found that *Atm*$^{R35X/R35X}$; *Aptx*$^{-/-}$ mice grew ~55% slower and reached estimated plateau weights that were ~35% less than control genotypes (log-rank, $p<0.0001$; **Fig. 2A**). These differences in weight are a postnatal phenomenon, as no significant weight differences were detected just after birth (P8) across all genotypes [1-way ANOVA, $p>0.23$]. Adolescent double mutant mice at postnatal day 45 (P45) weighed on average 30% less in males [double mutant: 14.4±1.0 g *vs.* wildtype: 20.2 ± 0.5 g, t-test, $p < 0.0001$] and 25% less in females [double mutant: 12.7 ± 0.6 g *vs.* wildtype: 17.0 ± 0.2 g, t-test, $p < 0.0001$; **Fig. 1A**]. Differences across the control genotypes were observed, but they were small and not consistent across time points or sex and therefore judged to not be physiologically relevant (**Fig. 2A**).

Survivability of the *Atm*$^{R35X/R35X}$; *Aptx*$^{-/-}$ mice was significantly reduced compared to *Atm*$^{Wt/Wt}$; *Aptx*$^{+/+}$ mice, with 53% of mice still alive at 400 days of age, compared to 97% of *Atm*$^{Wt/Wt}$; *Aptx*$^{+/+}$ mice at the same time point (**Fig. 2B**). ATM deficiency alone was sufficient to reduce survivability, as compared to *Atm*$^{Wt/Wt}$; *Aptx*$^{+/+}$ mice, both *Atm*$^{R35X/R35X}$; *Aptx*$^{+/+}$ and *Atm*$^{R35X/R35X}$; *Aptx*$^{-/+}$ mice had significantly reduced survivability rates [42%, log-rank, $\chi^2_{(1,\ 56)} = 13.49$, $p=0.0002$ and 52%, log-rank, $\chi^2_{(1,\ 53)} = 19.54$, $p<0.0001$, respectively]. No significant difference between ATM deficient mice with partial or complete APTX deficiency was detected [log-rank, $\chi^2_{(2,\ 85)} = 1.01$, $p = 0.6$]. Conversely, mice harboring at least one functional copy of the *Atm* gene had survivability like *Atm*$^{Wt/Wt}$; *Aptx*$^{+/+}$ mice, regardless of whether they expressed APTX or not [log-rank, $\chi^2_{(3,\ 131)} = 3.08$, $p=0.4$]. No significant difference between male and

bioRxiv preprint doi: https://doi.org/10.1101/2020.11.23.394098; this version posted November 23, 2020. The copyright holder for this preprint (which was not certified by peer review) is the author/funder, who has granted bioRxiv a license to display the preprint in perpetuity. It is made available under aCC-BY 4.0 International license.

female mice was observed and thus data were pooled [log-rank, p>0.4 for all pairwise comparisons; **Fig. 2-fig. S1B**]. Generally, a third of mice with ATM deficiency died from complications related to large thymic cancers found in the thoracic cavity (**Fig. 2C**). The presence or absence of APTX did not impact cancer prevalence, and mice with at least one *Atm* transcript were cancer free up until at least P400. Overall, ATM, but not APTX deficiency had severe effects on the health and survivability of the examined mice.

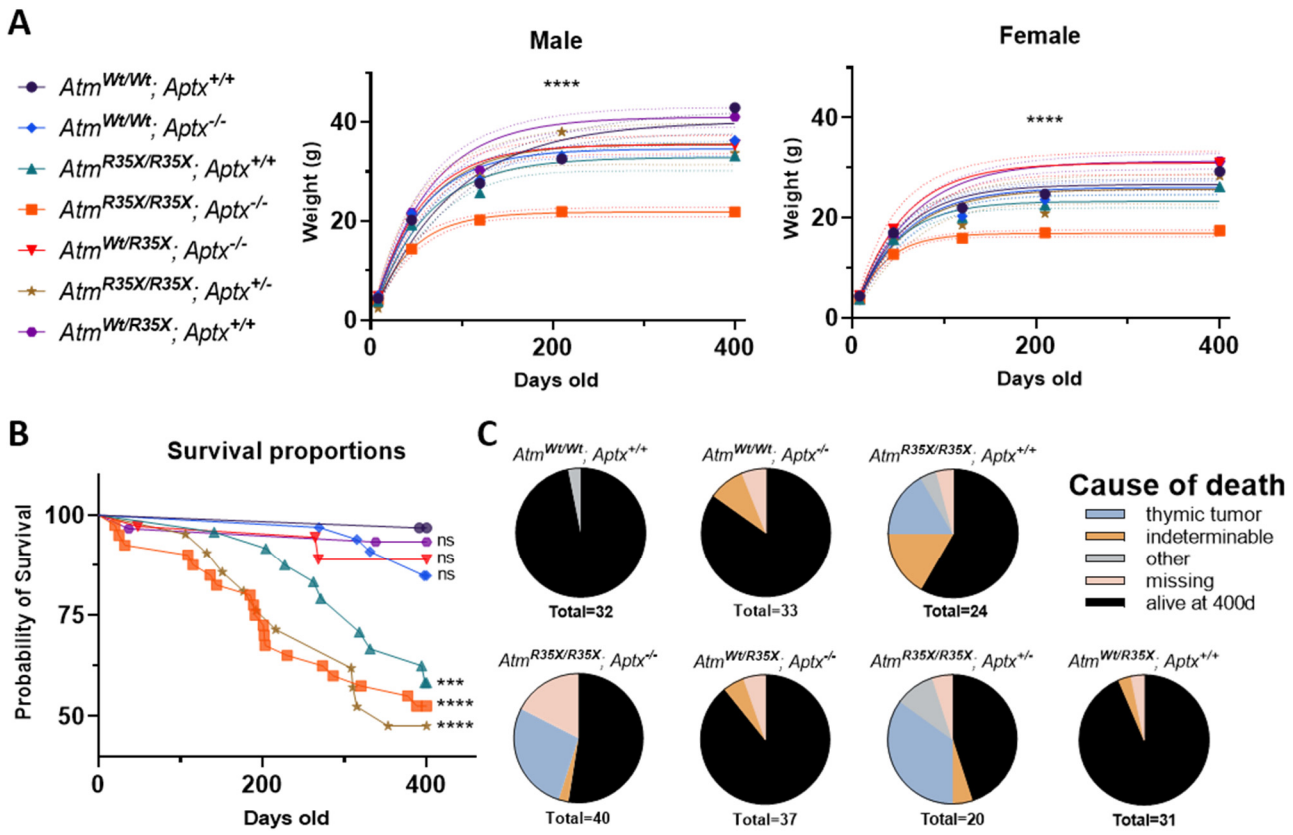

Figure 2. Health and survivability of single and double mutant mice. A) (left) The line color and symbol for each genotype is denoted and is consistent across all figures (1-7). (right) *Atm*$^{R35X/R35X}$*; Aptx*$^{-/-}$ mice weigh significantly less than the control genotypes as shown by the growth curves (solid line) along with the 95% confidence interval (dotted line). Growth curve (*Atm*$^{R35X/R35X}$*; Aptx*$^{-/-}$ *vs.* controls): Male k = 0.024 *vs.* 0.011-0.019, Y_{max} = 21.8 *vs.* 32.9-41.0 g, (n=3-18); Female k = 0.030 *vs.* 0.017-0.022, Y_{max} = 16.9 *vs.* 23.3-31.3, (n=2-19). Sum of squares F-test run across all curves: Male $F_{(12, 364)}$ = 30.5, ****p<0.0001, Female $F_{(12, 339)}$ = 28.3, ****p<0.0001. **B)** ATM deficient mice, regardless of APTX expression displayed significantly lower survivability with ~55% of mice deceased by P400. Mice heterozygous for the R35X mutation (*Atm*$^{R35X/Wt}$*; Aptx*$^{-/-}$) gene had similar survivability to wildtype (*Atm*$^{Wt/Wt}$*; Aptx*$^{+/+}$) mice. Log-rank (Mantel-Cox) tests across all ($\chi^2_{(6, 217)}$ = 48.4, ****$p<0.0001$) and single comparisons to wildtype (see figure) were conducted. Total number of animals indicated in panel **C**. **C)** ATM deficient mice displayed a high prevalence of thymic tumors based on postmortem necropsies. Other probable causes of death included enlarged livers, and obstructed kidneys. **Figure 2-figure supplement 1, Figure 2-Source Data 1**

bioRxiv preprint doi: https://doi.org/10.1101/2020.11.23.394098; this version posted November 23, 2020. The copyright holder for this preprint (which was not certified by peer review) is the author/funder, who has granted bioRxiv a license to display the preprint in perpetuity. It is made available under aCC-BY 4.0 International license.

2.3 ATM *and* APTX deficiency is necessary to produce progressive motor dysfunction

The progressive development of severe ataxia is a hallmark characteristic of A-T that is recapitulated in the *Atm*$^{R35X/R35X}$; *Aptx*$^{-/-}$ mice but none of the other control genotypes we tested. Overall, we find motor coordination deficits emerge between 210 and 400 days after birth in *Atm*$^{R35X/R35X}$; *Aptx*$^{-/-}$ mice and find no evidence of ataxia in mice with at least some ATM or APTX expression (**Fig. 3A, B**). For the vertical pole test, *Atm*$^{R35X/R35X}$; *Aptx*$^{-/-}$ mice took twice as long to descend at P400 compared to *Atm*$^{Wt/Wt}$; *Aptx*$^{+/+}$, *Atm*$^{Wt/Wt}$; *Aptx*$^{-/-}$, *Atm*$^{R35X/R35X}$; *Aptx*$^{+/+}$, or *Atm*$^{Wt/R35X}$; *Aptx*$^{-/-}$ mice [Male: 29.1±0.9 (n=3) *vs.* 7.5±0.4 (n=12), 12.5±2.5 (n=9), 9.2±0.9 (n=10), 8.6±0.9 (n=11) sec, 1-way ANOVA, $F_{(4, 40)}$ = 19.9, *p<0.0001*; Female: 19.0±4.0 (n=4) *vs.* 7.5±0.4 (n=12), 7.8±0.4 (n=10), 10.5±1.2 (n=6), 8.2±0.5 sec, 1-way ANOVA, $F_{(4, 35)}$ = 13.9; *p*<0.0001]. An examination of gait indicated that *Atm*$^{R35X/R35X}$; *Aptx*$^{-/-}$ mice at P400, but not P210 need additional stabilization during ambulation, as they spend twice as much time with 3 paws, rather than the normal 2 in contact with the ground as they walk across the gait analysis platform [Male: 56.2 *vs.* 26.4-32.2 %, 1-way ANOVA, $F_{(4, 54)}$ = 14.3, *p*<0.0001; Female: 58.4 *vs.* 18.9-28.8 %, 1-way ANOVA, $F_{(3, 178)}$ = 95.5, *p<0.0001*; **Fig. 3B**]. *Atm*$^{R35X/R35X}$; *Aptx*$^{-/-}$ also display a slower cadence and average speed across the platform compared to all other genotypes at P400 [cadence, Male: 9.5 *vs.* 13.3-15.9 steps/s, 1-way ANOVA, $F_{(3, 204)}$ = 36.8, *p<0.0001*; Female: 9.1 *vs.* 14.2-15.9 steps/s, 1-way ANOVA, $F_{(3, 204)}$ = 39.7, *p<0.0001*; speed, Male: 8.8 *vs.* 22-26 cm/s, 1-way ANOVA, $F_{(4, 50)}$ = 28.3 *p<0.0001*; Female: 58.4 *vs.* 18.9-28.8 cm/s, 1-way ANOVA, $F_{(3, 178)}$ = 39.7, *p<0.0001*; **Fig. 3B**]. This difference in speed and cadence is unlikely due to animal size, as there are no significant differences in these parameters at earlier time points when the difference in size is nominal (**Fig. 2A**). These observations across the two behavioral tests were found in both male and female mice at each of their respective time points, consistent with the lack of sex differences observed in A-T patients.

We further examined behavioral differences between the *Atm*$^{R35X/R35X}$; *Aptx*$^{-/-}$ and *Atm*$^{Wt/Wt}$; *Aptx*$^{+/+}$ mice using a standardized set of experimental procedures used to phenotype genetically modified mice (i.e., SHIRPA; **Fig. 3C**; **Fig. 3-fig. S1**) (Rogers et al. 1997). We first detected differences in motor function at P8, where *Atm*$^{R35X/R35X}$; *Aptx*$^{-/-}$ mice took 3-4 times longer on average to right themselves compared to *Atm*$^{Wt/Wt}$; *Aptx*$^{+/+}$ mice [Male: 6.4±1.1 s (n=24) *vs.* 1.5±0.1 s (n=23), t-test, *p<0.0002*; Female: 11.1±1.9 s

bioRxiv preprint doi: https://doi.org/10.1101/2020.11.23.394098; this version posted November 23, 2020. The copyright holder for this preprint (which was not certified by peer review) is the author/funder, who has granted bioRxiv a license to display the preprint in perpetuity. It is made available under aCC-BY 4.0 International license.

166 (n=21) *vs.* 2.4±0.3 s (n=17), t-test, *p<0.0002*; **Fig. 3C bottom**]. At 30-days of age, we detected significant

167 differences between *Atm*$^{R35X/R35X}$; *Aptx*$^{-/-}$ and *Atm*$^{Wt/Wt}$; *Aptx*$^{+/+}$ mice in behavioral tests that qualitatively

168 measure body position and spontaneous activity (**Fig. 3C**). Striking differences in *Atm*$^{R35X/R35X}$; *Aptx*$^{-/-}$

169 compared to *Atm*$^{Wt/Wt}$; *Aptx*$^{+/+}$ mice were observed at P400, especially for behaviors related to movement,

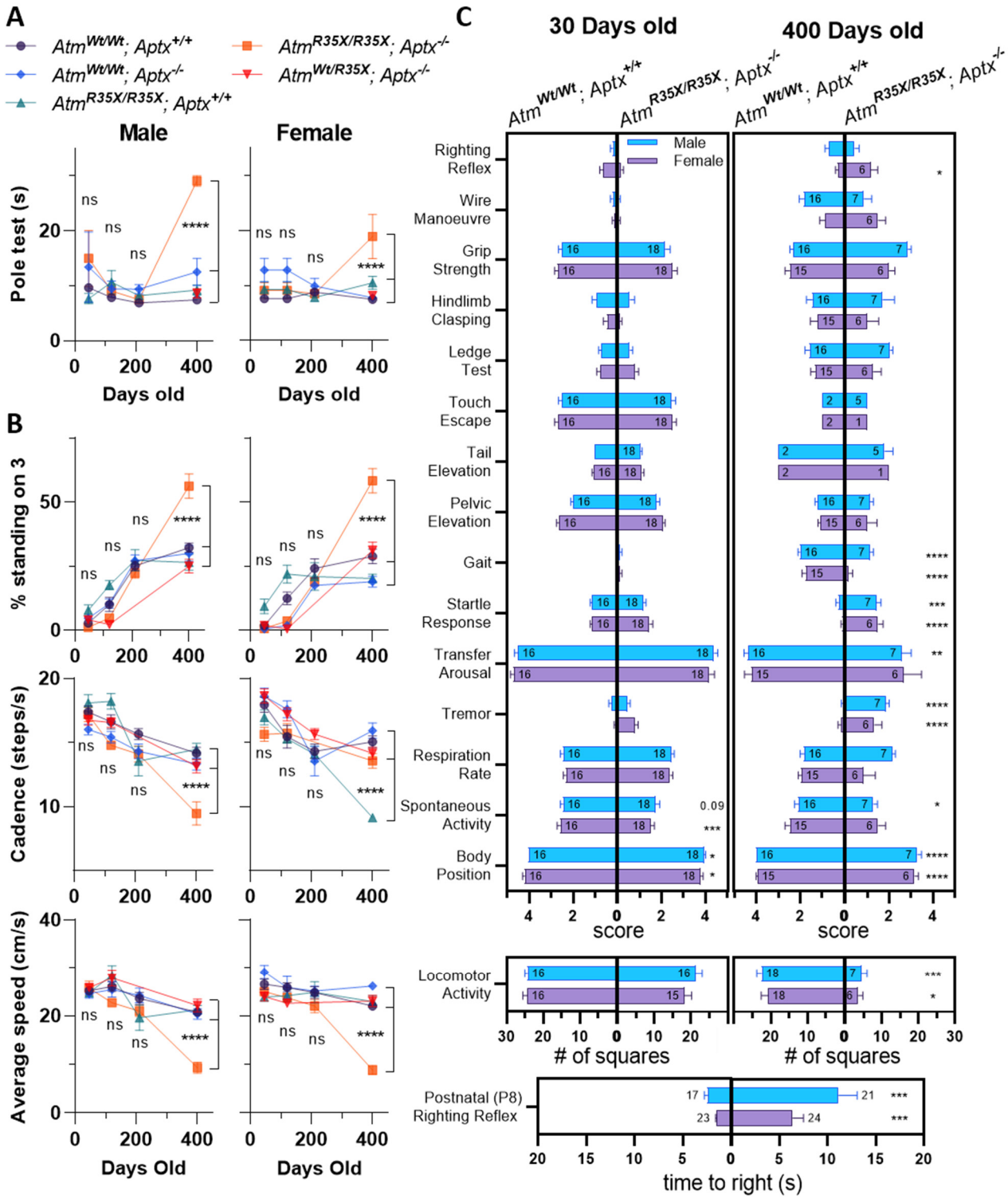

bioRxiv preprint doi: https://doi.org/10.1101/2020.11.23.394098; this version posted November 23, 2020. The copyright holder for this preprint (which was not certified by peer review) is the author/funder, who has granted bioRxiv a license to display the preprint in perpetuity. It is made available under aCC-BY 4.0 International license.

Figure 3. *Atm$^{R35X/R35X}$; Aptx$^{-/-}$* mice develop a progressive loss in motor coordination. A) *Atm$^{R35X/R35X}$; Aptx$^{-/-}$* take a similar amount of time to descend a vertical pole at P45, 120, and 210, but significantly longer at P400. These overall results were found to be similar for both male (left, n=2-12) and female (right, n=4-12) mice. **B)** Consistent with the vertical pole test, the gait of *Atm$^{R35X/R35X}$; Aptx$^{-/-}$* mice measured during ambulation on a Catwalk gait analysis system was significantly different to controls by P400, but not before P210. This includes the percent of time a mouse spends with 3 *vs.* 1, 2, or 4 paws on the ground and the speed and cadence during each run across the platform. The effects of the two null mutations were generally similar between males (left, n=4-21) and females (right, n=3-18). **C)** *Atm$^{R35X/R35X}$; Aptx$^{-/-}$* (left) and *Atm$^{Wt/Wt}$; Aptx$^{+/+}$* (right) at P30 and 400. Again, Male and Females performed similarly. A significant difference in the time to right during the righting reflex at P8 was observed in both Male and Female mice (bottom). **A** and **B** were examined via two-way ANOVA with age and genotype as factors followed by *potshot* Tukey's multiple comparison tests between *Atm$^{R35X/R35X}$; Aptx$^{-/-}$* and each of the control genotypes. Behavioral tests in **C** were examined using a non-parametric Kruskal Wallace followed by *postdocs* Dunn's multiple comparisons tests. Symbol/color key: *Atm$^{Wt/Wt}$; Aptx$^{+/+}$* (purple circle), *Atm$^{Wt/Wt}$; Aptx$^{-/-}$* (blue diamond), *Atm$^{R35X/R35X}$; Aptx$^{+/+}$* (green triangle), *Atm$^{R35X/R35X}$; Aptx$^{-/-}$* (orange square), *Atm$^{Wt/R35X}$; Aptx$^{-/-}$* (red inverted triangle) **Figure 3-figure supplement 1, Figure 3-Source Data 1**

including locomotor activity, body position, and gait (**Fig. 3C**). The results from this battery of tests demonstrates that *Atm$^{R35X/R35X}$*; *Aptx$^{-/-}$* mice develop a severe change in behavior, especially in those related to motor function, by P400, consistent with purely visual observations of significant motor coordination deficits in the mice at this time point. Importantly, we do not find any significant differences between the other control genotypes, including *Atm$^{Wt/R35X}$*; *Aptx$^{-/-}$* mice that express at least some ATM but no APTX protein (**Fig. 3-fig. S1**).

2.4 ATM and APTX deficiency is necessary to disrupt cerebellar neural physiology

Ataxia in A-T is thought to result from cerebellar dysfunction; however, the progression and underlying mechanism is unclear. Decreased spontaneous action potential firing rates in cerebellar Purkinje neurons (PN) has been linked to several forms of heritable ataxia (Cook, Fields, and Watt 2020). We therefore sought to determine if PN action potential firing rates in *Atm$^{R35X/R35X}$*; *Aptx$^{-/-}$* are abnormally low compared to control mice. We extracellularly recorded action potentials from 3,300 PNs (**Fig. 4A**), across 188 animals, encompassing *Atm$^{R35X/R35X}$*; *Aptx$^{-/-}$* and 3 other genotypes at 4 different time points (P45, 120, 210, and 400). Recordings were distributed across the lateral, intermediate and medial (vermis) cerebellum of each mouse.

bioRxiv preprint doi: https://doi.org/10.1101/2020.11.23.394098; this version posted November 23, 2020. The copyright holder for this preprint (which was not certified by peer review) is the author/funder, who has granted bioRxiv a license to display the preprint in perpetuity. It is made available under aCC-BY 4.0 International license.

PN spontaneous firing frequency, averaged across all age groups was significantly lower in *Atm*$^{R35X/R35X}$; *Aptx*$^{-/-}$ compared to *Atm*$^{Wt/Wt}$; *Aptx*$^{+/+}$ mice (**Fig. 4B**). The largest differences were detected in the anterior [38.6±3.4 Hz (n=187) *vs.* 88.1±1.8 Hz (n=222)] and posterior [46.9±1.9 Hz (n=175) *vs.* 84.1±2.4 Hz (n=219)] medial cerebellum [1-way ANOVA, *p<0.0001;* **Fig. 4B**]. Significant age dependent changes in firing frequency were only observed in *Atm*$^{R35X/R35X}$; *Aptx*$^{-/-}$ mice, especially within the medial cerebellum (**Fig. 4C**). The most significant decline occurring between P120 and 210 [anterior: 52.3±3.6 Hz (n=61) *vs*. 38.6±3.2 Hz (n=31), 1-way ANOVA, *p=0.015*; posterior: 48.4±3.1 Hz (n=63) *vs.* 34.8±3.2 Hz (n=25), 1-Way ANOVA, *p=0.012*]. Moreover, we determined that age-dependent changes in PN activity in the *Atm*$^{R35X/R35X}$; *Aptx*$^{-/-}$ mice were not equally expressed across the cerebellum, with the most pronounced effects in lobules III, VI, VIII, and X (linear regression, *p<0.05* for each folia; **Fig. 4-figs. S1, S2**). No significant difference in PN firing frequency was detected between male and female mice within each genotype, thus the data were pooled (2-way ANOVA, *p>0.*3 across all pairwise comparisons; **Fig. 4-fig. S3**). Previous studies in mouse models of heritable ataxia indicate that physiological disruption in PN firing not only includes changes in frequency but also affects its regularity (Cook, Fields, and Watt 2020). We compared both the coefficient of variation (CV) and variability in adjacent intervals (CV2) between *Atm*$^{R35X/R35X}$; *Aptx*$^{-/-}$ and control mice (**Fig. 4-figs. S4, S5**). No difference in these parameters across sex, age, or genotype was detected. Consistent with the behavioral results, cerebellar dysfunction was found only in the *Atm*$^{R35X/R35X}$; *Aptx*$^{-/-}$ mice that developed ataxia and not in mice with at least some expression of ATM or APTX.

2.5 ATM and APTX deficiency is necessary to induce cerebellar degeneration

Cerebellar atrophy is a characteristic A-T feature that is absent in other A-T deficient mouse models. We therefore assessed the developmental progression of cerebellar atrophy in the *Atm*$^{R35X/R35X}$; *Aptx*$^{-/-}$ mice. Structural changes in the overall size of the cerebellum were examined in *Atm*$^{R35X/R35X}$; *Aptx*$^{-/-}$ and control mice over 5 time points (P45, 120, 210, 400, 460; **Fig. 4D**). Cerebellar size was defined within each animal by the ratio of 2-dimensional surface area of the dorsal cerebellum to the forebrain (i.e., cerebellum area divided by forebrain area). The cerebellar size of control mice slightly increased during adolescence and early adulthood (P45-P210), was generally stable through adulthood (P210-400), and

bioRxiv preprint doi: https://doi.org/10.1101/2020.11.23.394098; this version posted November 23, 2020. The copyright holder for this preprint (which was not certified by peer review) is the author/funder, who has granted bioRxiv a license to display the preprint in perpetuity. It is made available under aCC-BY 4.0 International license.

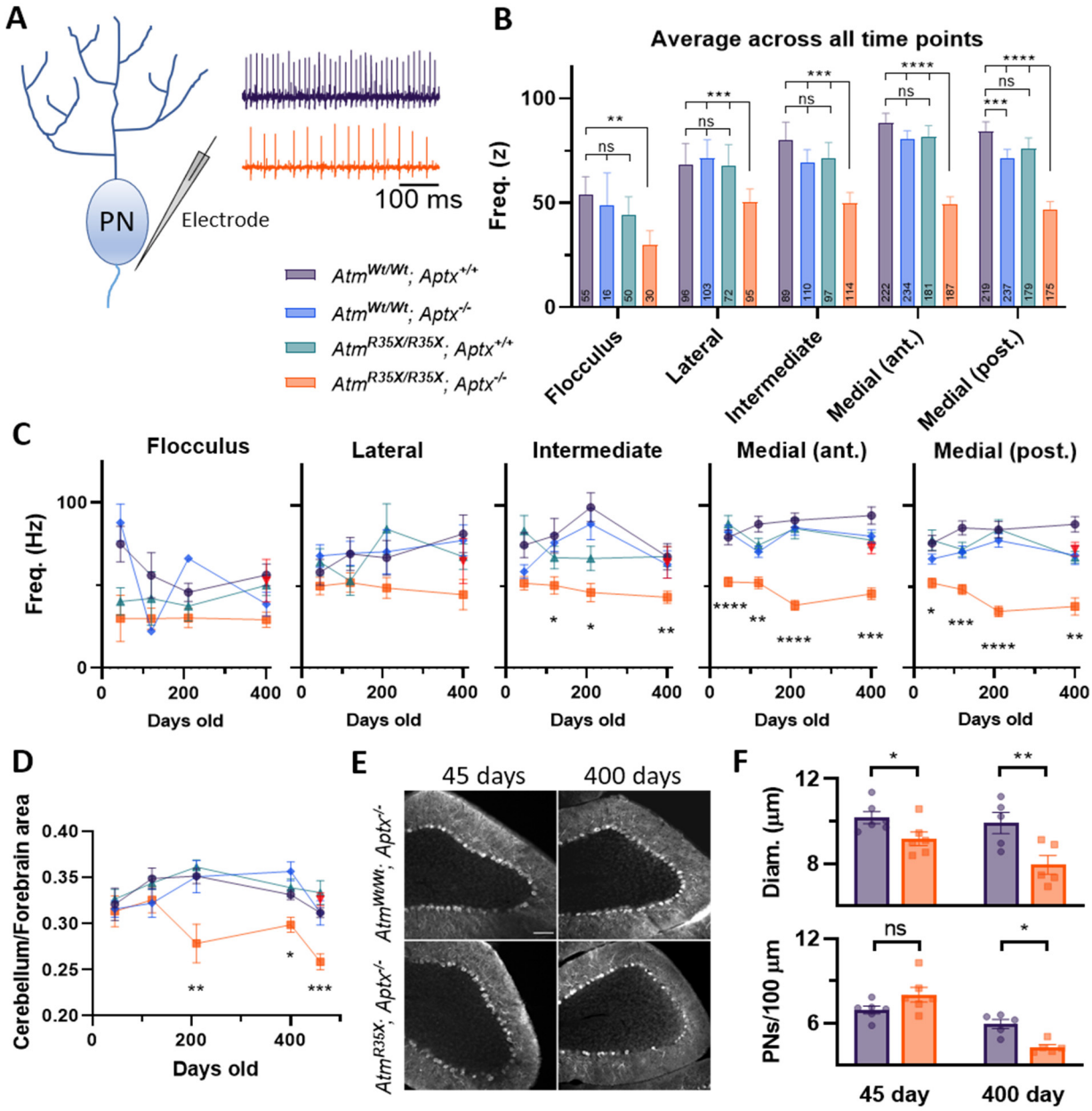

Figure 4. A reduction in PN firing rate, density, and size is associated with cerebellar atrophy in *Atm*$^{R35X/R35X}$; *Aptx*$^{-/-}$ mice. A) Schematic diagram of extracellular recording from a single Purkinje neuron (PN) in an acute cerebellar tissue slice preparation. Example electrophysiological traces for *Atm*$^{Wt/Wt}$; *Aptx*$^{+/+}$ (purple, top) and *Atm*$^{R35X/R35X}$; *Aptx*$^{-/-}$ (orange, bottom) PNs in the medial (vermis) area of the cerebellum. **B)** *Atm*$^{R35X/R35X}$; *Aptx*$^{-/-}$ PN action potential firing frequencies were significantly slower compared to all control genotypes. Number of animals denoted at bottom of bar. Medial: ant. (lobules II-V), post. (lobules VI-IX) **C)** Action potential spiking frequency was compared across genotypes and for each anatomical subdivision. **D)** The size of the cerebellum decreased over age in *Atm*$^{R35X/R35X}$; *Aptx*$^{-/-}$ (n=5-10), but not control mice [*Atm*$^{Wt/Wt}$; *Aptx*$^{+/+}$ (n=4-20), *Atm*$^{Wt/Wt}$; *Aptx*$^{-/-}$ (n=4-12), *Atm*$^{R35X/R35X}$; *Aptx*$^{+/+}$ (n=6-16), *Atm*$^{Wt/R35X}$; *Aptx*$^{-/-}$ (n=6)]. 2-dimensional area estimates from dorsal images of the brain were used to determine forebrain and cerebellar area and the cerebellar to forebrain ratio is reported. **E)** Immunofluorescent images of *Atm*$^{Wt/Wt}$; *Aptx*$^{+/+}$ (top) and *Atm*$^{R35X/R35X}$; *Aptx*$^{-/-}$ (bottom) at P45 and 400 (cerebellar lobule VIII). Scale bar = 100 um **F)** PN numbers (top) and soma diameter (bottom) in

212

bioRxiv preprint doi: https://doi.org/10.1101/2020.11.23.394098; this version posted November 23, 2020. The copyright holder for this preprint (which was not certified by peer review) is the author/funder, who has granted bioRxiv a license to display the preprint in perpetuity. It is made available under aCC-BY 4.0 International license.

Atm$^{Wt/Wt}$*; Aptx*$^{+/+}$ compared to *Atm*$^{R35X/R35X}$*; Aptx*$^{-/-}$ mice at P45 (n=6) and 400 (n=5). Statistical significances were assessed via 2-way ANOVA with age and genotype as factors followed by *posthoc* Holm-Sidak pairwise multiple comparisons test in **B**, **C**, and **D**. T-tests were used in **F.** Symbol/color key: *Atm*$^{Wt/Wt}$*; Aptx*$^{+/+}$ (purple circle), *Atm*$^{Wt/Wt}$*; Aptx*$^{-/-}$ (blue diamond), *Atm*$^{R35X/R35X}$*; Aptx*$^{+/+}$ (green triangle), *Atm*$^{R35X/R35X}$*; Aptx*$^{-/-}$ (orange square), *Atm*$^{Wt/R35X}$*; Aptx*$^{-/-}$ (red inverted triangle) **Figure 4-figure supplements 1-5, Figure 4-Source Data 1-3**

then declined slightly in older age (P400-460). In stark contrast, relative cerebellar size in *Atm*$^{R35X/R35X}$; *Aptx*$^{-/-}$ mice progressively declined after P120. We however did not find cerebellar atrophy in mice with some ATM expression [i.e., *Atm*$^{Wt/R35X}$; *Aptx*$^{-/-}$; 1-way ANOVA, $F_{(3,44)} = 1.2$, $p=0.32$]. To rule out the possibility that reduced cerebellar size was related to the smaller stature of *Atm*$^{R35X/R35X}$; *Aptx*$^{-/-}$ mice, we examined, but did not find a correlation between animal weight and actual cerebellar size [Pearson's correlation, $p>0.3$ for all 4 genotypes at P460, n=10-20]. Furthermore, we found that cerebellar size did not differ between male and the on average 22% smaller female mice across genotypes at this age [2-way ANOVA, $F_{(2, 153)} = 1.9$, $p=0.2$]. Therefore, cerebellar neurodegeneration in the *Atm*$^{R35X/R35X}$; *Aptx*$^{-/-}$ mice, which begins after P120, is correlated with ATM and APTX deficiency.

In humans, cerebellar atrophy is associated with PN loss (Gatti and Vinters 1985). At the pathohistological level, we found no difference in the linear density of *Atm*$^{R35X/R35X}$; *Aptx*$^{-/-}$ compared to *Atm*$^{Wt/Wt}$; *Aptx*$^{+/+}$ mice PNs at P45 [8.0 ± 0.5 *vs.* 6.9 ± 0.3 PNs/100 um, t-test, $p=0.9$], but did find PN diameter was significantly smaller [9.2 ± 0.3 *vs.* 10.2 ± 0.3 um, t-test, $p=0.04$; **Fig. 4E, F**]. At P400 however, the PN density [4.3 ± 0.2 *vs.* 5.9 ± 0.3 PNs/100 um, t-test, $p=0.003$] and diameter [8.0 ± 0.4 *vs.* 9.9 ± 0.5 um, t-test, $p=0.02$] are reduced in *Atm*$^{R35X/R35X}$; *Aptx*$^{-/-}$ compared to *Atm*$^{Wt/Wt}$; *Aptx*$^{+/+}$ mice (**Fig. 4E, F**). These data indicate that subtle changes in cerebellar function correlate well with mild deficits in motor behavior, but severe ataxia is associated with PN death and overall cerebellar atrophy.

2.6 Differential disruption of thymocyte development in ATM-deficient vs. APTX-deficient mice

Chronic sinopulmonary infections associated with immunodeficiency are one of the leading causes of death in A-T patients (Morrell, Cromartie, and Swift 1986; Bhatt and Bush 2014). Immunodeficiency is linked to deficits in the generation of B- and T-lymphocytes that have been linked to defects in the antigen receptor gene rearrangement processes during the generation of these cells in bone marrow and thymus, respectively (Staples et al. 2008). The resulting defects in mature lymphocyte numbers include decreases

bioRxiv preprint doi: https://doi.org/10.1101/2020.11.23.394098; this version posted November 23, 2020. The copyright holder for this preprint (which was not certified by peer review) is the author/funder, who has granted bioRxiv a license to display the preprint in perpetuity. It is made available under aCC-BY 4.0 International license.

236 in CD4⁺ helper T-cells and killer CD8⁺ T-cells (Schubert, Reichenbach, and Zielen 2002). We therefore
237 examined the percentages of T-cells in peripheral blood and of different subpopulations in the thymus of
238 $Atm^{R35X/R35X}$; $Aptx^{-/-}$ mice using T-cell antigen receptor (TCR) and CD4/CD8 co-receptor expression.

239 In the peripheral blood, we observed a significant reduction in the total fraction of CD3⁺ T-cells in mice
240 with reduced or absent ATM expression compared to wildtype mice (**Fig. 5**). This reduction was further
241 compounded by concomitant deficiency of APTX. ATM and APTX deficiencies reduced T-cells in
242 peripheral blood by over 65% decrease compared to wild type controls. The effect of APTX deficiency
243 was additive to that of ATM deficiency suggesting a different mechanism of action for each of these two
244 proteins on T-cell generation. The reduction in the percentage of T-cells in peripheral blood was mostly
245 associated with reduction in the CD4+ helper T-cell population (**Fig. 5B**). Of interest, the proportion of

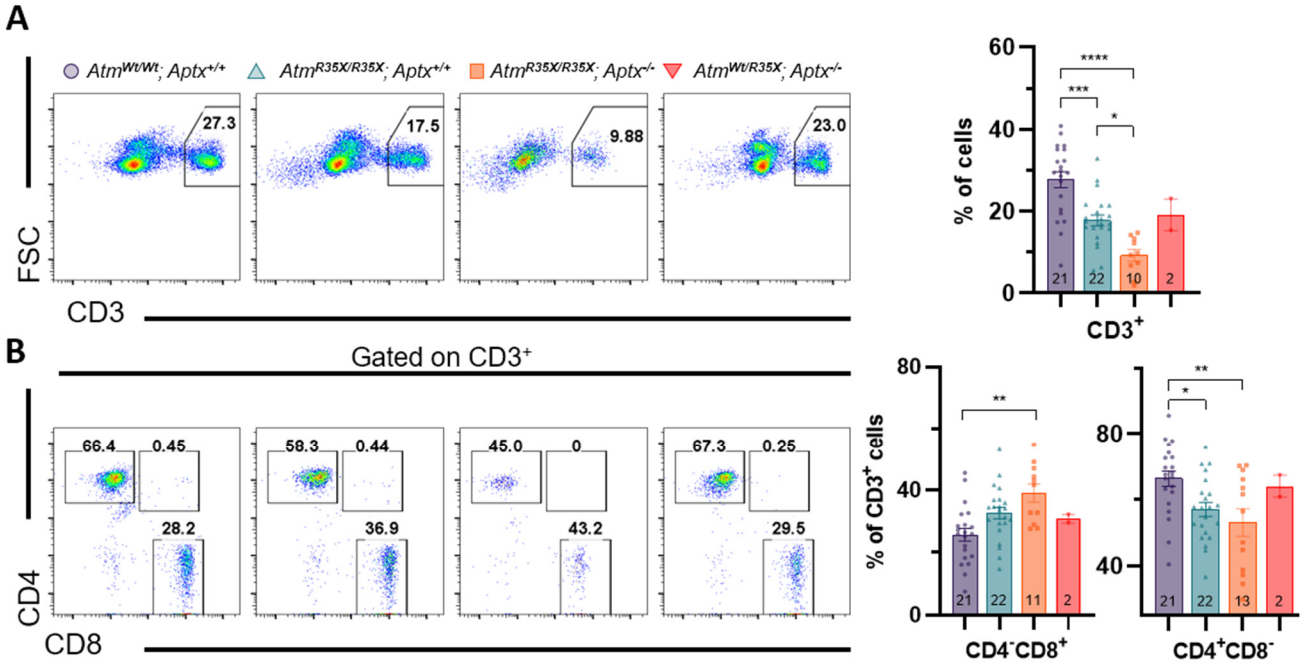

Figure 5. T-cell deficits are found in the blood of *$Atm^{R35X/R35X}$; $Aptx^{-/-}$* mice. A) Representative flow cytometric profiles of T-cell glycoprotein marker CD3 and summary plots indicate ATM and/or APTX deficient mice have decreased proportions of CD3⁺ T-cells in the blood. **B)** Representative flow cytometric profiles of T-cell glycoprotein markers CD4 and CD8 gated on CD3⁺ cells and summary plots for CD8 and CD4 single positive cell proportions. ATM deficient mice had reduced CD4⁺ proportions compared to mice with at least one copy of the *Atm* gene. Statistical significances were assessed via 1-way ANOVA followed by *posthoc* Tukey's pairwise multiple comparisons tests. Number of animals denoted at bottom of bar. Symbol/color key: $Atm^{Wt/Wt}$; $Aptx^{+/+}$ (purple circle), $Atm^{Wt/Wt}$; $Aptx^{-/-}$ (blue diamond), $Atm^{R35X/R35X}$; $Aptx^{+/+}$ (green triangle), $Atm^{R35X/R35X}$; $Aptx^{-/-}$ (orange square), $Atm^{Wt/R35X}$; $Aptx^{-/-}$ (red inverted triangle) **Figure 5/6-Source Data 1**

bioRxiv preprint doi: https://doi.org/10.1101/2020.11.23.394098; this version posted November 23, 2020. The copyright holder for this preprint (which was not certified by peer review) is the author/funder, who has granted bioRxiv a license to display the preprint in perpetuity. It is made available under aCC-BY 4.0 International license.

CD8+ T-cells was increased only in $Atm^{R35X/R35X}$; $Aptx^{-/-}$ mice (**Fig. 5B**). Again, we observed a differential effect of ATM and APTX deficiencies as seen for the effects of these mutations on the total T-cell fraction.

Given the reduction in T-cell populations in the blood, we next assessed T-cell development in the thymus. In this organ, bone marrow-derived T-cell progenitors undergo TCR gene rearrangement followed by positive selection for MHC restriction and negative selection of autoreactive clones. The phases of thymocyte development can be followed by monitoring expression of CD4 and CD8 expression in thymocytes. The progression of this developmental program goes from double negative ($CD4^-CD8^-$) thymocytes, to double positive ($CD4^+CD8^+$) thymocytes and then to single positive ($CD4^+$ or $CD8^+$) thymocytes. In addition, within the double negative stage, four different subpopulations can be identified, based on expression of CD25 and CD44, known as DN1 ($CD44^+CD25^-$), DN2 ($CD44^+CD25^+$), DN3 ($CD25^+CD44^-$) and DN4 ($CD44^-CD25^-$) (Germain 2002).

Gene rearrangement during thymocyte development occurs twice, once at the double negative thymocyte stage in the $CD25^+CD44^-$ stage (Krangel 2009) and then again in double positive thymocyte stage before progressing into separate $CD4^+$ and $CD8^+$ single positive populations (Livák et al. 1999). ATM deficiency has been linked to defects in both bouts of rearrangement in mice (Vachio 2007, Hathcock 2013). Therefore, we compared the proportion of cells in the thymus expressing these different developmental cell surface markers in our ATM deficient and control mice (**Fig. 6**). *$Atm^{R35X/R35X}$; $Aptx^{-/-}$* and *$Atm^{Wt/R35X}$; $Aptx^{-/-}$*, but not *$Atm^{R35X/R35X}$; $Aptx^{+/+}$* mice had significantly elevated proportions of $CD44^+CD25^-$, $CD44^+CD25^+$, and $CD44^-CD25^+$ cells compared to wildtype (**Fig. 6A**). These increased proportions appear to be due in part to an impediment of $CD44^-CD25^+$ cells maturing into $CD44^-CD25^-$ double negative cells, as the fraction of cells from *$Atm^{R35X/R35X}$; $Aptx^{-/-}$* and *$Atm^{Wt/R35X}$; $Aptx^{-/-}$* mice is significantly lower than wildtype (**Fig. 6A**). Of interest, APTX deficiency by itself had the greatest effect on the loss of DN4 cells suggesting that APTX deficiency, rather than ATM deficiency, is responsible for this effect. To our knowledge, this finding implicates for the first time APTX in gene rearrangement during the process of TCRβ recombination.

bioRxiv preprint doi: https://doi.org/10.1101/2020.11.23.394098; this version posted November 23, 2020. The copyright holder for this preprint (which was not certified by peer review) is the author/funder, who has granted bioRxiv a license to display the preprint in perpetuity. It is made available under aCC-BY 4.0 International license.

271 Next, we looked at the proportions of CD4⁺CD8⁺ thymocytes compared to CD4⁺CD8⁻ and CD4⁻CD8⁺

272 single positive thymocytes in these four different strains. In agreement with our results in the blood and

273 prior studies, we found that ATM-deficient mice but not control mice displayed decreased expression of

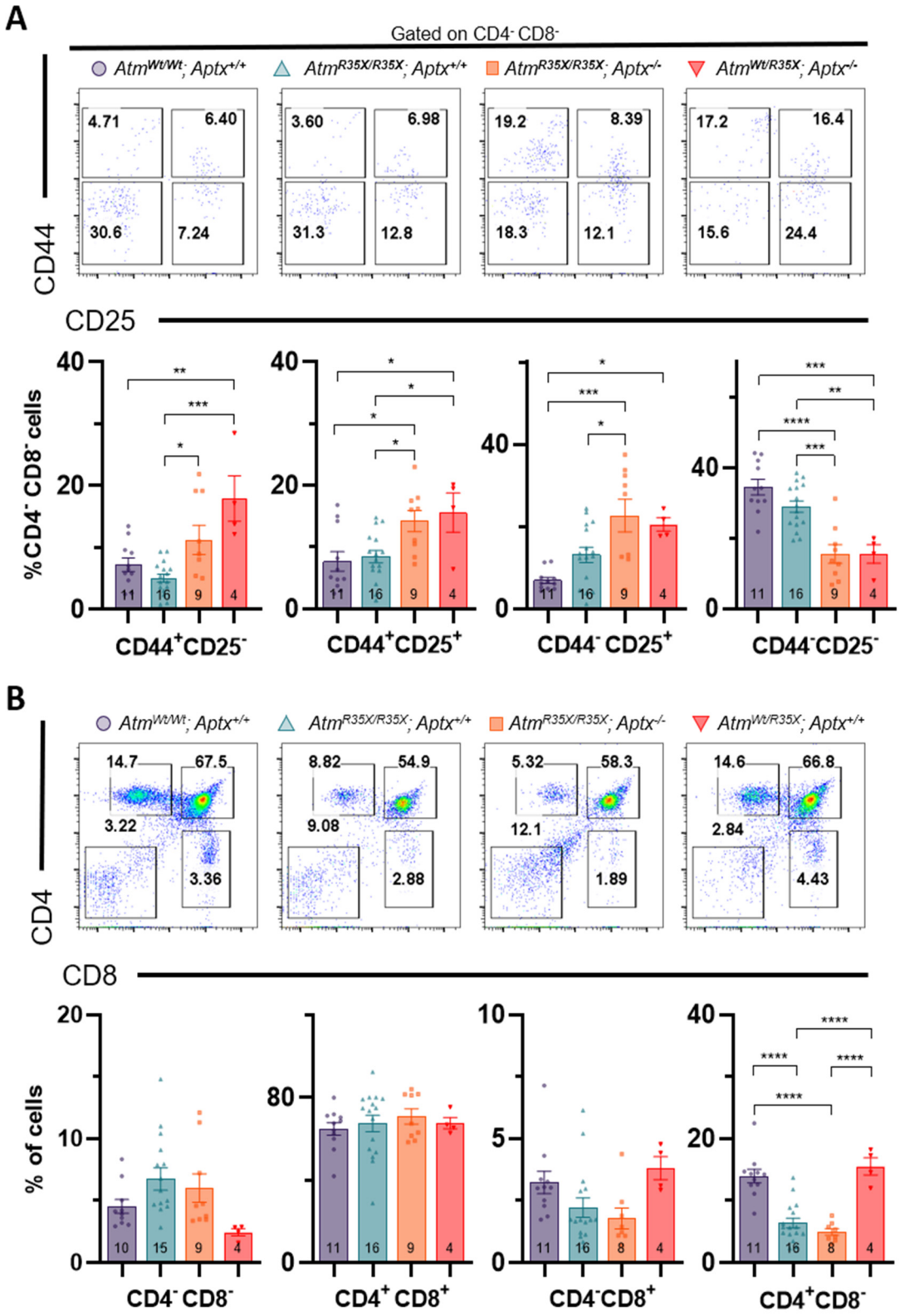

bioRxiv preprint doi: https://doi.org/10.1101/2020.11.23.394098; this version posted November 23, 2020. The copyright holder for this preprint (which was not certified by peer review) is the author/funder, who has granted bioRxiv a license to display the preprint in perpetuity. It is made available under aCC-BY 4.0 International license.

Figure 6. ATM and APTX deficiency confer deficits in T-cell expression, but at different developmental stages. A) Representative flow cytometric profiles of T-cell glycoprotein markers CD44 and CD25 gated on $CD4^{-}CD8^{-}$ double negative (DN) cells. Summary plots show proportions of thymocytes at DN stages 1-4 (left to right). APTX deficient mice display increased proportions for DN1-3 and decreased proportion at DN4 consistent with a deficit in ontogeny from DN3 to DN4. **B)** Representative flow cytometric profiles of T-cell glycoprotein markers CD4 and CD8 gated. ATM deficient mice display decreased proportions for CD4 and CD8 single positive cells consistent with a deficit in ontogeny from $CD4^{+}CD8^{+}$ double positive to $CD4^{+}$ and $CD8^{+}$ single positive fates. Statistical significances were assessed via 1-way ANOVA followed by *posthoc* Tukey's pairwise multiple comparisons tests. Number of animals denoted at bottom of bars. Symbol/color key: $Atm^{Wt/Wt}$; $Aptx^{+/+}$ (purple circle), $Atm^{Wt/Wt}$; $Aptx^{-/-}$ (blue diamond), $Atm^{R35X/R35X}$; $Aptx^{+/+}$ (green triangle), $Atm^{R35X/R35X}$; $Aptx^{-/-}$ (orange square), $Atm^{Wt/R35X}$; $Aptx^{-/-}$ (red inverted triangle) **Figure 5/6-Source Data 1**

$CD4^{+}CD8^{-}$ and $CD4^{-}CD8^{+}$ single positive thymocytes (**Fig. 6B**). These results support the role of ATM in TCR α/δ gene rearrangement during thymocyte development (Bredemeyer et al. 2006), a role that is independent of the role played by APTX in early thymocyte maturation.

2.7 Readthrough molecules overcome PTC to restore ATM expression

By inserting a primary nonsense mutation to cause ATM deficiency, this new model is amenable to efficacy testing of readthrough molecules with the potential to restore ATM expression by overcoming the nonsense mutation causing PTC. As proof-of-principle that readthrough compounds can restore ATM production, we exposed explant tissue harvested from ATM^{R35X} and ATM^{Q35X} mice with two different readthrough compounds for 72 hrs. and then measured ATM expression to assess restoration. In both types of ATM deficient mice, ATM expression was consistently restored in the spleen and cerebellum by both G418, an aminoglycoside previously known to have readthrough properties, and GJ103, a candidate SMRT compound derivative created by our group (**Fig. 7**). These results demonstrate that ATM expression can be restored by readthrough molecules in this mouse model, thereby creating the rationale for *in vivo* efficacy testing of compounds with suitable pharmaco-dynamic and -kinetic properties in follow-on studies.

bioRxiv preprint doi: https://doi.org/10.1101/2020.11.23.394098; this version posted November 23, 2020. The copyright holder for this preprint (which was not certified by peer review) is the author/funder, who has granted bioRxiv a license to display the preprint in perpetuity. It is made available under aCC-BY 4.0 International license.

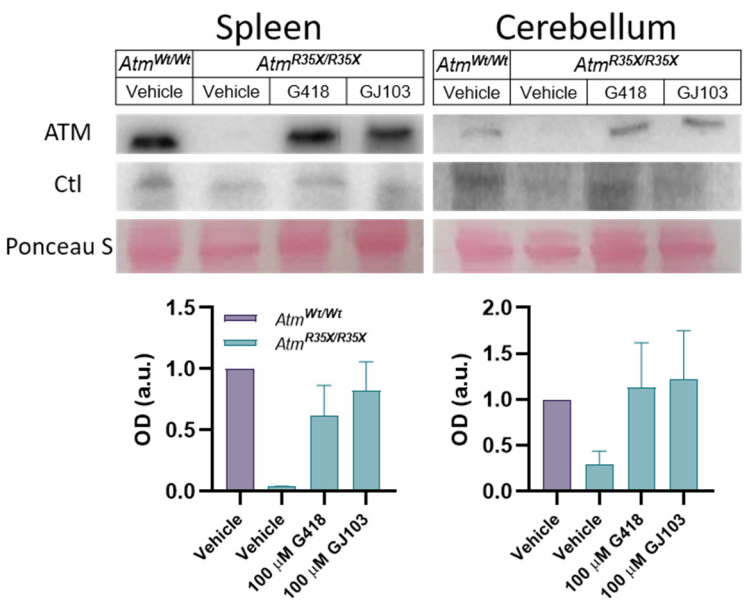

Figure 7. ATM protein expression is restored after readthrough compound exposure in explant tissues from *Atm*$^{R35X/R35X}$ and *Atm*$^{Q35X/Q35X.}$ Spleen and cerebellar explant tissue from *Atm*$^{R35X/R35X}$ and *Atm*$^{Wt/Wt}$ mice were treated with vehicle, the readthrough compounds G418 (100 μM) or GJ103 (100 μM) for 72 hrs. ATM immunoblots show recovery of ATM production in both the spleen (n=2) and cerebellum (n=3). Equal loading was assessed via housekeeping genes (Actin) and ponceau staining.

3.0 Discussion

By increasing genotoxic stress through the addition of a secondary hit to the DDR pathway, we generated an A-T mouse that displays the most comprehensive set of A-T symptoms of any mouse model to date. This includes a high incidence of cancer, defects in immune cell development, and most notably a severe and progressive ataxia associated with cerebellar atrophy. Together, these comorbidities encompass the three leading causes of premature death in A-T — each contributing to roughly a third. Of the 3 morbidities, the incapacitating effect of ataxia is the most penetrant; thus, it is reported by patients and caregivers as having the greatest impact on quality of life. For this reason, the presence of ataxia and cerebellar atrophy in this new mouse model is significant as it provides for the first time a resource to not only investigate the mechanisms of neurological dysfunction but also, provides an important *in vivo* model to test critically needed A-T therapeutics like the readthrough compounds tested here.

Our findings suggest two possibilities for why deficiency in genome stability proteins like A-T in mice do not result in comparably severe neurological deficits as it does in humans: **1)** rodents have redundancies in genome stability pathways in the brain thereby reducing the impact of ATM or APTX deficiency alone, or **2)** a mouse's lifespan is too short for genetic mutations that lead to genome instability to accumulate and cause dysfunction. The fact that the nervous system, compared to others, like the immune, requires

bioRxiv preprint doi: https://doi.org/10.1101/2020.11.23.394098; this version posted November 23, 2020. The copyright holder for this preprint (which was not certified by peer review) is the author/funder, who has granted bioRxiv a license to display the preprint in perpetuity. It is made available under aCC-BY 4.0 International license.

higher genotoxic pressure is an important question, and potentially points to differing mechanisms of action for ATM within different organ systems of the body.

In the immune system, ATM is implicated in the repair of DNA breaks that naturally occur during gene rearrangement of antigen receptor genes in B- and T-cell precursors, a phenomenon critical for antigen receptor (Ig and TCR) diversity of these cells. Our finding that T-cell proportions in the blood are significantly reduced is consistent with prior studies in humans and A-T knockout mice (Schubert, Reichenbach, and Zielen 2002; Hathcock et al. 2013; Chao, Yang, and Xu 2000; Barlow et al. 1996). This reduction of T-cells in the periphery likely correlates with a defect in both cellular and humoral immunity. Importantly, we found that expression of at least one copy of the ATM gene is enough to restore CD4+ deficits in the blood indicating that therapies able to restore at least some ATM expression would have therapeutic efficacy. Although we have not assessed B-cell development in this paper, it is likely that similar conclusions would apply to that process given their mechanistic similarities.

As expected, the reduction on T-cells in peripheral blood correlated with defective thymocyte development. In the thymus, we found two main defects. One, induced primarily by APTX deficiency, manifests as a defect in the DN3 to DN4 transition coinciding with early rearrangement of TCR β locus. The other defect, primarily caused by ATM deficiency, correlates with decreased progression of double positive $CD4^+CD8^+$ to single positive cells, primarily $CD4^+$ thymocytes. While the APTX finding was surprising, as its deficiency (AOA 1) is not associated with immune deficits, APTX is known to interact with TCR β gene rearrangement proteins, including XRCC4 (Clements et al. 2004). Future studies aimed at defining APTX's role in end-joining mechanisms during TCR gene rearrangement will be important, and the possibility that alternative end-joining mechanisms, like the use of microhomologies account for the lack of an immune deficit in its absence need further investigation (Bogue et al. 1997).

In line with the 40% cancer prevalence found in A-T patients, we found roughly 30% of ATM deficient mice developed cancerous tumors. In humans, the most common cancers observed are leukemia (blood cell) and lymphoma (immune cell), with sporadic reports of ovarian, breast, and thyroid cancer. The tumors we observed in ATM deficient mice were almost exclusively thymic lymphomas that produced

bioRxiv preprint doi: https://doi.org/10.1101/2020.11.23.394098; this version posted November 23, 2020. The copyright holder for this preprint (which was not certified by peer review) is the author/funder, who has granted bioRxiv a license to display the preprint in perpetuity. It is made available under aCC-BY 4.0 International license.

large masses in the thoracic cavity. These tumors put pressure on the heart and lungs, leading to undersized organs that likely contributed to the animal's death. The thymic and lymphatic origins of these tumors raise the possibility that they arise from cell populations in the thymus that did not undergo proper gene rearrangement, a possibility that has received some consideration, but requires further exploration (Starczynski et al. 2003).

The survivability of *Atm*$^{R35X/R35X}$; *Aptx*$^{-/-}$ mice is considerably longer than prior A-T mouse models. In comparison, the first A-T KO mouse model reported by Barlow et al. died from thymomas usually within 2-4 months after birth (Barlow et al. 1996). The increased severity of cancer survivability in this, and many other knockout A-T mouse models is likely genetic, as the background strain harboring the mutation has been shown to have significant effects on cancer prevalence and survivability, with A/J and C57BL/6 backgrounds having significantly increased survivability over the BALBC and 129S strains (Genik et al. 2014). The fact that our ATM deficient mice were created on a C57BL/6 background likely underlies their comparatively long lifespan. Given that the *Atm*$^{R35X/R35X}$; *Aptx*$^{+/+}$ mice do not develop ataxia, it is unlikely that the early death in A-T KO mice prevents observation of an ataxic phenotype that would otherwise develop in these mice. On the other hand, it is unknown whether the C57BL/6 background confers a resilience to developing ataxia, as it does for cancer. Defining the genetic or possibly epigenetic factors that influence the severity of the disease could provide avenues for future therapeutic development.

Atm$^{R35X/R35X}$; *Aptx*$^{-/-}$ mice developed a visually apparent and measurable progressive loss in motor coordination. As is the case in A-T patients, the degree of ataxia observed in the A-T mice was not uniform (Rothblum-Oviatt et al. 2016; Levy and Lang 2018; Boder and Sedgwick 1958). We found that while all the *Atm*$^{R35X/R35X}$; *Aptx*$^{-/-}$ mice at P400 had visually apparent challenges moving around, there was a significant variation in ataxia, from those that could still walk around, although clumsily in the cage, to those moving almost solely by contortion. We observed motor differences in the *Atm*$^{R35X/R35X}$; *Aptx*$^{-/-}$ mice as early as 8 days old, where their time to right in the righting reflex was 5-10 times longer than control animals. Subtle differences in spontaneous activity and body position were qualitatively detected at P30, however, the overall ability of *Atm*$^{R35X/R35X}$; *Aptx*$^{-/-}$ mice to ambulate was not dramatically affected until

bioRxiv preprint doi: https://doi.org/10.1101/2020.11.23.394098; this version posted November 23, 2020. The copyright holder for this preprint (which was not certified by peer review) is the author/funder, who has granted bioRxiv a license to display the preprint in perpetuity. It is made available under aCC-BY 4.0 International license.

after P210. By P400, multiple behavioral deficits were obvious, including changes in gait, increased startle reflex, tremor, and locomotor activity. One potential limitation of this model is the difference in temporal manifestation of ataxia, which develops at a developmentally later stage in the mice compared to humans. Additionally, the fact that this model expresses null mutations in two genome stability genes that has not been observed in human disease must be carefully factored into the interpretation of future experiments utilizing this new model.

Ataxia in A-T is linked to loss of cerebellar function due to its relatively selective neuropathology across the brain and its known role in coordinated movement (Hoche et al. 2012). Consistent with patient neuroimaging studies (Wallis et al. 2007; Sahama et al. 2015; Sahama et al. 2014; Dineen et al. 2020; Tavani et al. 2003; Quarantelli et al. 2013), we find that cerebellar size in *Atm*$^{R35X/R35X}$; *Aptx*$^{-/-}$ mice is initially normal, but eventually atrophies. Historically, correlations between the severity of atrophy and ataxia in humans has not been straightforward, as postmortem assessment of cerebellar atrophy has not necessarily been a good predictor of ataxia severity in human patients (Aguilar et al. 1968; Crawford et al. 2006); although a recent neurometric and quantitative behavioral assessment study indicates a mild correlation exists (Dineen et al. 2020). The central question underlying these findings is, to what extent does cerebellar dysfunction, in the absence of, or prior to atrophy contribute to the ataxic phenotype *vs.* atrophy itself. Since ataxia is often the first A-T symptom identified by parents and doctors, determining whether future therapies will require replacing atrophied tissue or restore or halt changes in neuronal function has significant ramifications.

Our observation that *Atm*$^{R35X/R35X}$; *Aptx*$^{-/-}$ mice display differences in cerebellar physiology, specifically decreased spontaneous PN action potential firing frequency, changes in morphology, and ultimately PN death is in line with multiple other ataxic mouse model studies, including those focused on spinocerebellar ataxias (SCA) 1, 2, 3, 5, 6, and 13 (see review (Cook, Fields, and Watt 2020)). In *Atm*$^{R35X/R35X}$; *Aptx*$^{-/-}$ mice, we find that reduced PN firing frequency and morphological size is correlated with only mild behavioral deficits. As PN physiology progressively degrades the cerebellum atrophies resulting in severe ataxia. The underlying cause of the PN abnormality likely arises from changes in Ca^{+} homeostasis as the

bioRxiv preprint doi: https://doi.org/10.1101/2020.11.23.394098; this version posted November 23, 2020. The copyright holder for this preprint (which was not certified by peer review) is the author/funder, who has granted bioRxiv a license to display the preprint in perpetuity. It is made available under aCC-BY 4.0 International license.

result of decreased Inositol 1,4,5-triphosphate receptor 1 (*Itpr1*) expression previously found in ATM-deficient mice (Kim et al. 2020), and is associated with changes in PN activity in SCA2. Moreover, we find that progressive decline in PN health is strongest in the vermis compared to the hemispheres. While the functional anatomy of the cerebellum is still under intense scrutiny, the medial cerebellum is considered to be an integral part of the spinocerebellum, receiving somatic sensory information from the spinal cord and motor cortex transforming information important for aspects of whole-body posture and locomotion (Machado et al. 2015; Apps and Garwicz 2005; Coffman, Dum, and Strick 2011).

Pinpointing where, when, and how ATM deficiency causes cerebellar pathology and ataxia has been a challenge as prior ATM deficient mice generally lack the characteristic features needed to causally link cellular and molecular deficits to the ataxic phenotype. Multiple promising avenues of investigation have been defined, including those focused at the neuronal level where ATM is implicated in oxidative stress signaling (Chen et al. 2003) and synaptic function (Li et al. 2009; Vail et al. 2016), as well as glial function, where recent evidence suggests glial pathology may be a leading factor in cerebellar pathology (Kaminsky et al. 2016; Campbell et al. 2016; Petersen, Rimkus, and Wassarman 2012; Weyemi et al. 2015). This novel animal model provides a new tool to test mechanistic hypotheses regarding how ATM deficiency causes cerebellar pathology and ataxia as well as a testing platform for both previously proposed therapeutic candidates (Browne et al. 2004; Chen et al. 2003) and our own SMRT compounds (Du et al. 2013).

4.0 Materials and Methods

4.1 Ethics Statement

This study was performed in strict accordance with the recommendations in the Guide for the Care and Use of Laboratory Animals of the National Institutes of Health. All the animals were handled according to approved institutional animal care and use committee (IACUC) protocols at The Lundquist Institute (31374-03, 31773-02) and UCLA (ARC-2007-082, ARC-2013-068). The protocol was approved by the Committee on the Ethics of Animal Experiments of the Lundquist Institute (Assurance Number: D16-00213). Every effort was made to minimize pain and suffering by providing support when necessary and choosing ethical endpoints.

bioRxiv preprint doi: https://doi.org/10.1101/2020.11.23.394098; this version posted November 23, 2020. The copyright holder for this preprint (which was not certified by peer review) is the author/funder, who has granted bioRxiv a license to display the preprint in perpetuity. It is made available under aCC-BY 4.0 International license.

4.2 Mice

All mice were group housed and kept under a 12 h day/night cycle with food and water available *ad libitum*. Animals were housed within the general mouse house population, and not in specialized pathogen free rooms. Older animals were made available wetted food or food gel packs on the ground of the cages as ataxia developed. Atm^{R35X} and Atm^{Q35X} mice were created and provided by Dr. Hicks and colleagues at the University of Manitoba.

These mice were created to contain the 103 C>T mutation found in a large population of North African AT patients, using recombineering Gateway technology and site-directed mutagenesis. A C>T mutation at this position in the mouse *Atm* gene creates a TAG G stop codon. The same mutation in the human ATM gene produces a TGA G stop codon. In consideration of the use of these models for therapeutic interventions, we chose to create a mouse model for each of the two PTC codons (**Fig. 1A**).

A modified Gateway R3-R4-destination vector was used to pull out the desired region of the mouse Atm gene from a Bacterial Artificial Chromosome (BAC) and subsequently mutated to create either a TAG G stop codon at codon 35 (M00001, position 103 (C>T)) or a TGA G stop codon (M00002, position 103 (CAG>TGA), replicating the human AT PTC). The genomic alleles were then cloned into a modified version of the NorCOMM mammalian targeting vector using a 3-way Gateway Reaction (Bradley, Anastassiadis *et al*. 2012). The resulting targeting vectors were electroporated into C2 ES cells (C57Bl/6N, derived in A. Nagy lab, Toronto, Canada, Gertsenstein, Nutter *et al.*, 2010) and successfully targeted clones were identified by selection with G418. Integration of the mutated targeting cassette into the *Atm* gene locus was confirmed by Southern blot, and by sequencing of PCR products to confirm the presence of the Atm PTC mutation, error free targeting into the Atm locus and error free functional components of the vector (data not shown). Positive ES clones were used for blastocyst injection to obtain the transgenic lines. The transgenic allele contained a floxed human beta actin promoter - delta TK1- Neo cassette in the intron upstream of the region containing the mutated exon. This floxed cassette was subsequently excised by crossing with a Cre driver mouse (B6.C-Tg(CMV-cre)1Cgn/J) to generate $Atm^{R35X/Wt}$ and $Atm^{Q35X/Wt}$ (MGI nomenclature: $Atm^{TM1(103CAG>TGA)MFGC}$ and $Atm^{TM1(103C>T)MFGC}$, respectively)

bioRxiv preprint doi: https://doi.org/10.1101/2020.11.23.394098; this version posted November 23, 2020. The copyright holder for this preprint (which was not certified by peer review) is the author/funder, who has granted bioRxiv a license to display the preprint in perpetuity. It is made available under aCC-BY 4.0 International license.

435 mouse lines (**Fig. 1A**). Genotyping of the two *Atm* lines was performed by using the following primers at
436 Tm 62°C: Atm gene forward (F) primer: 5'-CCTTTGAGGCATAAGTTGCAACTTG-3'; and Atm gene
437 reverse (R) primer: 5'-GTACAGTGTATCAGGTTAGGCATGC-3', creating a Wild-type allele product of
438 151bp or targeted allele product of 241bp (**Figs. 1A, 1B**).

439 Atm^{R35X} and Atm^{Q35X} were backcrossed with C57Bl/6J mice for 9 generations (99.2% isogenic) prior to
440 cryopreservation and subsequent rederivation using C57Bl/6J surrogate mothers. Atm^{R35X} and Atm^{Q35X}
441 breeders were obtained from F1 sibling $Atm^{R35X/Wt}$ and $Atm^{Q35X/Wt}$ mice. $Atm^{R35X/R35X}$ and $Atm^{Q35X/Q35X}$ were
442 both found to be fertile. *Aptx* knockout ($Aptx^{-/-}$) mice were created and provided to Dr. Mathews as
443 embryos from Dr. McKinnon (Ahel et al. 2006), and subsequently rederived via C57Bl/6J surrogate
444 mothers. $Aptx^{-/-}$ mice are on a C57Bl/6 and 129 mixed background. Atm^{R35X}; $Aptx^{KO}$ mice of various Wt,
445 heterozygous, and homozygous combinations were created from $Atm^{R35X/Wt}$; $Aptx^{-/+}$ breeders generated
446 by crossing $Atm^{R35X/R35X}$ and $Aptx^{-/-}$ mice. One cohort of double mutant and corresponding control mice
447 were used in the longitudinal behavioral study for gait analyses and SHIRPA testing (**Figs. 2**, **3**). Multiple
448 additional cohorts of age matched double mutant and control mice were used for electrophysiological,
449 immunohistological, and Vertical Pole test experiments (**Figs. 4**, **7**). Immunological and protein
450 expression experiments were carried out using mice bred from the original Atm^{R35X} and Atm^{Q35X} rederived
451 mice (**Figs**. **5**, **6**, and **8**).

452 Genotyping was performed from ear tissue samples of P8-11 mice. Real-time PCR methods conducted
453 by Transnetyx Inc. were used to determine each animals' genotype. Animals were made identifiable via
454 toe tattoos given at the same time as ear biopsy. Unique primers for Atm^{R35X} and Atm^{Q35X} were quantified
455 and used to identify Wt, hetero- and homo-zygous mice (listed above). $Aptx^{-/-}$ and $Aptx^{Wt}$ primers were
456 used to assess their genotypes.

457 **4.3 Animal Health**

458 Animals were weighed via a digital scale at P8, 45, 120, 210, 400. Animal death was recorded as the day
459 found dead, or on the day of euthanization when the animals reached a humane endpoint (animal unable to
460 right itself within 60s, significant hair matting indicating lack of self-grooming, or excessive distress as noted

bioRxiv preprint doi: https://doi.org/10.1101/2020.11.23.394098; this version posted November 23, 2020. The copyright holder for this preprint (which was not certified by peer review) is the author/funder, who has granted bioRxiv a license to display the preprint in perpetuity. It is made available under aCC-BY 4.0 International license.

by the veterinary staff). Animal carcasses were immediately frozen upon death, and postmortem necropsies were carried out in batch. Probable cause of death was determined to the best of our ability in collaboration with the staff veterinarian (Dr. Catalina Guerra) by visual inspection of the internal organs. Some mice were cannibalized or accidentally disposed of by vivarium staff and were therefore labelled as “missing.” Mice with no discernable visual cause of death were labelled “indeterminable.” Mice that were found with thoracic masses near where the thymus would normally be in young mice were listed as “thymic cancer.” All other identified probable causes of death (e.g., enlarged livers, urinary blockage) were labelled “other.”

4.4 Behavior

Before performing any behavioral test, mice were acclimated to the behavioral suite for ~20 minutes. Mice were tested at varying times of the day, in line with their day cycle. A battery of behavioral tests was performed on naïve double mutant mice of the indicated genotypes at various time points depending on the behavior but in the same cohort of mice. The battery of tests included Catwalk Gait assessment (P45, 120, 210, 400) and a subset of the SmithKline-Beecham Harwell Imperial-College and Royal-London-Hospital Phenotype Assessment (SHIRPA) tests (P30 and 400). These tests were conducted by the UCLA Behavioral Core. Double mutant and control mice were additionally examined on the Vertical Pole test. All behavioral apparatus was wiped down with ethanol (70%) between each testing each subject.

Gait Analysis

We used a Noldus Catwalk Gait analysis system designed to semi-automatically measure and analyze the gait of mice during normal ambulation. Briefly, the movement of mice across a glass bottom corridor is video recorded from a ventral position. Paw prints are highlighted in the video due to light illumination across the glass walking platform. Each mouse step within a video is subsequently detected using Noldus software in a semi-automated fashion. A run for each mouse consists of 3 trials of consistent ambulation across the monitored platform. Only consistent trials are accepted, and mice may take up to 10 attempts to complete 3 compliant trials in either direction across the corridor. Compliant trials were defined as those with movement across the platform under 5s long and with no more than 60% speed variation. Once placed onto the platform, mice generally ran back and forth without any need for experimenter prompting.

bioRxiv preprint doi: https://doi.org/10.1101/2020.11.23.394098; this version posted November 23, 2020. The copyright holder for this preprint (which was not certified by peer review) is the author/funder, who has granted bioRxiv a license to display the preprint in perpetuity. It is made available under aCC-BY 4.0 International license.

Vertical Pole

Mice are placed at the top of an 80 cm tall bolt with their nose faced down and hind paws as close to the top as possible. Mice are immediately released, and time started immediately upon placement. Time is stopped when the first forepaw touches the surface below the pole. A mouse's natural predilection is to immediately climb down the pole, and they are given up to 60s to traverse the pole, otherwise they are helped off the pole. A non-completed trial is automatically given a time of 30s, as 95% of mice that did not descend within 30s were still on the pole at the 60s mark.

SHIRPA

Behavioral tests were conducted by the University of California, Los Angeles Behavioral Core at P30 and P400. All parameters are scored to provide a quantitative assessment, which enables comparison of results both over time and between different laboratories. Each mouse was sequentially tested across all behaviors within ~20 min. time span before moving onto the next mouse. The experimenter was blinded to animal genotype. The screen was performed as described previously (Rogers et al. 1997).

Behavioral Observation

The primary screen provides a behavioral observation profile and assessment of each animal begins by observing undisturbed behavior in a viewing jar (10 cm diameter) for 5 min. In addition to the scored behaviors of **body position**, **spontaneous activity**, **respiration rate**, and **tremor**, the observer logs any instances of bizarre or stereotyped behavior and convulsions, compulsive licking, self-destructive biting, retropulsion (walking backwards) and indications of spatial disorientation.

Arena Behavior

Thereafter, the mouse is transferred to the arena (30 cm x 50 cm) for testing of transfer arousal and observation of normal behavior. The arena is marked into a grid of 10 cm^2 squares to measure locomotor activity within a 30s period. While the mouse is active in the arena, measures of **startle response**, **gait**, **pelvic elevation**, and **tail elevation** are recorded.

Supine Restraint

bioRxiv preprint doi: https://doi.org/10.1101/2020.11.23.394098; this version posted November 23, 2020. The copyright holder for this preprint (which was not certified by peer review) is the author/funder, who has granted bioRxiv a license to display the preprint in perpetuity. It is made available under aCC-BY 4.0 International license.

The animal is restrained in a supine position to record autonomic behaviors. During this assessment, **grip strength**, **body tone**, **pinna reflex**, **corneal reflex**, **toe pinch**, **wire maneuver**, and **heart rate**, were evaluated.

Balance and Orientation

Finally, several measures of vestibular system function were performed. The **righting reflex**, **contact righting reflex**, and **negative geotaxis** tests were performed. Throughout this procedure vocalization, urination and general fear, irritability, or aggression were recorded.

Equipment Used

1. Clear Plexiglas arena (approximate internal dimensions 55 x 33 x18 cm). On the floor of the arena is a Plexiglas sheet marked with 15 squares (11 cm). A rigid horizontal wire (3 mm diameter) is secured across the rear right corner such that the animals cannot touch the sides during the wire maneuver. A grid (40 x 20 cm) with 12 mm mesh (approximate) is secured across the width of the box for measuring tail suspension and grip strength behavior.
2. A clear Plexiglas cylinder (15 x 11 cm) was used as a viewing jar.
3. One grid floor (40 x 20 cm) with 12 mm meshes on which viewing jars stand.
4. Four cylindrical stainless-steel supports (3 cm high x 2.5 cm diameter) to raise grids off the bench.
5. One square (13 cm) stainless steel plate for transfer of animals to the arena.
6. Cut lengths of 3 / 0 Mersilk held in the forceps for corneal and pinna reflex tests
7. A plastic dowel rod sharpened to a pencil point to test salivation and biting.
8. A pair of dissecting equipment forceps, curved with fine points (125 mm forceps, Philip Harris Scientific, Cat. No. D46-174), for the toe pinch.
9. A stopwatch.
10. An IHR Click box is used for testing the startle responses. The Click Box generates a brief 20 KHz tone at 90dB SPL when held 30cm above the mouse. Contact Prof. K.P. Steel, MRC Institute of Hearing Research, University Park, Nottingham NG7 2RD.
11. A ruler.

bioRxiv preprint doi: https://doi.org/10.1101/2020.11.23.394098; this version posted November 23, 2020. The copyright holder for this preprint (which was not certified by peer review) is the author/funder, who has granted bioRxiv a license to display the preprint in perpetuity. It is made available under aCC-BY 4.0 International license.

12. A 30 cm clear Plexiglas tube with an internal diameter of 2.5 cm for the contact righting reflex.

4.5 Electrophysiology

Preparation of acute cerebellar slices

Acute parasagittal slices of 300 um thickness were prepared from the cerebellum of experimental and control littermate mice by following published methods (Hansen et al., 2013). In brief, cerebella were quickly removed and immersed in an ice-cold extracellular solution with composition of (mM): 119 NaCl, 26 $NaHCO_3$, 11 glucose, 2.5 KCl, 2.5 $CaCl_2$, 1.3 $MgCl_2$ and 1 NaH_2PO_4, pH 7.4 when gassed with 5% CO_2/95% O_2. Cerebella were sectioned parasagittal using a vibratome (Leica VT-1000, Leica Biosystems, Nussloch, Germany) and initially incubated at 35°C for ~30 min, and then equilibrated and stored at room temperature until use.

Extracellular Electrophysiology

Extracellular recordings were obtained from Purkinje neurons (PNs) in slices constantly perfused with carbogen-bubbled extracellular solution (see above). Cells were visualized with DIC optics and a water-immersion 40× objective (NA 0.75) using a Zeiss Examiner microscope. Glass pipettes of ~3 MΩ resistance (Model P-1000, Sutter instruments, Novato, CA) were filled with extracellular solution and positioned near PN axon hillocks in order to measure action potential-associated capacitive current transients in voltage clamp mode with the pipette potential held at 0 mV. Data was acquired using a MultiClamp 700B amplifier at 20 kHz, Digidata 1440 with pClamp10 (Molecular Devices, Sunnyvale, CA) and filtered at 4 kHz. A total of 20 to 45 PNs were recorded from for each animal across all genotypes, sexes, and age groups. Recordings were distributed across both the medial-lateral and rostro-caudal axis of the cerebellum. Specifically, recordings were made from serial sections in the flocculus, lateral (2nd or 3rd), intermediate (6th or 7th), and medial (11th or 12th) slices. Lower number slices were used in the younger age groups (P45 and 110) to roughly match the relative positioning of recordings across age groups. 0-3 recordings were made from each lobule within each slice dependent on tissue quality and health. Each recording lasted for 1-minute. 3 to 5 mice were used for each age group and the experimenter was blinded to the genotype, age, and sex.

bioRxiv preprint doi: https://doi.org/10.1101/2020.11.23.394098; this version posted November 23, 2020. The copyright holder for this preprint (which was not certified by peer review) is the author/funder, who has granted bioRxiv a license to display the preprint in perpetuity. It is made available under aCC-BY 4.0 International license.

Analyses

Experiments were analyzed using standard and custom routines in Clampfit (Molecular Device), IgorPro (Wavemetrics), and Excel (Microsoft). Specifically, action potentials were threshold detected and spiking statistics (i.e., frequency and interval length), determined using adapted IgorPro routines (Taro Tools; https://sites.google.com/site/tarotoolsregister/). The coefficient of variation of the mean interspike interval (CV) and the median interspike interval (CV2=2 |ISIn+1-ISIn|/(ISIn+1+ISIn)) were calculated in Excel using custom macros.

4.6 Examination of Cerebellar Degeneration

Cerebellar size

Immediately after brain removal from the skull, a dorsal, whole mount image was obtained. Images were then processed using Fiji (NIH). The forebrain and cerebellar sizes were assessed by outlining their 2-dimensional space and then calculating area. We normalized for possible differences in overall brain size by dividing the results of the cerebellum by forebrain size to produce a relative cerebellum to forebrain ratio. Experimenters were blind to the genotype of the animal.

Immunohistochemistry

At the respective study endpoints (P45, 120, 210, 400), male and female mice of all genotypes represented in this study were anesthetized with isoflurane and underwent transcardial perfusion with phosphate-buffered saline followed by 4% (w/v) buffered paraformaldehyde (PFA) and then dissected to extract the brain. Images of the whole brain were taken immediately after removing the brain from the skull and the brains were then submerged in 4% PFA for 24 hours, followed by 72 hours in 30% sucrose in Tris-buffered saline (TBS) with 0.05% azide, and then cryoprotected in TBS-AF and stored at 4°C until further use. The cerebellum was separated from the forebrain and parasagittally sectioned using a sliding microtome (Microm HM 430, Thermo Scientific) set to section at 40µm thickness. Cerebellum sections were collected in a series of six and stored in TBS-AF at 4° C until further use. For immunofluorescent visualization of Purkinje neurons, cerebellum sections of both $Atm^{Wt/Wt}$; $Aptx^{+/+}$ and $Atm^{R35X/R35X}$; $Aptx^{-/-}$ (n=5 per genotype) were washed for 5 minutes in TBS three times, and then

bioRxiv preprint doi: https://doi.org/10.1101/2020.11.23.394098; this version posted November 23, 2020. The copyright holder for this preprint (which was not certified by peer review) is the author/funder, who has granted bioRxiv a license to display the preprint in perpetuity. It is made available under aCC-BY 4.0 International license.

blocked in 15% normal goat serum at room temperature for 30 minutes followed by free floating incubation in rabbit anti-calbindin D-28k (1:1000, Swant cat# CB38a) for 1 hour at room temperature on an orbital shaker, then washed for 5 minutes with TBS three times, followed by free floating incubation in goat anti-rabbit Alexa Fluor 488 (1:1000, Invitrogen cat# A-11034) for 1 hour in the dark at room temperature on an orbital shaker. Following secondary antibody incubation, sections were washed for 5 minutes in TBS three times and stored in TBS until further use. Sections were mounted and cover-slipped with Fluoromount-G with DAPI (Southern Biotech cat# 0100-20). Slides were scanned using Stereo Investigator version 2020.1.3 64bit (MBF Bioscience) on a Zeiss Axio Imager.M2 microscope (Carl Zeiss Microscopy) using a 20x objective (NA 0.5) and images captured with a Hamamatsu ORCA Flash 4.0 LT C11440 digital camera (Hamamatsu Photonics). To quantify the number of calbindin-reactive cells in the resulting images, regions of interest were selected and drawn around the most dorsal portion of the Purkinje neuron layer in lobule 8 of medial sections (based on the electrophysiological differences previously observed) and the regions of interest were measured in semi-automated fashion using a Smart Segmentation recipe (using Region: Area, Region: Percent Area, and Region: Diameter, Mean as filters) on ImagePro Premier version 9.3 (Media Cybernetics).

Purkinje cell body size comparison was accomplished by using the mean diameter measurements obtained in the previously described quantification of lobule VIII PNs. Cell quantification data was visually inspected against the quantified images to ensure that only complete Purkinje cell bodies were included in this analysis, any cells without full cell bodies apparent in the image were excluded. Experimenter was blinded to mouse genotype.

4.7 Flow Cytometry Measurements

Flow cytometry analysis of blood and thymus cells was performed by staining with specific anti-mouse antibodies: CD4 (Invitrogen cat# 50-0041-82) CD8 (Invitrogen cat# 53-0081-82) CD3 (Invitrogen cat#12-0031-83), CD44 (Invitrogen cat# 25-0441-82) and CD25 (Invitrogen cat# 47-0251-82). Briefly, whole-blood samples (50 ul) were stained using fluorescent-labeled antibodies, then red-blood cells were lysed using BD lysing solution (BD Biosciences cat# 349202) while live white-blood cells were stained using a

bioRxiv preprint doi: https://doi.org/10.1101/2020.11.23.394098; this version posted November 23, 2020. The copyright holder for this preprint (which was not certified by peer review) is the author/funder, who has granted bioRxiv a license to display the preprint in perpetuity. It is made available under aCC-BY 4.0 International license.

viability stain (BD Biosciences cat# 564996). Thymuses were mechanically dissociated. 1-2 million thymus cells were similarly stained using specific antibodies for CD4, CD8, CD44 and CD25. Analysis of immuno-stained white blood cells or thymus samples was performed using FACS ARIA III and data analyzed using FlowJo software as reported previously (Sanghez et al. 2017).

4.8 Western Blots

Protein extracts (cells/tissues) were homogenized in radioimmunoprecipitation assay (RIPA) lysis buffer (150 mM NaCl, 1% Nonidet P-40 [NP-40], 0.5% deoxycholate, 0.1% SDS, 50 mM Tris, pH 8.0) with protease inhibitors (10 ug/ml AEBSF, 10 ug/ml leupeptin, 5 ug/ml pepstatin, 5 ug/ml chymotrypsin, 10 ug/ml aprotinin) (Roche cat# 1167498001). The protein extracts were sonicated then pelleted by centrifugation at 13,000 rpm for 15 min at 4°C. BCA protein assay (Pierce, 23250) was used to quantify protein concentrations. Samples containing equal amounts of protein 50-100 ug per lane were separated using 4–12% gradient TGX precast gels BioRad (cat# 4561093EDU) then transferred by TransBlot Semi-Dry BioRad system (cat #1704150EDU) using Nitrocellulose transfer pack (cat# 1704158EDU). Transferred blots were stained by Ponceau S stain for equal protein loading then washed and blocked with 5% nonfat dry milk in TBST for 1hr at room temp. Primary antibodies were incubated with shaking overnight at 4°C. Blots were probed for the following antibodies: ATM (D2E2) Rabbit mAb Cell Signaling, (cat# 2873) at 1:1000 dilution, β-Actin (D6A8) Rabbit mAb Cell Signaling (cat#8457), GAPDH (D16H11) Rabbit mAb Cell Signaling (cat #5174) followed by the appropriate horseradish peroxidase–conjugated (HRP) secondary Anti-rabbit, Anti-mouse for 2 hours at room temperature. After multiple washes with TBST, Protein expression was detected by Radiance Plus chemiluminescence substrate using the Azure c400 and the BioRad ChemiDoc imaging systems. Densitometric analysis of the ATM was performed using ImageJ. Experiments were performed with 2 technical and 2-3 biological replicates as indicated.

4.9 Statistical Assessment

The number of animals chosen for each group was based on a priori power analyses using GPower v3.1 based on an α size of 0.5, power of 0.8, and effect sizes estimated from preliminary data or prior studies. We used both parametric (1- and 2-way ANOVA) for normally distributed and non-parametric (Kruskal

bioRxiv preprint doi: https://doi.org/10.1101/2020.11.23.394098; this version posted November 23, 2020. The copyright holder for this preprint (which was not certified by peer review) is the author/funder, who has granted bioRxiv a license to display the preprint in perpetuity. It is made available under aCC-BY 4.0 International license.

Wallace) statistical methods for interval data to test for differences between groups followed by pairwise multiple comparisons tests as indicated in the text. Outliers for immune data in Figs. 6 and 7 were excluded via the ROUT method (Q=2%). The specific analyses used for each data set is noted in each figure legend. For all figures: * $p \leq 0.05$, ** $p<0.01$, *** $p<0.001$, **** $p<0.0001$. Data are represented as mean ± SEM. All figures and statistical analyses were completed using Excel (Microsoft) or Prism v8 (Graphpad).

5.0 Acknowledgements

We would like to thank the UCLA Behavioral Core, especially Irina Zhuravka for her efforts assaying behavioral deficits in the mice.

6.0 Competing interests

The authors declare that no competing interests exist.

7.0 Citations

Aguilar, Mary Jane, Shigehiko Kamoshita, Benjamin H. Landing, Elena Boder, and Robert P. Sedgwick. 1968. 'Pathological Observations in Ataxia-Telangiectasia: A Report on Five Cases*', *Journal of Neuropathology and Experimental Neurology*, 27: 659-76.

Ahel, I., U. Rass, S. F. El-Khamisy, S. Katyal, P. M. Clements, P. J. McKinnon, K. W. Caldecott, and S. C. West. 2006. 'The neurodegenerative disease protein aprataxin resolves abortive DNA ligation intermediates', *Nature*, 443: 713-6.

Aicardi, J., C. Barbosa, E. Andermann, F. Andermann, R. Morcos, Q. Ghanem, Y. Fukuyama, Y. Awaya, and P. Moe. 1988. 'Ataxia-ocular motor apraxia: a syndrome mimicking ataxia-telangiectasia', *Annals of Neurology*, 24: 497-502.

Ando, K., J. L. Kernan, P. H. Liu, T. Sanda, E. Logette, J. Tschopp, A. T. Look, J. Wang, L. Bouchier-Hayes, and S. Sidi. 2012. 'PIDD death-domain phosphorylation by ATM controls prodeath versus prosurvival PIDDosome signaling', *Molecular Cell*, 47: 681-93.

Apps, Richard, and Martin Garwicz. 2005. 'Anatomical and physiological foundations of cerebellar information processing', *Nature Reviews Neuroscience*, 6: 297-311.

Barlow, C., S. Hirotsune, R. Paylor, M. Liyanage, M. Eckhaus, F. Collins, Y. Shiloh, J. N. Crawley, T. Ried, D. Tagle, and A. Wynshaw-Boris. 1996. 'Atm-deficient mice: a paradigm of ataxia telangiectasia', *Cell*, 86: 159-71.

Beraldi, R., D. K. Meyerholz, A. Savinov, A. D. Kovacs, J. M. Weimer, J. A. Dykstra, R. D. Geraets, and D. A. Pearce. 2017. 'Genetic ataxia telangiectasia porcine model phenocopies the multisystemic features of the human disease', *Biochim Biophys Acta Mol Basis Dis*, 1863: 2862-70.

Bhatt, Jayesh M., and Andrew Bush. 2014. 'Microbiological surveillance in lung disease in ataxia telangiectasia', *European Respiratory Journal*, 43: 1797-801.

bioRxiv preprint doi: https://doi.org/10.1101/2020.11.23.394098; this version posted November 23, 2020. The copyright holder for this preprint (which was not certified by peer review) is the author/funder, who has granted bioRxiv a license to display the preprint in perpetuity. It is made available under aCC-BY 4.0 International license.

Boder, Elena, and Robert P. Sedgwick. 1958. 'ATAXIA-TELANGIECTASIA', *A Familial Syndrome of Progressive Cerebellar Ataxia, Oculocutaneous Telangiectasia and Frequent Pulmonary Infection*, 21: 526-54.

Bogue, M. A., C. Wang, C. Zhu, and D. B. Roth. 1997. 'V(D)J recombination in Ku86-deficient mice: distinct effects on coding, signal, and hybrid joint formation', *Immunity*, 7: 37-47.

Bredemeyer, Andrea L, Girdhar G Sharma, Ching-Yu Huang, Beth A Helmink, Laura M Walker, Katrina C Khor, Beth Nuskey, Kathleen E Sullivan, Tej K Pandita, and Craig H Bassing. 2006. 'ATM stabilizes DNA double-strand-break complexes during V (D) J recombination', *Nature*, 442: 466-70.

Browne, Susan E., L. Jackson Roberts, Phyllis A. Dennery, Susan R. Doctrow, M. Flint Beal, Carrolee Barlow, and Rodney L. Levine. 2004. 'Treatment with a catalytic antioxidant corrects the neurobehavioral defect in ataxia–telangiectasia mice', *Free Radical Biology and Medicine*, 36: 938-42.

Campbell, A., B. Krupp, J. Bushman, M. Noble, C. Pröschel, and M. Mayer-Pröschel. 2015. 'A novel mouse model for ataxia-telangiectasia with a N-terminal mutation displays a behavioral defect and a low incidence of lymphoma but no increased oxidative burden', *Human Molecular Genetics*, 24: 6331-49.

Campbell, Andrew, Jared Bushman, Joshua Munger, Mark Noble, Christoph Pröschel, and Margot Mayer-Pröschel. 2016. 'Mutation of ataxia–telangiectasia mutated is associated with dysfunctional glutathione homeostasis in cerebellar astroglia', *Glia*, 64: 227-39.

Chao, Connie, Eva Marie Yang, and Yang Xu. 2000. 'Rescue of Defective T Cell Development and Function in Atm^{−/−} Mice by a Functional TCRαβ Transgene', *The Journal of Immunology*, 164: 345-49.

Chen, Philip, Cheng Peng, John Luff, Kevin Spring, Dianne Watters, Steven Bottle, Shigeki Furuya, and Martin F. Lavin. 2003. 'Oxidative Stress Is Responsible for Deficient Survival and Dendritogenesis in Purkinje Neurons from Ataxia-Telangiectasia Mutated Mutant Mice', *The Journal of Neuroscience*, 23: 11453-60.

Clements, P. M., C. Breslin, E. D. Deeks, P. J. Byrd, L. Ju, P. Bieganowski, C. Brenner, M. C. Moreira, A. M. Taylor, and K. W. Caldecott. 2004. 'The ataxia-oculomotor apraxia 1 gene product has a role distinct from ATM and interacts with the DNA strand break repair proteins XRCC1 and XRCC4', *DNA Repair (Amst)*, 3: 1493-502.

Coffman, Keith A., Richard P. Dum, and Peter L. Strick. 2011. 'Cerebellar vermis is a target of projections from the motor areas in the cerebral cortex', *Proceedings of the National Academy of Sciences*, 108: 16068-73.

Concannon, P., and R. A. Gatti. 1997. 'Diversity of ATM gene mutations detected in patients with ataxia-telangiectasia', *Human Mutation*, 10: 100-7.

Cook, Anna A., Eviatar Fields, and Alanna J. Watt. 2020. 'Losing the Beat: Contribution of Purkinje Cell Firing Dysfunction to Disease, and Its Reversal', *Neuroscience*.

Crawford, T. O., R. L. Skolasky, R. Fernandez, K. J. Rosquist, and H. M. Lederman. 2006. 'Survival probability in ataxia telangiectasia', *Archives of Disease in Childhood*, 91: 610-11.

Dineen, Rob A., Felix Raschke, Hannah L. McGlashan, Stefan Pszczolkowski, Lorna Hack, Andrew D. Cooper, Manish Prasad, Gabriel Chow, William P. Whitehouse, and Dorothee P. Auer. 2020. 'Multiparametric cerebellar imaging and clinical phenotype in childhood ataxia telangiectasia', *NeuroImage: Clinical*, 25: 102110.

Du, L., M. E. Jung, R. Damoiseaux, G. Completo, F. Fike, J. M. Ku, S. Nahas, C. Piao, H. Hu, and R. A. Gatti. 2013. 'A new series of small molecular weight compounds induce read through of all three types of nonsense mutations in the ATM gene', *Molecular Therapy*, 21: 1653-60.

Elson, A., Y. Wang, C. J. Daugherty, C. C. Morton, F. Zhou, J. Campos-Torres, and P. Leder. 1996. 'Pleiotropic defects in ataxia-telangiectasia protein-deficient mice', *Proceedings of the National Academy of Sciences of the United States of America*, 93: 13084-9.

Gatti, R. A., and H. V. Vinters. 1985. 'Cerebellar pathology in ataxia-telangiectasia: the significance of basket cells', *Kroc Foundation Series*, 19: 225-32.

Genik, P. C., H. Bielefeldt-Ohmann, X. Liu, M. D. Story, L. Ding, J. M. Bush, C. M. Fallgren, and M. M. Weil. 2014. 'Strain background determines lymphoma incidence in Atm knockout mice', *Neoplasia*, 16: 129-36.

Germain, Ronald N. 2002. 'T-cell development and the CD4–CD8 lineage decision', *Nature Reviews Immunology*, 2: 309-22.

Gilad, Shlomit, Rami Khosravi, Dganit Shkedy, Tamar Uziel, Yael Ziv, Kinneret Savitsky, Galit Rotman, Sara Smith, Luciana Chessa, Timothy J. Jorgensen, Reli Harnik, Moshe Frydman, Ozden Sanal, Sima Portnoi, Zipora

bioRxiv preprint doi: https://doi.org/10.1101/2020.11.23.394098; this version posted November 23, 2020. The copyright holder for this preprint (which was not certified by peer review) is the author/funder, who has granted bioRxiv a license to display the preprint in perpetuity. It is made available under aCC-BY 4.0 International license.

Goldwicz, N. G. J. Jaspers, Richard A. Gatti, Gilbert Lenoir, Martin F. Lavin, Kouichi Tatsumi, Rolf D. Wegner, Yosef Shiloh, and Anat Bar-Shira. 1996. 'Predominance of Null Mutations in Ataxia-Telangiectasia', *Human Molecular Genetics*, 5: 433-39.

Guo, Zhi, Sergei Kozlov, Martin F. Lavin, Maria D. Person, and Tanya T. Paull. 2010. 'ATM Activation by Oxidative Stress', *Science*, 330: 517-21.

Hathcock, K. S., S. Bowen, F. Livak, and R. J. Hodes. 2013. 'ATM influences the efficiency of TCRbeta rearrangement, subsequent TCRbeta-dependent T cell development, and generation of the pre-selection TCRbeta CDR3 repertoire', *PloS One*, 8: e62188.

Herzog, Karl-Heinz, Miriam J. Chong, Manuela Kapsetaki, James I. Morgan, and Peter J. McKinnon. 1998. 'Requirement for Atm in Ionizing Radiation-Induced Cell Death in the Developing Central Nervous System', *Science*, 280: 1089-91.

Hoche, F., K. Seidel, M. Theis, S. Vlaho, R. Schubert, S. Zielen, and M. Kieslich. 2012. 'Neurodegeneration in ataxia telangiectasia: what is new? What is evident?', *Neuropediatrics*, 43: 119-29.

Jackson, Thomas J, Gabriel Chow, Mohnish Suri, Philip Byrd, Malcolm R Taylor, and William P Whitehouse. 2016. 'Longitudinal analysis of the neurological features of ataxia-telangiectasia', *Developmental Medicine and Child Neurology*, 58: 690-97.

Kaminsky, Natalie, Ofer Bihari, Sivan Kanner, and Ari Barzilai. 2016. 'Connecting Malfunctioning Glial Cells and Brain Degenerative Disorders', *Genomics, Proteomics & Bioinformatics*, 14: 155-65.

Kastan, M. B., and J. Bartek. 2004. 'Cell-cycle checkpoints and cancer', *Nature*, 432: 316-23.

Kim, Jusik, Keeeun Kim, Jung-Soon Mo, and Youngsoo Lee. 2020. 'Atm deficiency in the DNA polymerase β null cerebellum results in cerebellar ataxia and Itpr1 reduction associated with alteration of cytosine methylation', *Nucleic Acids Research*, 48: 3678-91.

Krangel, Michael S. 2009. 'Mechanics of T cell receptor gene rearrangement', *Current Opinion in Immunology*, 21: 133-39.

Lavin, M. F. 2013. 'The appropriateness of the mouse model for ataxia-telangiectasia: neurological defects but no neurodegeneration', *DNA Repair (Amst)*, 12: 612-9.

Levy, Ariel, and Anthony E. Lang. 2018. 'Ataxia-telangiectasia: A review of movement disorders, clinical features, and genotype correlations', *Movement Disorders*, 33: 1238-47.

Li, J., Y. R. Han, M. R. Plummer, and K. Herrup. 2009. 'Cytoplasmic ATM in neurons modulates synaptic function', *Current Biology*, 19: 2091-6.

Livák, Ferenc, Michelle Tourigny, David G. Schatz, and Howard T. Petrie. 1999. 'Characterization of TCR Gene Rearrangements During Adult Murine T Cell Development', *The Journal of Immunology*, 162: 2575-80.

Machado, Ana S, Dana M Darmohray, Joao Fayad, Hugo G Marques, and Megan R Carey. 2015. 'A quantitative framework for whole-body coordination reveals specific deficits in freely walking ataxic mice', *Elife*, 4: e07892.

Matei, I. R., C. J. Guidos, and J. S. Danska. 2006. 'ATM-dependent DNA damage surveillance in T-cell development and leukemogenesis: the DSB connection', *Immunological Reviews*, 209: 142-58.

Matsuoka, Shuhei, Bryan A. Ballif, Agata Smogorzewska, E. Robert McDonald, Kristen E. Hurov, Ji Luo, Corey E. Bakalarski, Zhenming Zhao, Nicole Solimini, Yaniv Lerenthal, Yosef Shiloh, Steven P. Gygi, and Stephen J. Elledge. 2007. 'ATM and ATR Substrate Analysis Reveals Extensive Protein Networks Responsive to DNA Damage', *Science*, 316: 1160-66.

McKinnon, P. J. 2009. 'DNA repair deficiency and neurological disease', *Nature Reviews: Neuroscience*, 10: 100-12.

Micol, R., L. Ben Slama, F. Suarez, L. Le Mignot, J. Beauté, N. Mahlaoui, C. Dubois d'Enghien, A. Laugé, J. Hall, J. Couturier, L. Vallée, B. Delobel, F. Rivier, K. Nguyen, T. Billette de Villemeur, J. L. Stephan, P. Bordigoni, Y. Bertrand, N. Aladjidi, J. M. Pedespan, C. Thomas, I. Pellier, M. Koenig, O. Hermine, C. Picard, D. Moshous, B. Neven, F. Lanternier, S. Blanche, M. Tardieu, M. Debré, A. Fischer, and D. Stoppa-Lyonnet. 2011. 'Morbidity and mortality from ataxia-telangiectasia are associated with ATM genotype', *Journal of Allergy and Clinical Immunology*, 128: 382-9.e1.

Moreira, M. C., S. Klur, M. Watanabe, A. H. Németh, I. Le Ber, J. C. Moniz, C. Tranchant, P. Aubourg, M. Tazir, L. Schöls, M. Pandolfo, J. B. Schulz, J. Pouget, P. Calvas, M. Shizuka-Ikeda, M. Shoji, M. Tanaka, L. Izatt, C. E.

bioRxiv preprint doi: https://doi.org/10.1101/2020.11.23.394098; this version posted November 23, 2020. The copyright holder for this preprint (which was not certified by peer review) is the author/funder, who has granted bioRxiv a license to display the preprint in perpetuity. It is made available under aCC-BY 4.0 International license.

Shaw, A. M'Zahem, E. Dunne, P. Bomont, T. Benhassine, N. Bouslam, G. Stevanin, A. Brice, J. Guimarães, P. Mendonça, C. Barbot, P. Coutinho, J. Sequeiros, A. Dürr, J. M. Warter, and M. Koenig. 2004. 'Senataxin, the ortholog of a yeast RNA helicase, is mutant in ataxia-ocular apraxia 2', *Nature Genetics*, 36: 225-7.

Morrell, Daphne, Elizabeth Cromartie, and Michael Swift. 1986. 'Mortality and cancer incidence in 263 patients with ataxia-telangiectasia', *Journal of the National Cancer Institute*, 77: 89-92.

Petersen, Andrew J., Stacey A. Rimkus, and David A. Wassarman. 2012. 'ATM kinase inhibition in glial cells activates the innate immune response and causes neurodegeneration in Drosophila', *Proceedings of the National Academy of Sciences*, 109: E656-E64.

Pizzamiglio, L., E. Focchi, and F. Antonucci. 2020. 'ATM Protein Kinase: Old and New Implications in Neuronal Pathways and Brain Circuitry', *Cells*, 9.

Quarantelli, Mario, Giuliana Giardino, Anna Prinster, Giuseppina Aloj, Barbara Carotenuto, Emilia Cirillo, Angela Marsili, Elena Salvatore, Ennio Del Giudice, and Claudio Pignata. 2013. 'Steroid treatment in Ataxia-Telangiectasia induces alterations of functional magnetic resonance imaging during prono-supination task', *European Journal of Paediatric Neurology*, 17: 135-40.

Quek, Hazel, John Luff, KaGeen Cheung, Sergei Kozlov, Magtouf Gatei, C. Soon Lee, Mark C. Bellingham, Peter G. Noakes, Yi Chieh Lim, Nigel L. Barnett, Steven Dingwall, Ernst Wolvetang, Tomoji Mashimo, Tara L. Roberts, and Martin F. Lavin. 2016. 'A rat model of ataxia-telangiectasia: evidence for a neurodegenerative phenotype', *Human Molecular Genetics*, 26: 109-23.

Rashi-Elkeles, S., R. Elkon, N. Weizman, C. Linhart, N. Amariglio, G. Sternberg, G. Rechavi, A. Barzilai, R. Shamir, and Y. Shiloh. 2006. 'Parallel induction of ATM-dependent pro- and antiapoptotic signals in response to ionizing radiation in murine lymphoid tissue', *Oncogene*, 25: 1584-92.

Rass, Ulrich, Ivan Ahel, and Stephen C. West. 2007. 'Defective DNA Repair and Neurodegenerative Disease', *Cell*, 130: 991-1004.

Rogers, D. C., E. M. Fisher, S. D. Brown, J. Peters, A. J. Hunter, and J. E. Martin. 1997. 'Behavioral and functional analysis of mouse phenotype: SHIRPA, a proposed protocol for comprehensive phenotype assessment', *Mammalian Genome*, 8: 711-3.

Rothblum-Oviatt, Cynthia, Jennifer Wright, Maureen A. Lefton-Greif, Sharon A. McGrath-Morrow, Thomas O. Crawford, and Howard M. Lederman. 2016. 'Ataxia telangiectasia: a review', *Orphanet Journal of Rare Diseases*, 11: 159.

Sahama, Ishani, Kate Sinclair, Simona Fiori, James Doecke, Kerstin Pannek, Lee Reid, Martin Lavin, and Stephen Rose. 2015. 'Motor pathway degeneration in young ataxia telangiectasia patients: A diffusion tractography study', *NeuroImage: Clinical*, 9: 206-15.

Sahama, Ishani, Kate Sinclair, Kerstin Pannek, Martin Lavin, and Stephen Rose. 2014. 'Radiological imaging in ataxia telangiectasia: a review', *The Cerebellum*, 13: 521-30.

Sandoval, N., M. Platzer, A. Rosenthal, T. Dork, R. Bendix, B. Skawran, M. Stuhrmann, R. D. Wegner, K. Sperling, S. Banin, Y. Shiloh, A. Baumer, U. Bernthaler, H. Sennefelder, M. Brohm, B. H. Weber, and D. Schindler. 1999. 'Characterization of ATM gene mutations in 66 ataxia telangiectasia families', *Human Molecular Genetics*, 8: 69-79.

Sanghez, Valentina, Anna Luzzi, Don Clarke, Dustin Kee, Steven Beuder, Danielle Rux, Mitsujiro Osawa, Joaquín Madrenas, Tsui-Fen Chou, Michael Kyba, and Michelina Iacovino. 2017. 'Notch activation is required for downregulation of HoxA3-dependent endothelial cell phenotype during blood formation', *PloS One*, 12: e0186818.

Savitsky, K., A. Bar-Shira, S. Gilad, G. Rotman, Y. Ziv, L. Vanagaite, D. A. Tagle, S. Smith, T. Uziel, S. Sfez, M. Ashkenazi, I. Pecker, M. Frydman, R. Harnik, S. R. Patanjali, A. Simmons, G. A. Clines, A. Sartiel, R. A. Gatti, L. Chessa, O. Sanal, M. F. Lavin, N. G. Jaspers, A. M. Taylor, C. F. Arlett, T. Miki, S. M. Weissman, M. Lovett, F. S. Collins, and Y. Shiloh. 1995. 'A single ataxia telangiectasia gene with a product similar to PI-3 kinase', *Science*, 268: 1749-53.

Schubert, R., J. Reichenbach, and S. Zielen. 2002. 'Deficiencies in CD4+ and CD8+ T cell subsets in ataxia telangiectasia', *Clinical and Experimental Immunology*, 129: 125-32.

bioRxiv preprint doi: https://doi.org/10.1101/2020.11.23.394098; this version posted November 23, 2020. The copyright holder for this preprint (which was not certified by peer review) is the author/funder, who has granted bioRxiv a license to display the preprint in perpetuity. It is made available under aCC-BY 4.0 International license.

Sedghi, Maryam, Mehri Salari, Ali-Reza Moslemi, Ariana Kariminejad, Mark Davis, Hayley Goullée, Björn Olsson, Nigel Laing, and Homa Tajsharghi. 2018. 'Ataxia-telangiectasia-like disorder in a family deficient for MRE11A, caused by a MRE11 variant', *Neurology Genetics*, 4: e295.

Shiloh, Yosef, and Yael Ziv. 2013. 'The ATM protein kinase: regulating the cellular response to genotoxic stress, and more', *Nature Reviews Molecular Cell Biology*, 14: 197-210.

Spring, K., S. Cross, C. Li, D. Watters, L. Ben-Senior, P. Waring, F. Ahangari, S. L. Lu, P. Chen, I. Misko, C. Paterson, G. Kay, N. I. Smorodinsky, Y. Shiloh, and M. F. Lavin. 2001. 'Atm knock-in mice harboring an in-frame deletion corresponding to the human ATM 7636del9 common mutation exhibit a variant phenotype', *Cancer Research*, 61: 4561-8.

Staples, E. R., E. M. McDermott, A. Reiman, P. J. Byrd, S. Ritchie, A. M. Taylor, and E. G. Davies. 2008. 'Immunodeficiency in ataxia telangiectasia is correlated strongly with the presence of two null mutations in the ataxia telangiectasia mutated gene', *Clinical and Experimental Immunology*, 153: 214-20.

Starczynski, Jane, William Simmons, Joanne R. Flavell, Phillip J. Byrd, Grant S. Stewart, Harjit S. Kullar, Alix Groom, John Crocker, Paul A. H. Moss, Gary M. Reynolds, Meri Glavina-Durdov, A. Malcolm R. Taylor, Christopher Fegan, Tatjana Stankovic, and Paul G. Murray. 2003. 'Variations in ATM protein expression during normal lymphoid differentiation and among B-cell-derived neoplasias', *The American journal of pathology*, 163: 423-32.

Swift, M., D. Morrell, E. Cromartie, A. R. Chamberlin, M. H. Skolnick, and D. T. Bishop. 1986. 'The incidence and gene frequency of ataxia-telangiectasia in the United States', *American Journal of Human Genetics*, 39: 573-83.

Takashima, H., C. F. Boerkoel, J. John, G. M. Saifi, M. A. Salih, D. Armstrong, Y. Mao, F. A. Quiocho, B. B. Roa, M. Nakagawa, D. W. Stockton, and J. R. Lupski. 2002. 'Mutation of TDP1, encoding a topoisomerase I-dependent DNA damage repair enzyme, in spinocerebellar ataxia with axonal neuropathy', *Nature Genetics*, 32: 267-72.

Tal, Efrat, Marina Alfo, Shan Zha, Ari Barzilai, Chris I. De Zeeuw, Yael Ziv, and Yosef Shiloh. 2018. 'Inactive Atm abrogates DSB repair in mouse cerebellum more than does Atm loss, without causing a neurological phenotype', *DNA Repair*, 72: 10-17.

Tavani, F., R. A. Zimmerman, G. T. Berry, K. Sullivan, R. Gatti, and P. Bingham. 2003. 'Ataxia-telangiectasia: the pattern of cerebellar atrophy on MRI', *Neuroradiology*, 45: 315-19.

Vacchio, Melanie S., Alexandru Olaru, Ferenc Livak, and Richard J. Hodes. 2007. 'ATM deficiency impairs thymocyte maturation because of defective resolution of T cell receptor α locus coding end breaks', *Proceedings of the National Academy of Sciences*, 104: 6323-28.

Vail, Graham, Aifang Cheng, Yu Ray Han, Teng Zhao, Shengwang Du, Michael M. T. Loy, Karl Herrup, and Mark R. Plummer. 2016. 'ATM protein is located on presynaptic vesicles and its deficit leads to failures in synaptic plasticity', *Journal of Neurophysiology*, 116: 201-09.

Valentin-Vega, Y. A., and M. B. Kastan. 2012. 'A new role for ATM: regulating mitochondrial function and mitophagy', *Autophagy*, 8: 840-1.

van der Burgt, I, K H Chrzanowska, D Smeets, and C Weemaes. 1996. 'Nijmegen breakage syndrome', *Journal of Medical Genetics*, 33: 153-56.

Wallis, LI, PD Griffiths, SJ Ritchie, CAJ Romanowski, G Darwent, and ID Wilkinson. 2007. 'Proton spectroscopy and imaging at 3T in ataxia-telangiectasia', *American journal of neuroradiology*, 28: 79-83.

Weyemi, Urbain, Christophe E. Redon, Towqir Aziz, Rohini Choudhuri, Daisuke Maeda, Palak R. Parekh, Michael Y. Bonner, Jack L. Arbiser, and William M. Bonner. 2015. 'NADPH oxidase 4 is a critical mediator in Ataxia telangiectasia disease', *Proceedings of the National Academy of Sciences*, 112: 2121-26.

Xu, Y., and D. Baltimore. 1996. 'Dual roles of ATM in the cellular response to radiation and in cell growth control', *Genes and Development*, 10: 2401-10.

bioRxiv preprint doi: https://doi.org/10.1101/2020.11.23.394098; this version posted November 23, 2020. The copyright holder for this preprint (which was not certified by peer review) is the author/funder, who has granted bioRxiv a license to display the preprint in perpetuity. It is made available under aCC-BY 4.0 International license.

8.0 Figure Supplements

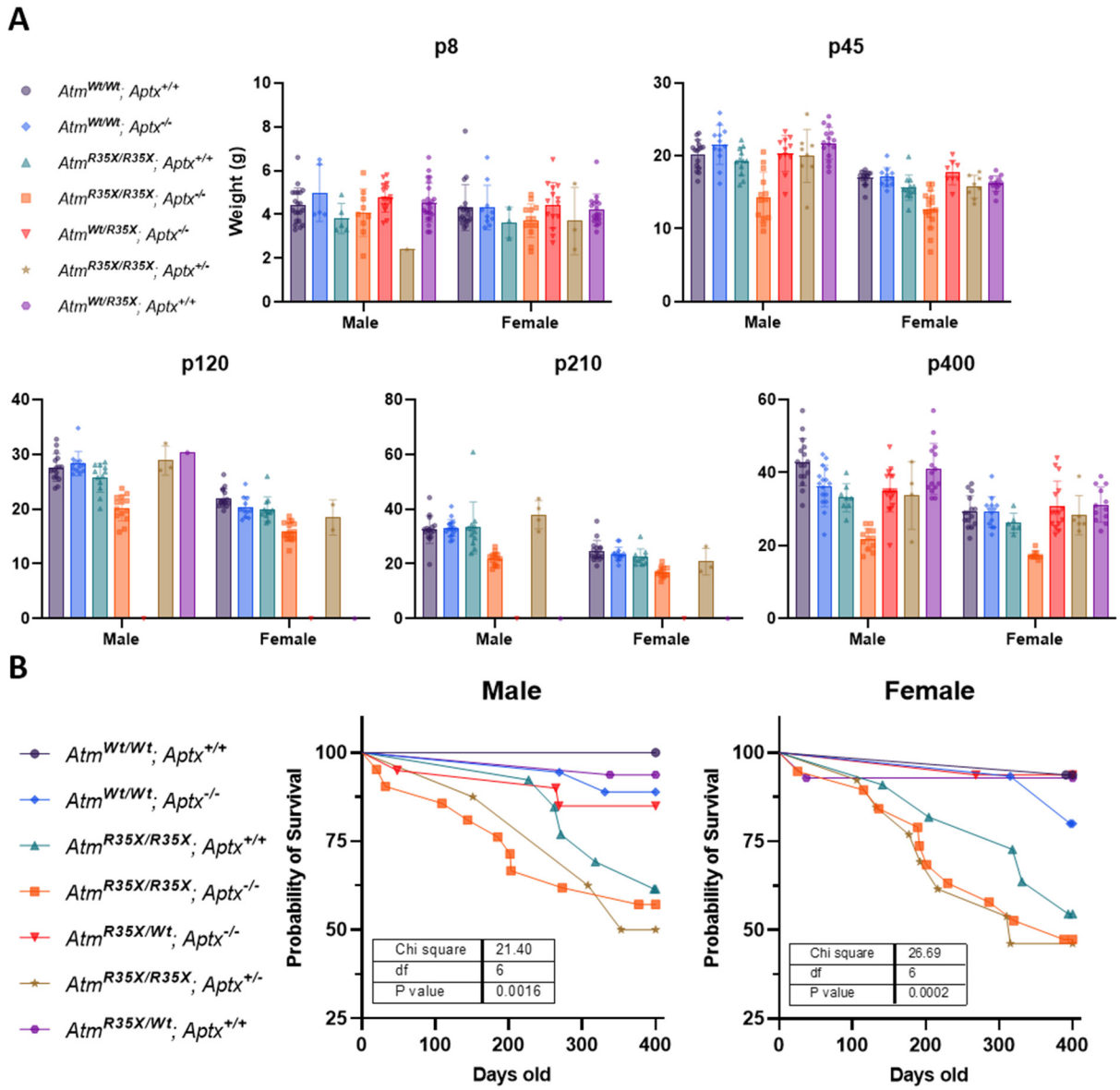

Figure 1-figure supplement 1. Animal weight for each time point and genotype. A) The average weights are plotted for each genotype at each of the indicated time points. Growth curves without experimental, 2-way ANOVA with age and genotype as factors. Male: $F_{(10, 226)} = 5.6$, $p < 0.0001$; Female: $F_{(10, 197)} = 7.3$, $p < 0.0001$ **B)** The survivability of each genotype of mice are plotted for male and female individually.

bioRxiv preprint doi: https://doi.org/10.1101/2020.11.23.394098; this version posted November 23, 2020. The copyright holder for this preprint (which was not certified by peer review) is the author/funder, who has granted bioRxiv a license to display the preprint in perpetuity. It is made available under aCC-BY 4.0 International license.

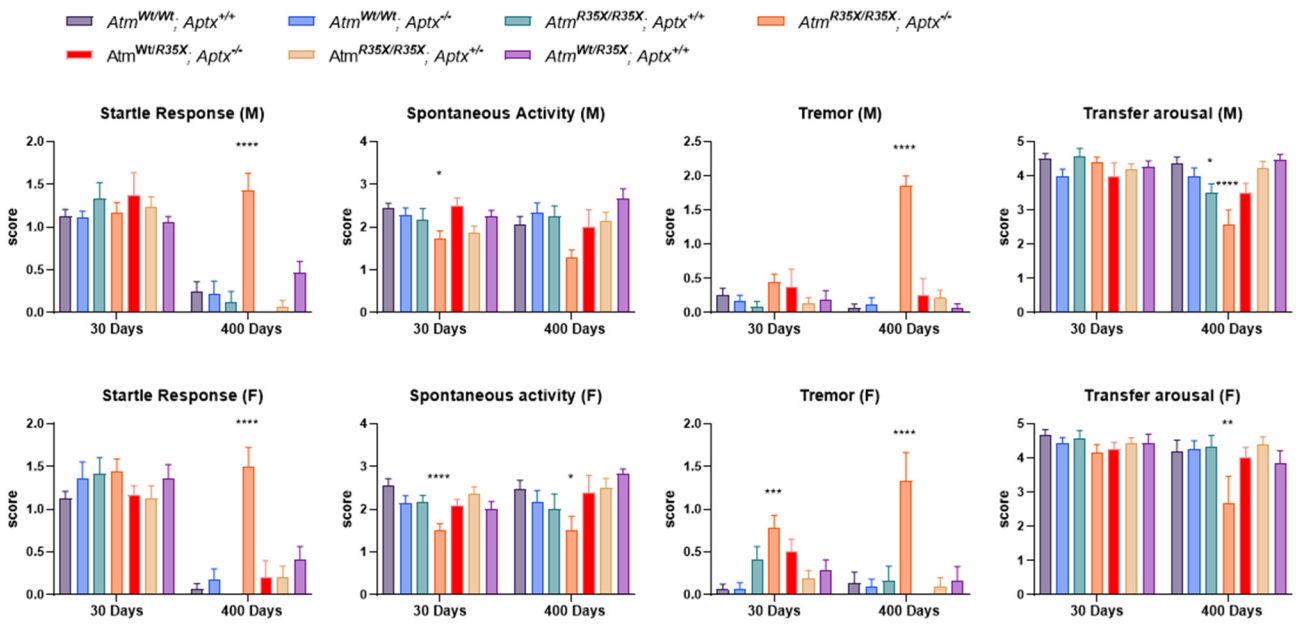

Figure 3-figure supplement 1. SHIRPA battery of behavioral tests. Behavioral deficits are seen only in *Atm*$^{R35X/R35X}$*; Aptx*$^{-/-}$ mice across all behavioral tests and sexes. Behavioral tests were examined using a non-parametric Kruskal Wallace followed by *posthoc* Dunn's multiple comparisons tests.

bioRxiv preprint doi: https://doi.org/10.1101/2020.11.23.394098; this version posted November 23, 2020. The copyright holder for this preprint (which was not certified by peer review) is the author/funder, who has granted bioRxiv a license to display the preprint in perpetuity. It is made available under aCC-BY 4.0 International license.

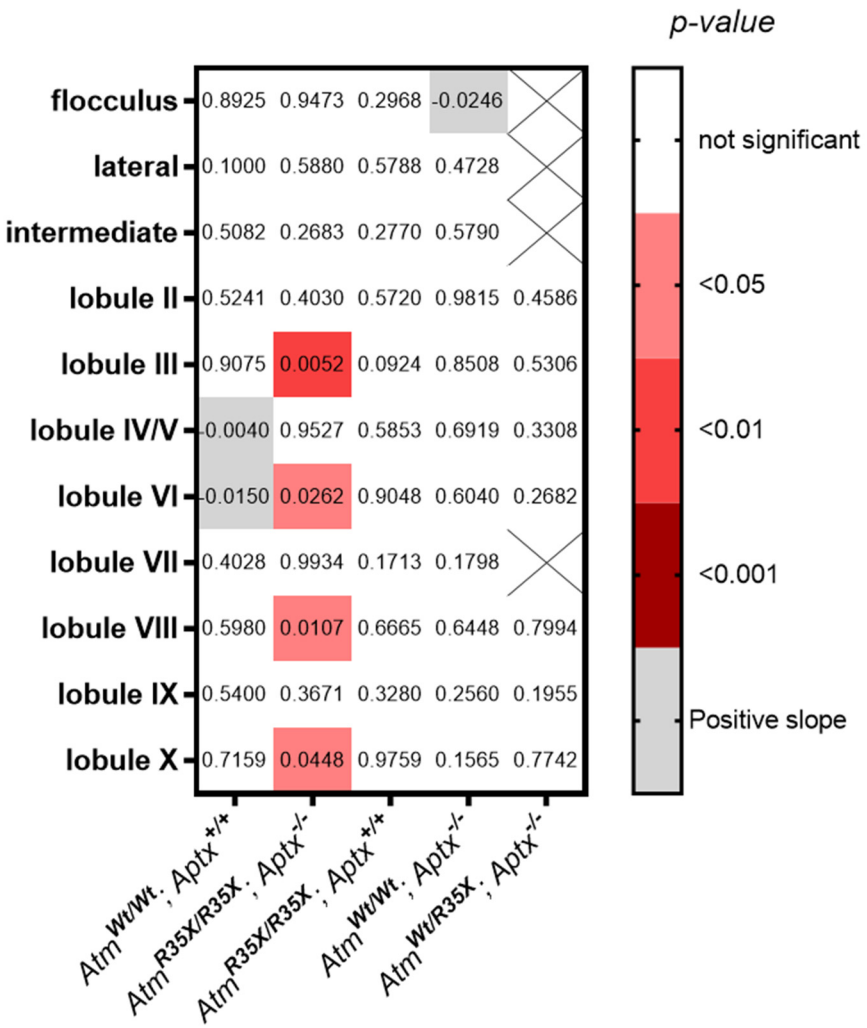

Figure 4-figure supplement 1. Heatmap showing significant PN firing frequency *vs.* age correlations in different lobules in *Atm*$^{R35X/R35X}$; *Aptx*$^{-/-}$ and control mice. Listed *p*-values indicate statistical differences from 0 based on linear regressions for the indicated lobules and areas. Red shaded boxes highlight *Atm*$^{R35X/R35X}$; *Aptx*$^{-/-}$ folia with significantly decreasing PN firing frequency over age. Grey boxes indicate regions where PN firing frequency increased with age.

bioRxiv preprint doi: https://doi.org/10.1101/2020.11.23.394098; this version posted November 23, 2020. The copyright holder for this preprint (which was not certified by peer review) is the author/funder, who has granted bioRxiv a license to display the preprint in perpetuity. It is made available under aCC-BY 4.0 International license.

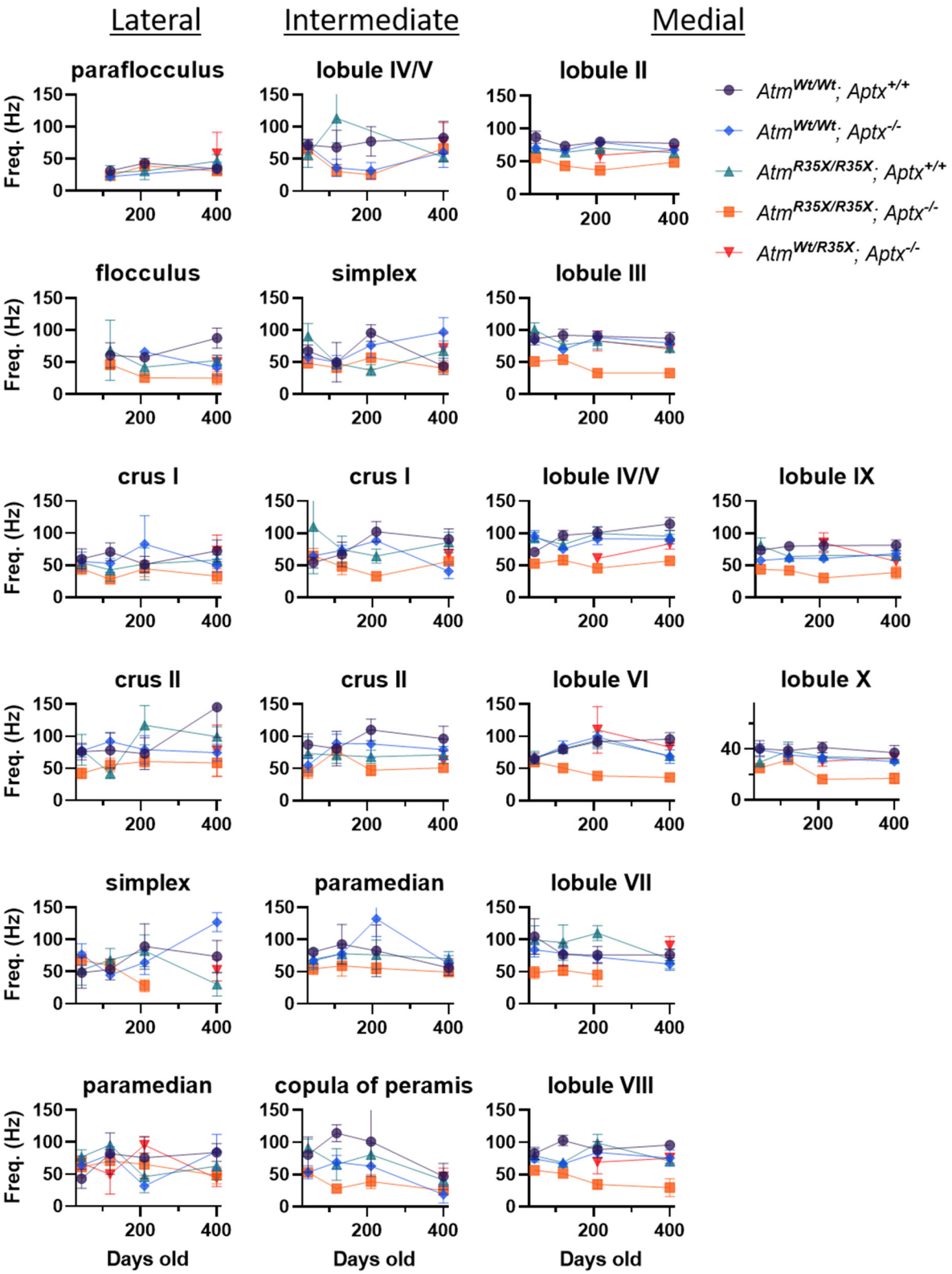

892

893 **Figure 4-figure supplement 2. Mean variation between PN firing intervals across the cerebellum.**

894 Average CV2 of PN firing frequency is plotted across the indicated locations at P45, 120, 210, and 400.

895

bioRxiv preprint doi: https://doi.org/10.1101/2020.11.23.394098; this version posted November 23, 2020. The copyright holder for this preprint (which was not certified by peer review) is the author/funder, who has granted bioRxiv a license to display the preprint in perpetuity. It is made available under aCC-BY 4.0 International license.

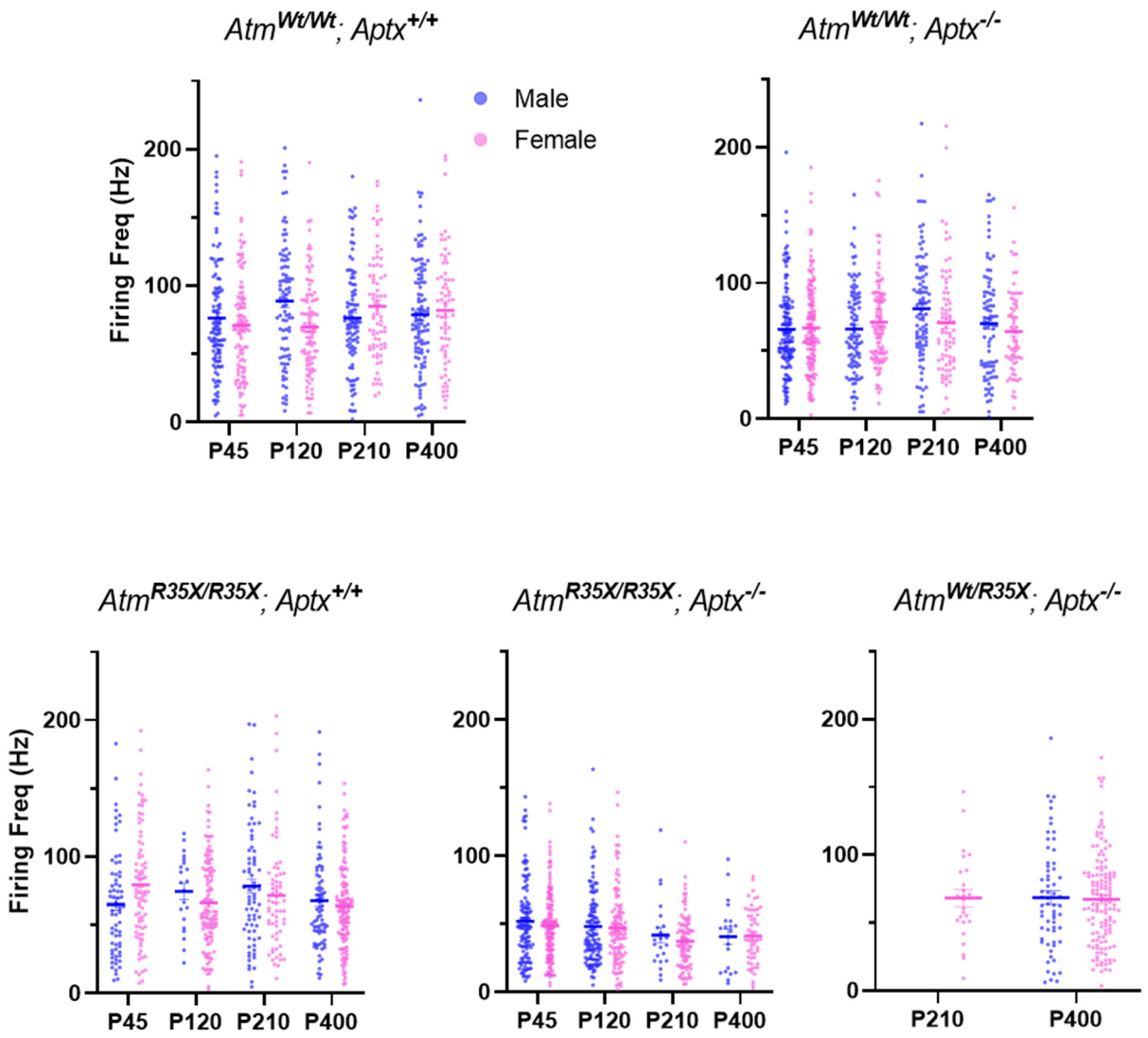

896

897 **Figure 4-figure supplement 3. Mean PN firing frequency across genotype and sex.** Average PN

898 firing frequency for all cells recorded from male and female mice is plotted for the indicated genotype. No

899 significant differences were observed between sex. 2-Way ANOVA with age and sex as factors, *Atm*$^{Wt/Wt}$*;*

900 *Aptx*$^{+/+}$ ($F_{(1, 751)} = 1.15$, *p=0.3*), *Atm*$^{Wt/Wt}$*; Aptx*$^{-/-}$ ($F_{(1, 797)} = 1.10$, *p=0.3*), *Atm*$^{R35X/R35X}$*; Aptx*$^{+/+}$ ($F_{(1, 630)} = 0.17$,

901 *p=0.7*), *Atm*$^{R35X/R35X}$*; Aptx*$^{-/-}$ ($F_{(1, 666)} = 1.10$, *p=0.4*), t-test for P400 *Atm*$^{Wt/R35X}$*; Aptx*$^{-/-}$ (*p=0.9*)

902

bioRxiv preprint doi: https://doi.org/10.1101/2020.11.23.394098; this version posted November 23, 2020. The copyright holder for this preprint (which was not certified by peer review) is the author/funder, who has granted bioRxiv a license to display the preprint in perpetuity. It is made available under aCC-BY 4.0 International license.

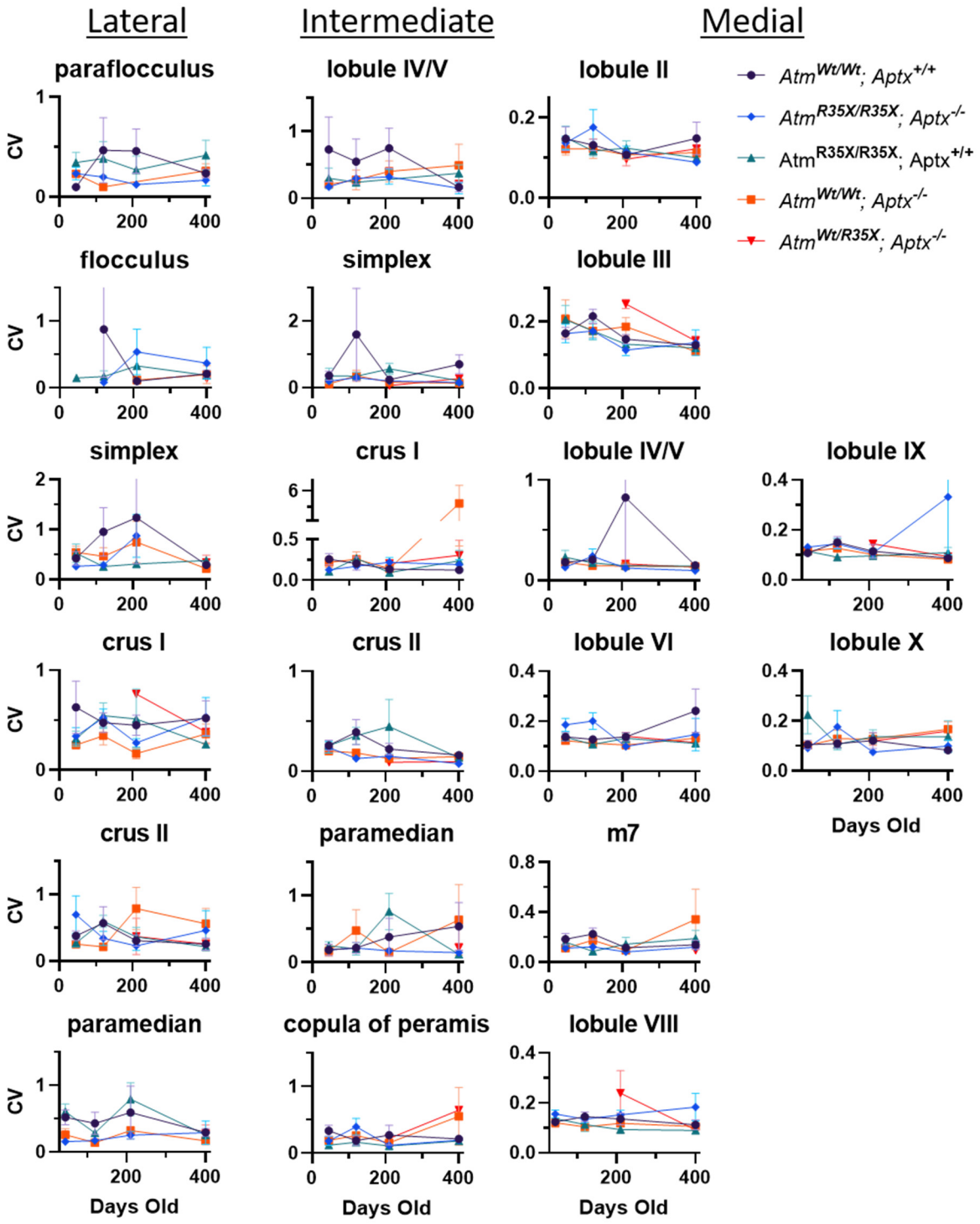

Figure 4-figure supplement 4. Coefficient of Variation of PN firing frequency across the cerebellum. Average CV of PN firing frequency is plotted across the indicated locations at P45, 120, 210, and 400. No significant differences (*p<0.5*) were detected across all areas using 2-way ANOVA with age and genotype as factors.

bioRxiv preprint doi: https://doi.org/10.1101/2020.11.23.394098; this version posted November 23, 2020. The copyright holder for this preprint (which was not certified by peer review) is the author/funder, who has granted bioRxiv a license to display the preprint in perpetuity. It is made available under aCC-BY 4.0 International license.

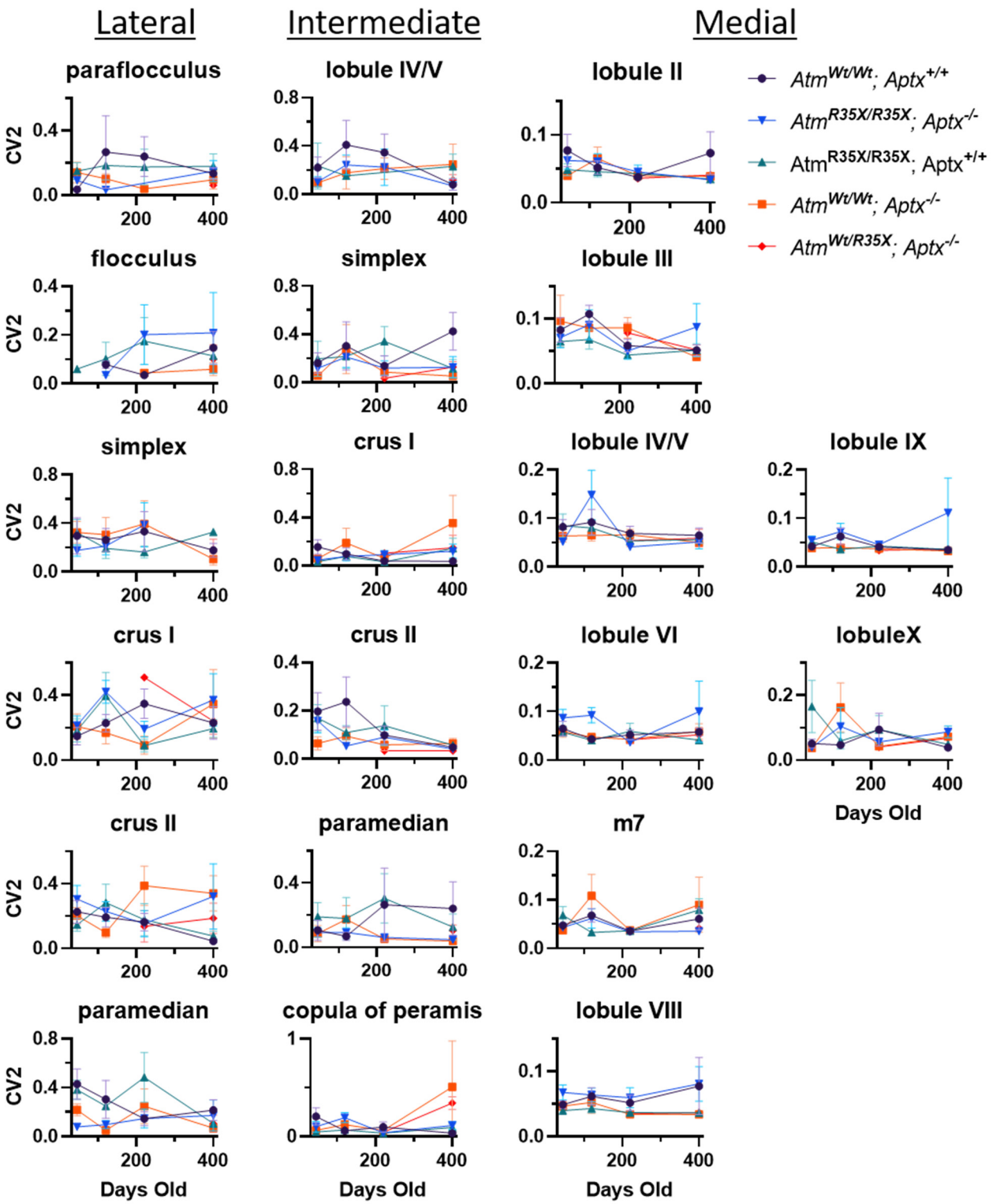

908 **Figure 4-figure supplement 5. Mean variation between PN firing intervals across the cerebellum.**

909 Average CV2 of PN firing frequency is plotted across the indicated locations at P45, 120, 210, and 400.

910 No significant differences (*p<0.5*) were detected across all areas using 2-way ANOVA with age and

911 genotype as factors.

bioRxiv preprint doi: https://doi.org/10.1101/2020.11.23.394098; this version posted November 23, 2020. The copyright holder for this preprint (which was not certified by peer review) is the author/funder, who has granted bioRxiv a license to display the preprint in perpetuity. It is made available under aCC-BY 4.0 International license.

9.0 Source files

Figure 2-Source Data 1. Weight, age of death, and probable cause of death

Figure 3-Source Data 1. Raw behavior data

Figure 4-Source Data 1. Individual average firing frequencies for each recorded cell

Figure 4-Source Data 2. Individual CV for each recorded cell

Figure 4-Source Data 3. Brain area, Purkinje neuron density, and cell diameter for each animal and cell

Figure 5/6-Source Data 1. Tables of FACs data

10.0 Rich Media

Video S1. Pole test, *Atm$^{Wt/Wt}$* vs. *Atm$^{R35X/R35X}$*. *Atm$^{R35X/R35X}$* do not display an ataxic phenotype at P460.

Video S2. Pole test, *Aptx$^{+/+}$* vs. *Aptx$^{-/-}$*. *Aptx$^{-/-}$* mice do not display an ataxic phenotype at P460.

Video S3. Pole test, *Atm$^{Wt/Wt}$; Aptx$^{+/+}$* vs. *Atm$^{R35X/R35X}$; Aptx$^{-/-}$*. *Atm$^{R35X/R35X}$; Aptx$^{-/-}$* have considerable motor disability at P460.

Video S4. Open field, *Atm$^{Wt/Wt}$; Aptx$^{+/+}$* vs. *Atm$^{R35X/R35X}$; Aptx$^{-/-}$*. *Atm$^{R35X/R35X}$; Aptx$^{-/-}$* display a clear inability to ambulate in the open field at P460.

Fig. 1

bioRxiv preprint doi: https://doi.org/10.1101/2020.11.23.394098; this version posted November 23, 2020. The copyright holder for this preprint (which was not certified by peer review) is the author/funder, who has granted bioRxiv a license to display the preprint in perpetuity. It is made available under aCC-BY 4.0 International license.

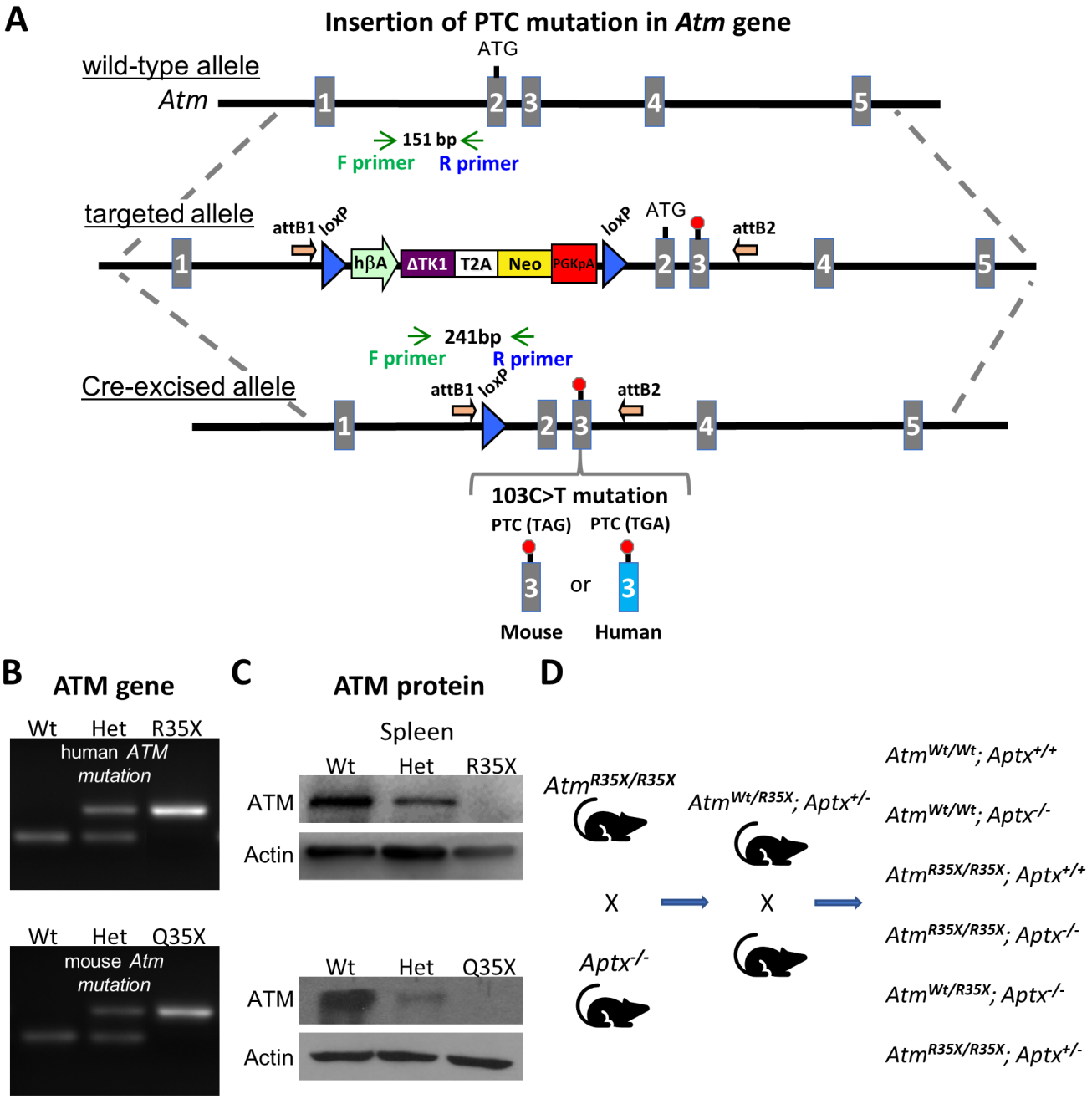

Fig. 2

bioRxiv preprint doi: https://doi.org/10.1101/2020.11.23.394098; this version posted November 23, 2020. The copyright holder for this preprint (which was not certified by peer review) is the author/funder, who has granted bioRxiv a license to display the preprint in perpetuity. It is made available under aCC-BY 4.0 International license.

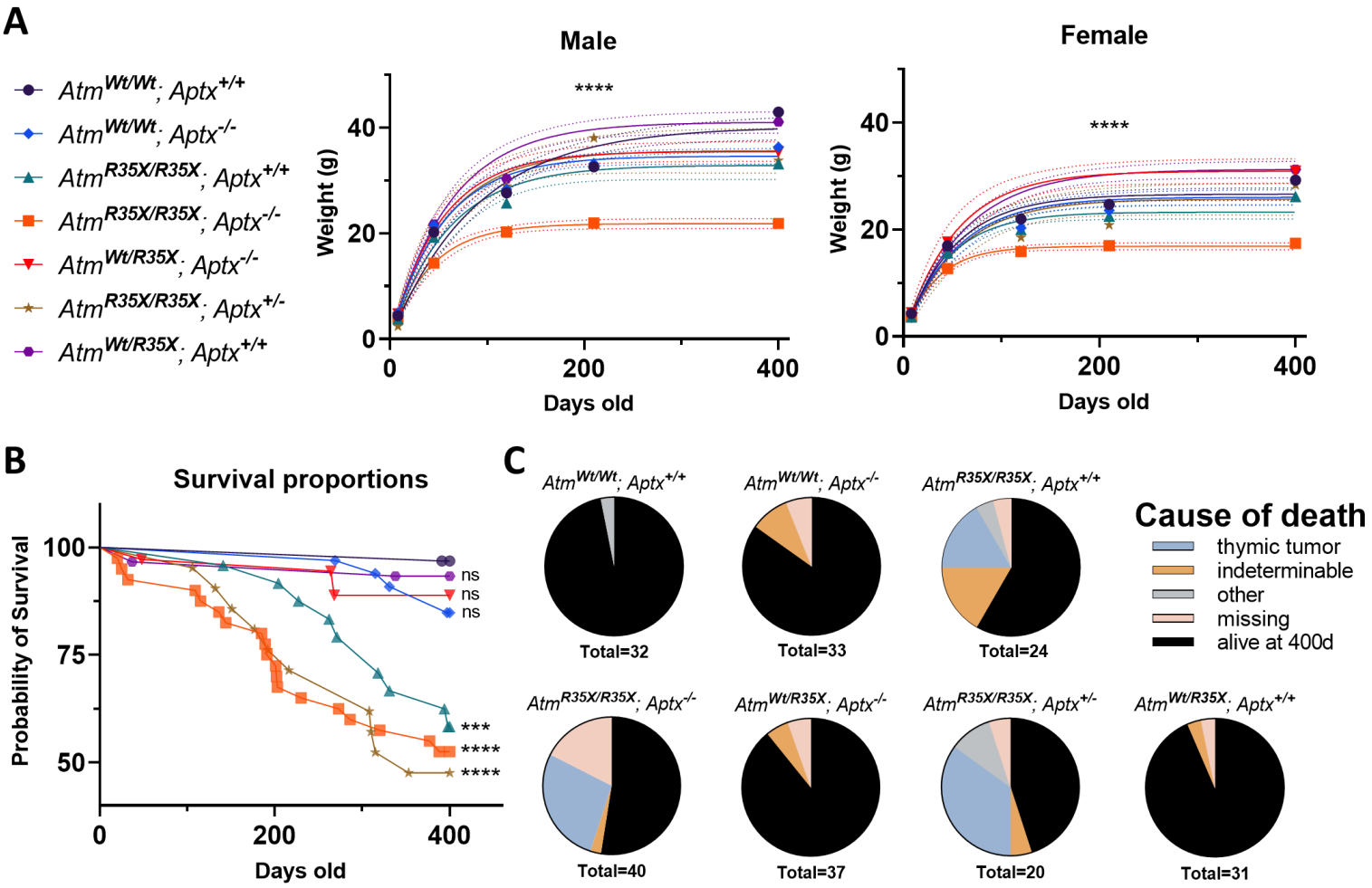

Figure 2-figure supplement 1

bioRxiv preprint doi: https://doi.org/10.1101/2020.11.23.394098; this version posted November 23, 2020. The copyright holder for this preprint (which was not certified by peer review) is the author/funder, who has granted bioRxiv a license to display the preprint in perpetuity. It is made available under aCC-BY 4.0 International license.

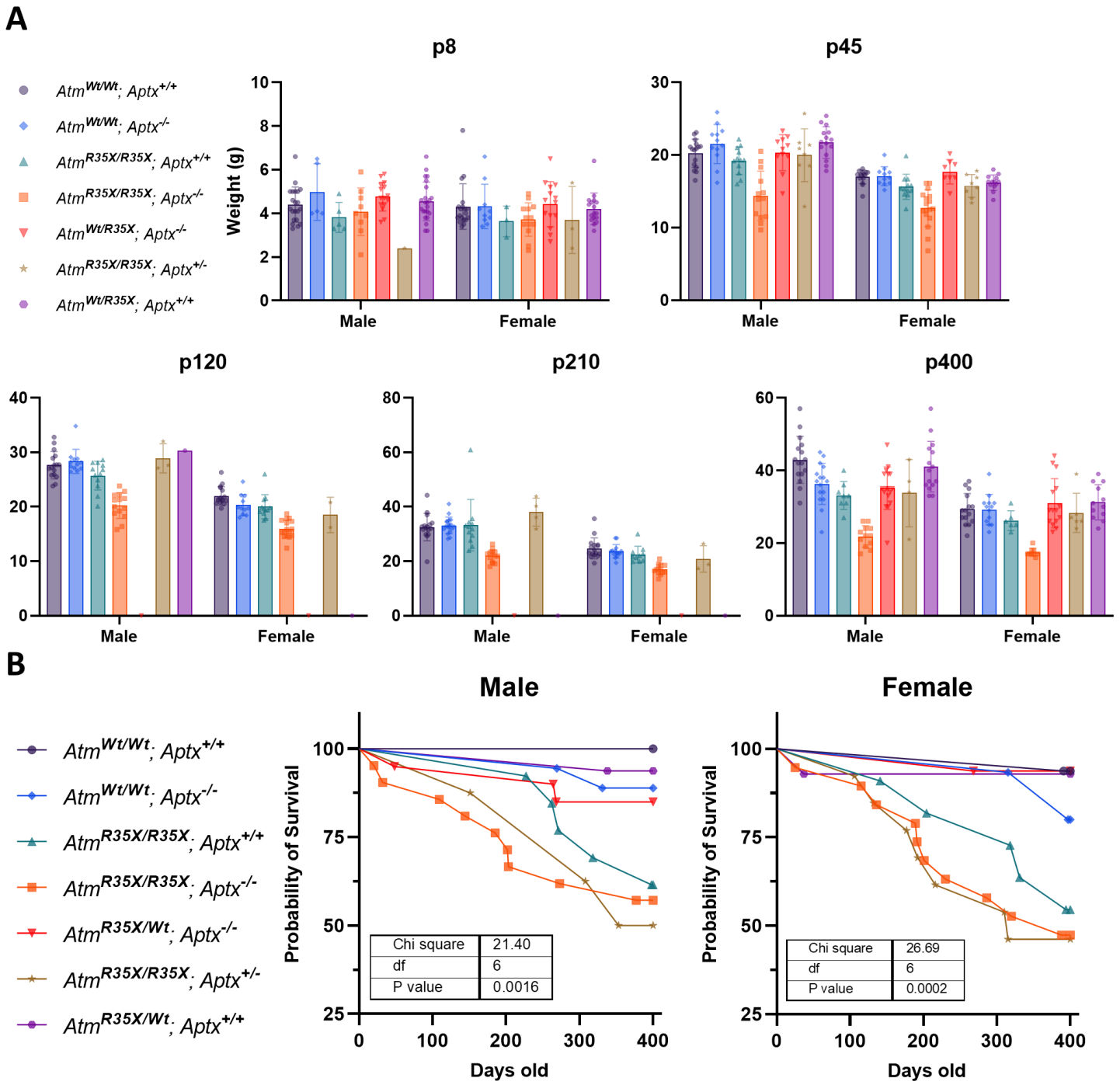

Fig. 3

bioRxiv preprint doi: https://doi.org/10.1101/2020.11.23.394098; this version posted November 23, 2020. The copyright holder for this preprint (which was not certified by peer review) is the author/funder, who has granted bioRxiv a license to display the preprint in perpetuity. It is made available under aCC-BY 4.0 International license.

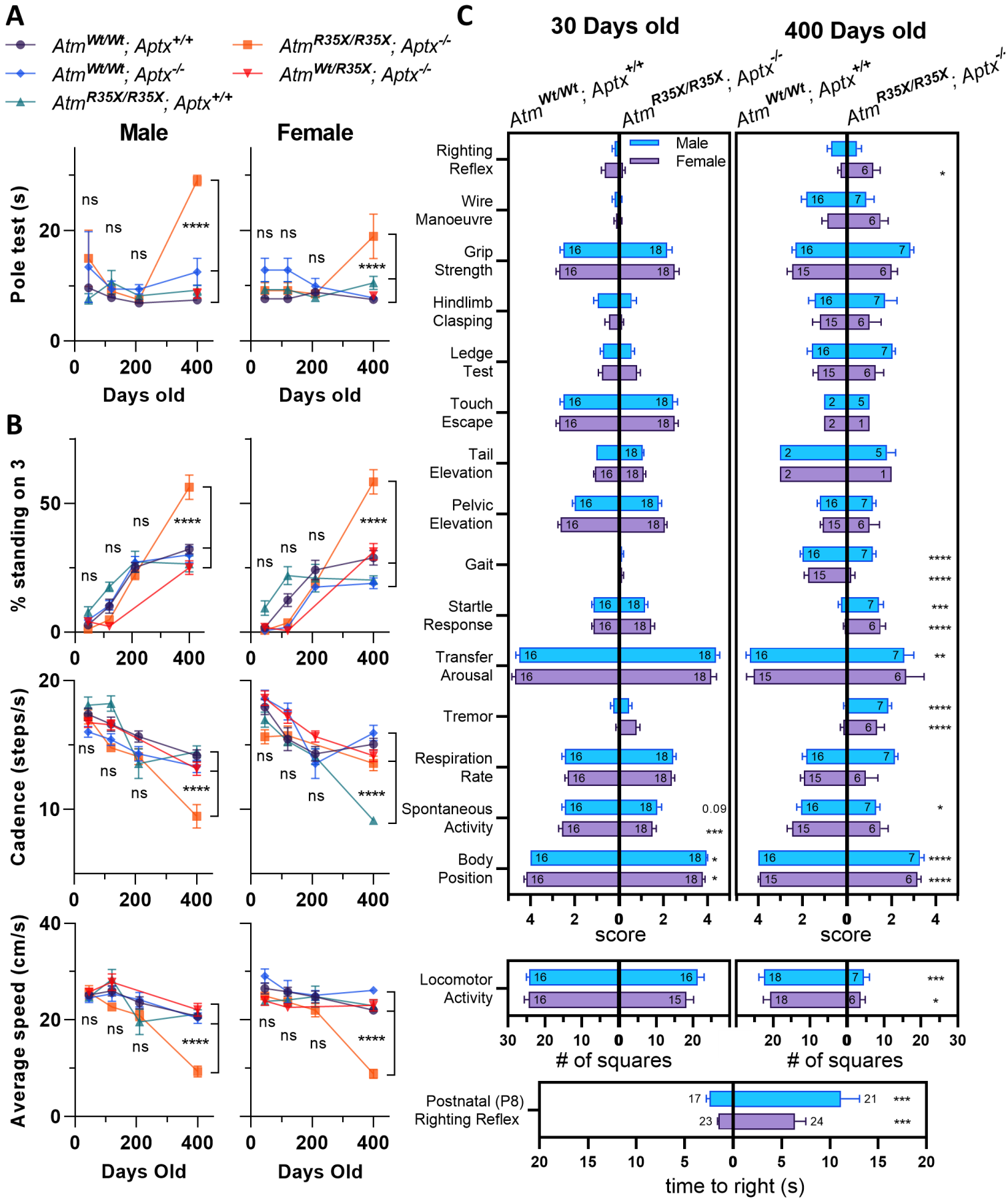

Figure 3-figure supplement 1

bioRxiv preprint doi: https://doi.org/10.1101/2020.11.23.394098; this version posted November 23, 2020. The copyright holder for this preprint (which was not certified by peer review) is the author/funder, who has granted bioRxiv a license to display the preprint in perpetuity. It is made available under aCC-BY 4.0 International license.

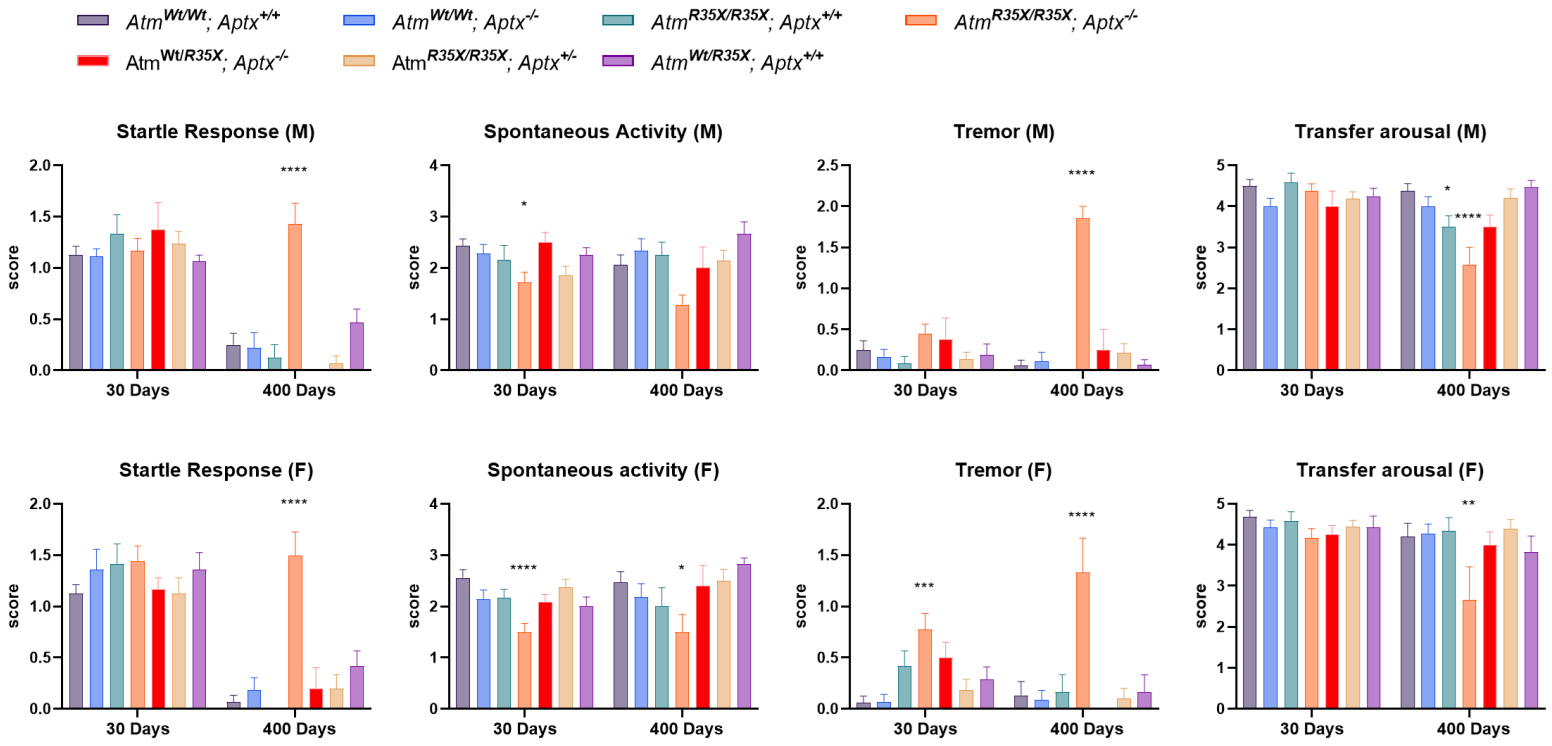

Fig. 4

bioRxiv preprint doi: https://doi.org/10.1101/2020.11.23.394098; this version posted November 23, 2020. The copyright holder for this preprint (which was not certified by peer review) is the author/funder, who has granted bioRxiv a license to display the preprint in perpetuity. It is made available under aCC-BY 4.0 International license.

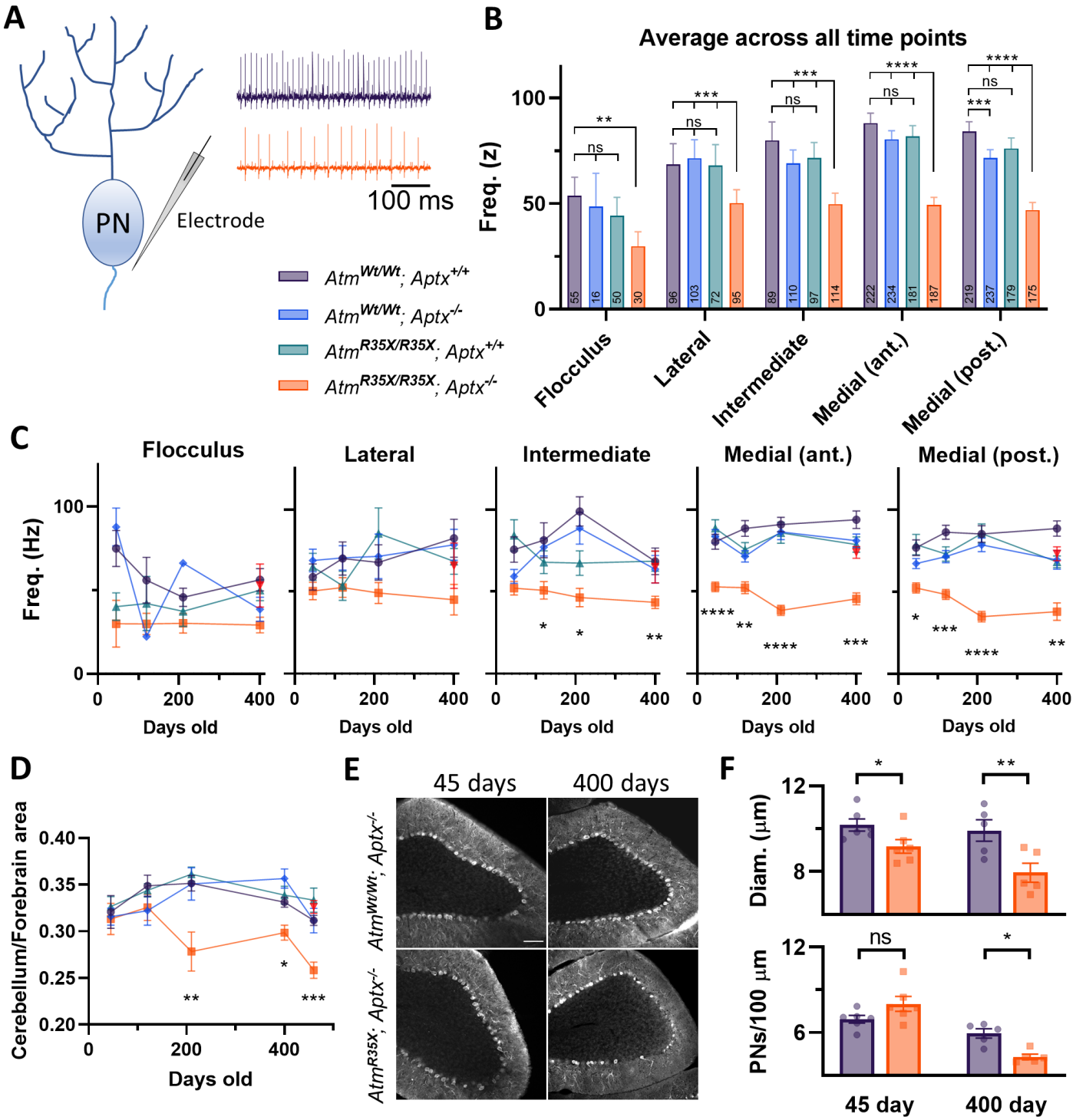

bioRxiv preprint doi: https://doi.org/10.1101/2020.11.23.394098; this version posted November 23, 2020. The copyright holder for this preprint (which was not certified by peer review) is the author/funder, who has granted bioRxiv a license to display the preprint in perpetuity. It is made available under aCC-BY 4.0 International license.

Figure 4-figure supplement 1

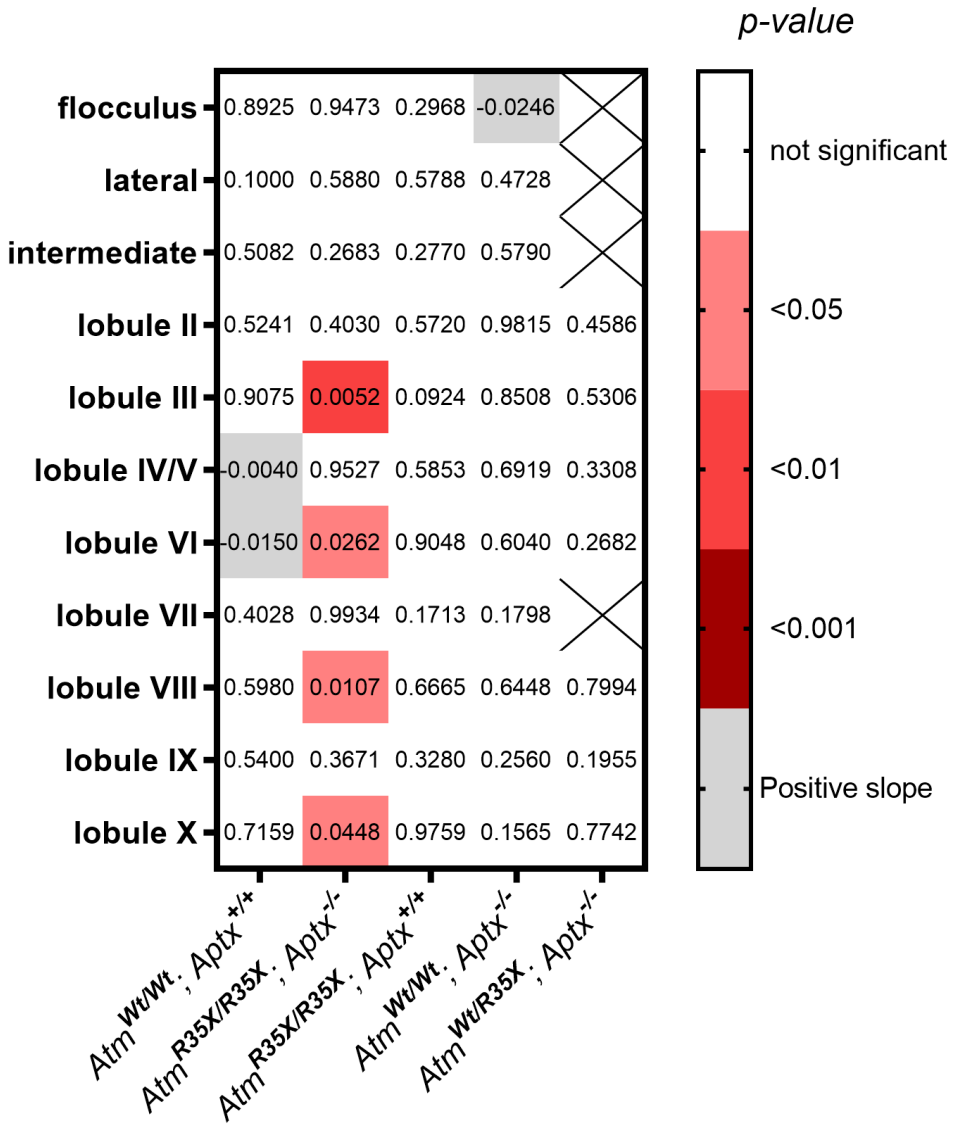

bioRxiv preprint doi: https://doi.org/10.1101/2020.11.23.394098; this version posted November 23, 2020. The copyright holder for this preprint (which was not certified by peer review) is the author/funder, who has granted bioRxiv a license to display the preprint in perpetuity. It is made available under aCC-BY 4.0 International license.

Figure 4-figure supplement-2

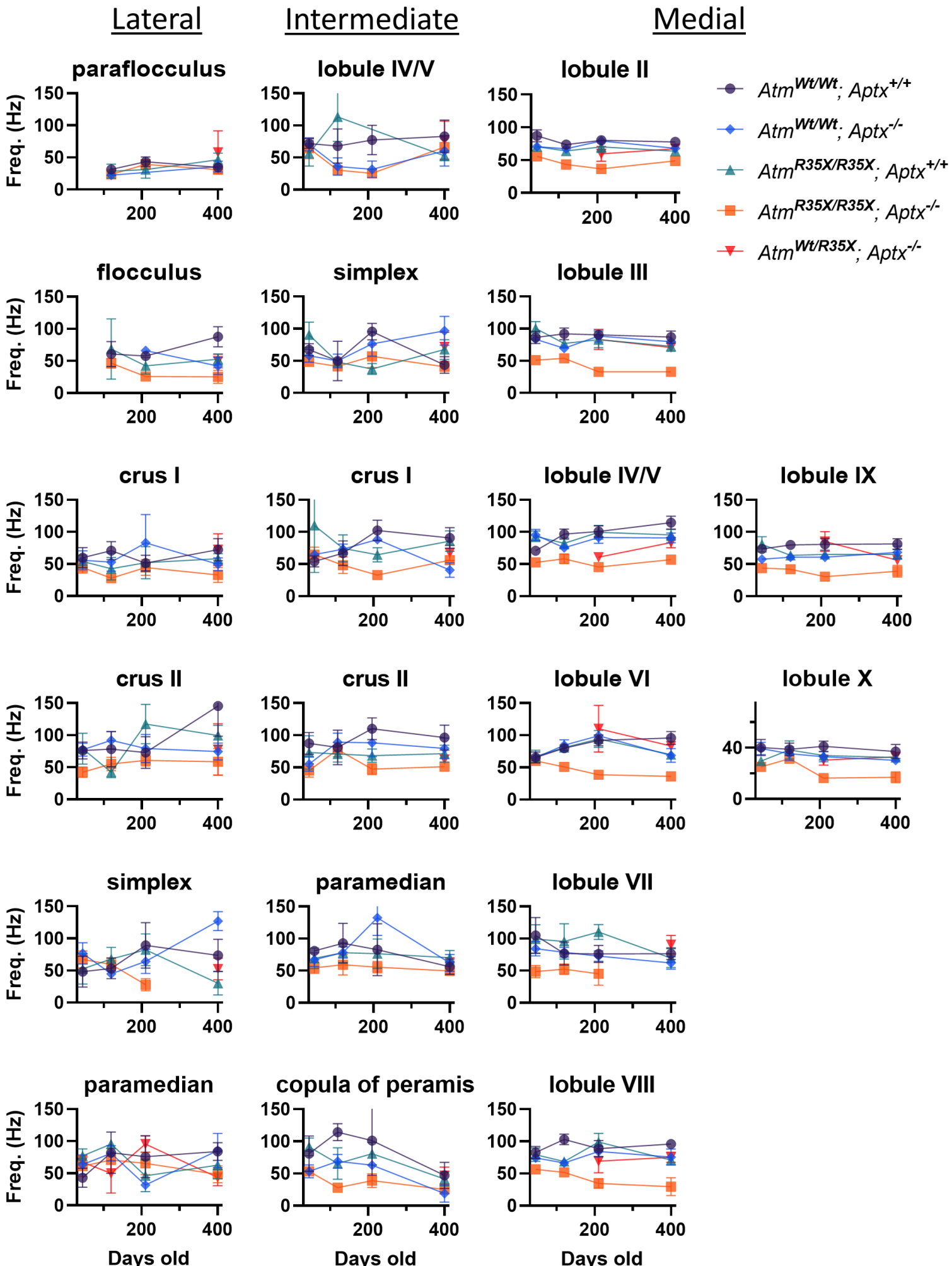

bioRxiv preprint doi: https://doi.org/10.1101/2020.11.23.394098; this version posted November 23, 2020. The copyright holder for this preprint (which was not certified by peer review) is the author/funder, who has granted bioRxiv a license to display the preprint in perpetuity. It is made available under aCC-BY 4.0 International license.

Figure 4-figure supplement-3

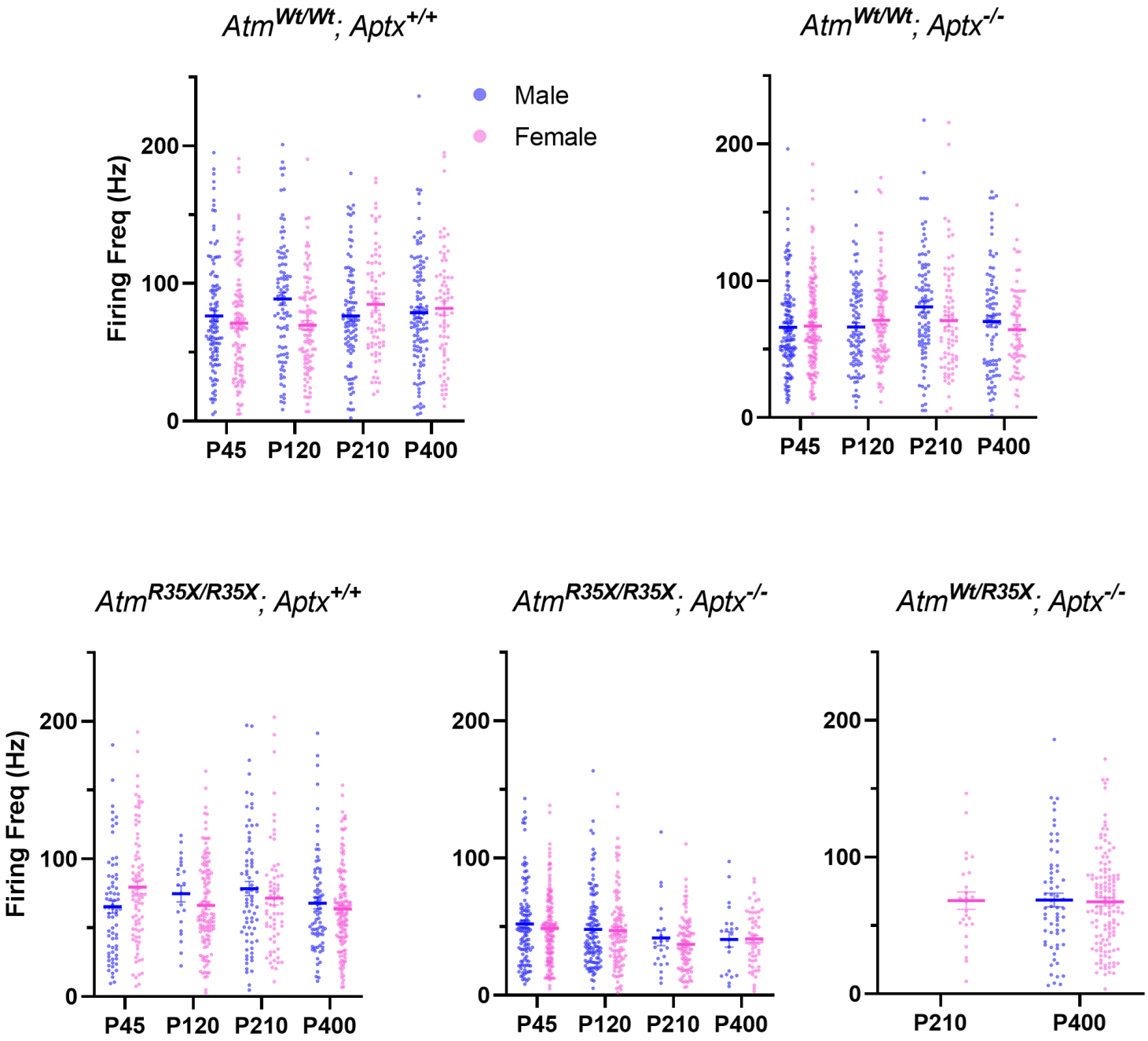

bioRxiv preprint doi: https://doi.org/10.1101/2020.11.23.394098; this version posted November 23, 2020. The copyright holder for this preprint (which was not certified by peer review) is the author/funder, who has granted bioRxiv a license to display the preprint in perpetuity. It is made available under aCC-BY 4.0 International license.

Figure 4-figure supplement 4

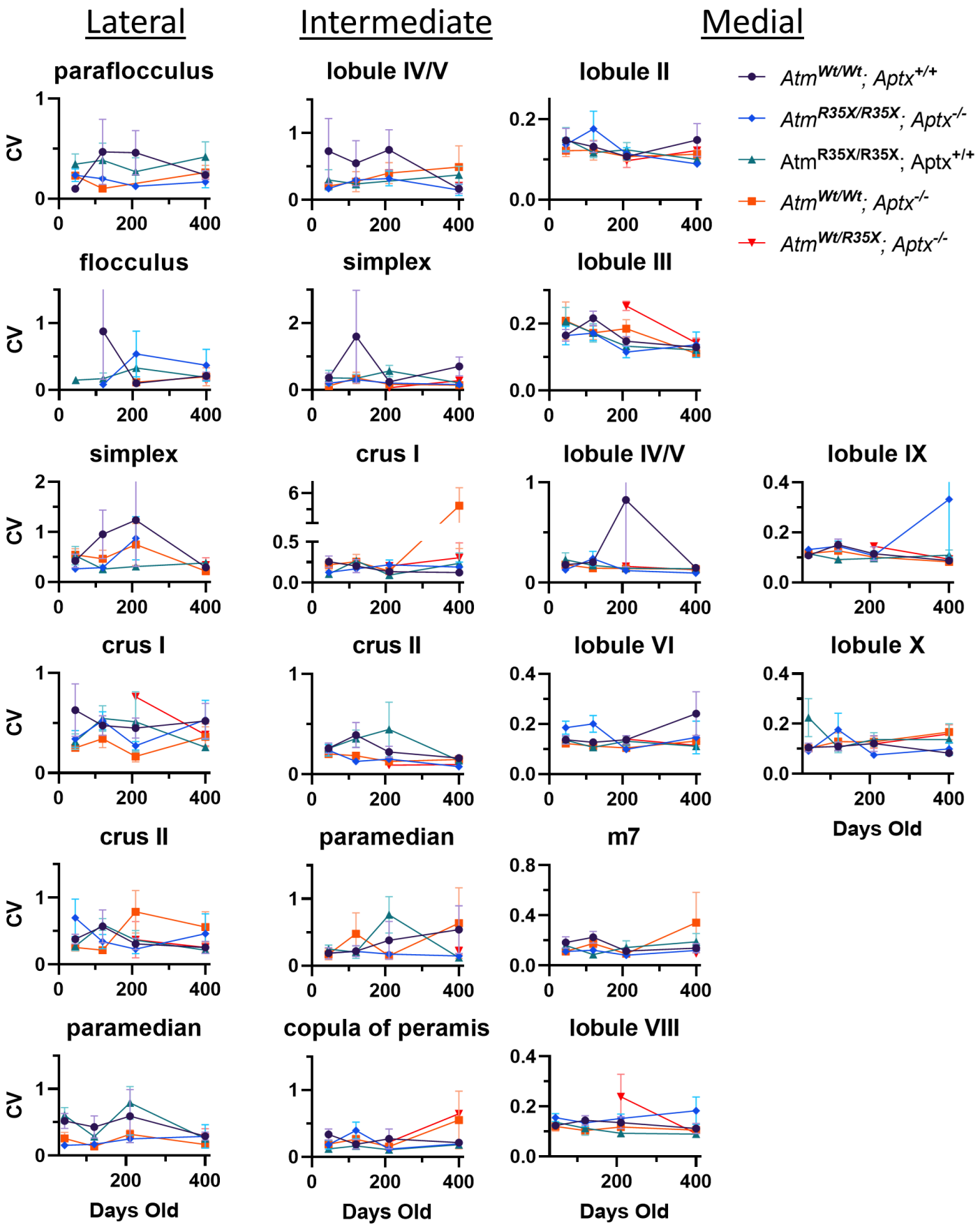

bioRxiv preprint doi: https://doi.org/10.1101/2020.11.23.394098; this version posted November 23, 2020. The copyright holder for this preprint (which was not certified by peer review) is the author/funder, who has granted bioRxiv a license to display the preprint in perpetuity. It is made available under aCC-BY 4.0 International license.

Figure 4-figure supplement 5

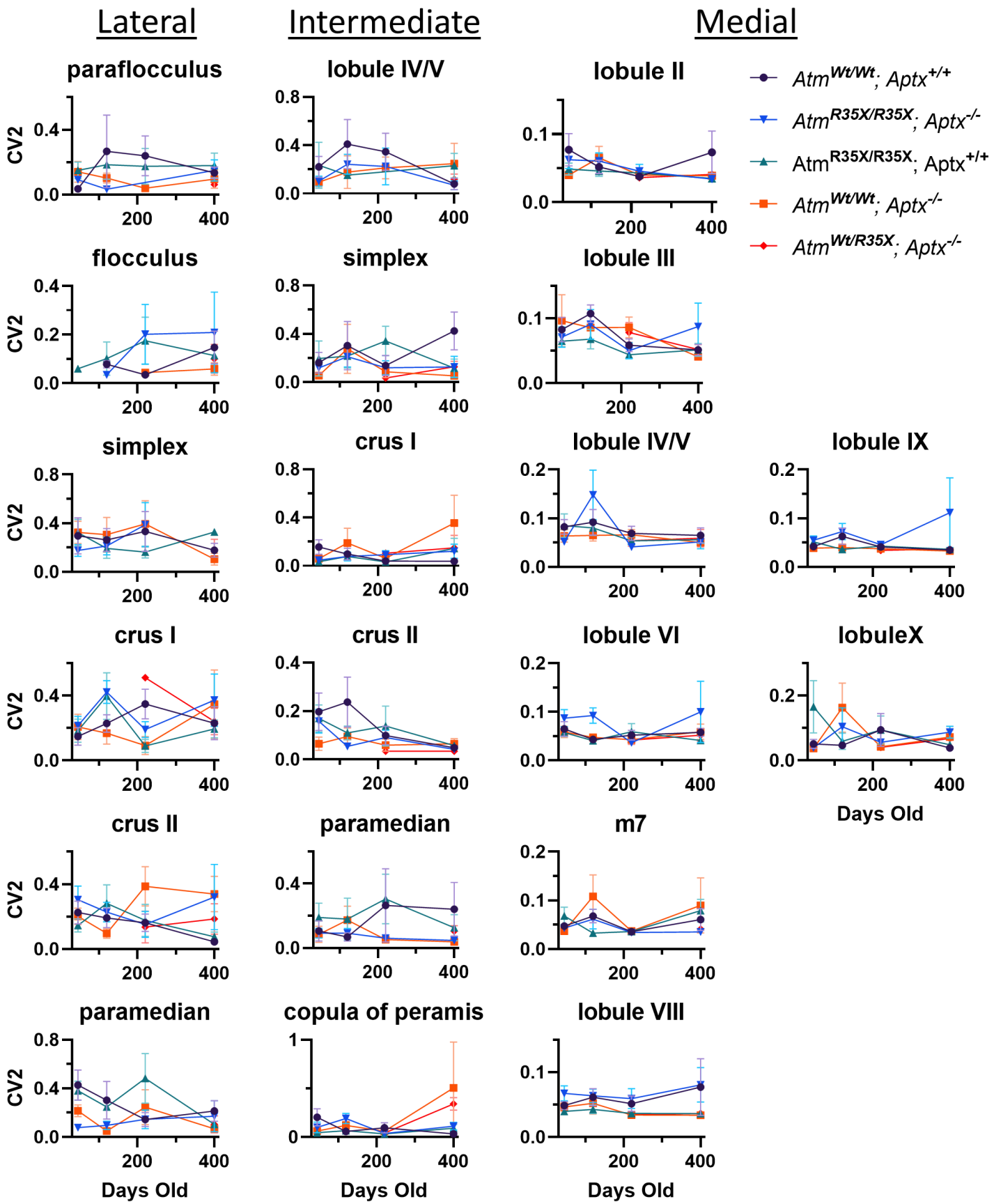

Fig. 5

bioRxiv preprint doi: https://doi.org/10.1101/2020.11.23.394098; this version posted November 23, 2020. The copyright holder for this preprint (which was not certified by peer review) is the author/funder, who has granted bioRxiv a license to display the preprint in perpetuity. It is made available under aCC-BY 4.0 International license.

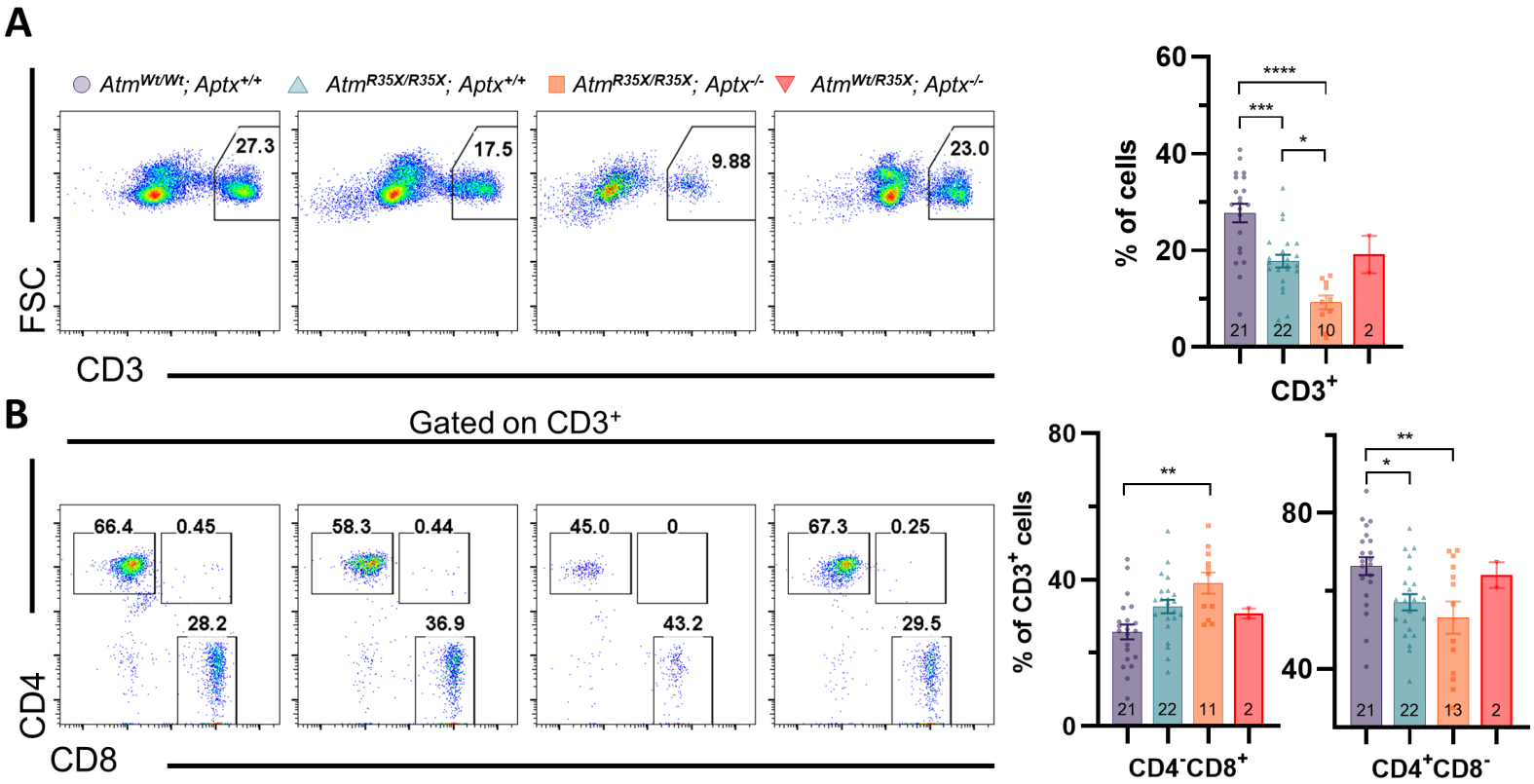

Fig. 6

bioRxiv preprint doi: https://doi.org/10.1101/2020.11.23.394098; this version posted November 23, 2020. The copyright holder for this preprint (which was not certified by peer review) is the author/funder, who has granted bioRxiv a license to display the preprint in perpetuity. It is made available under aCC-BY 4.0 International license.

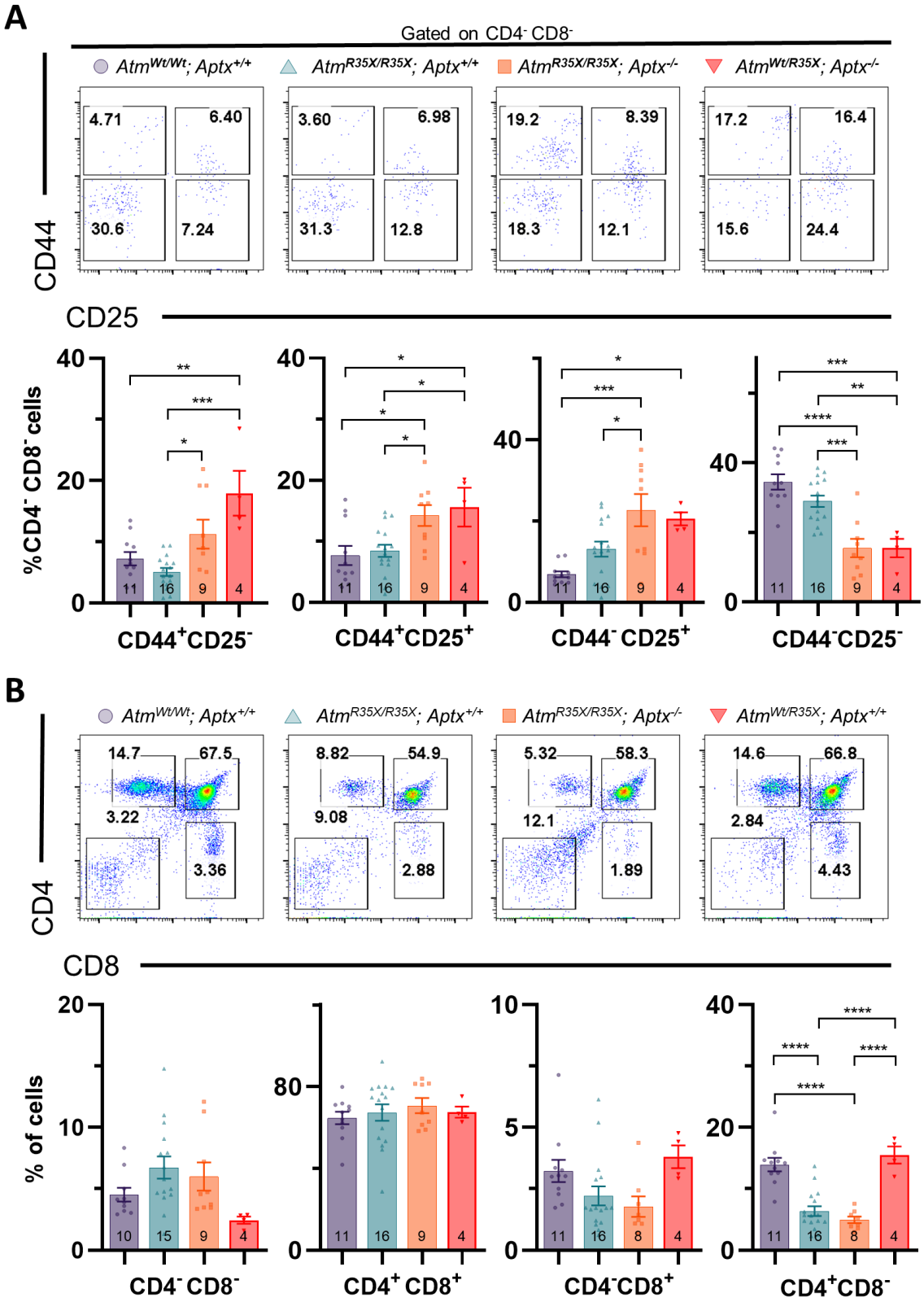

Fig. 7
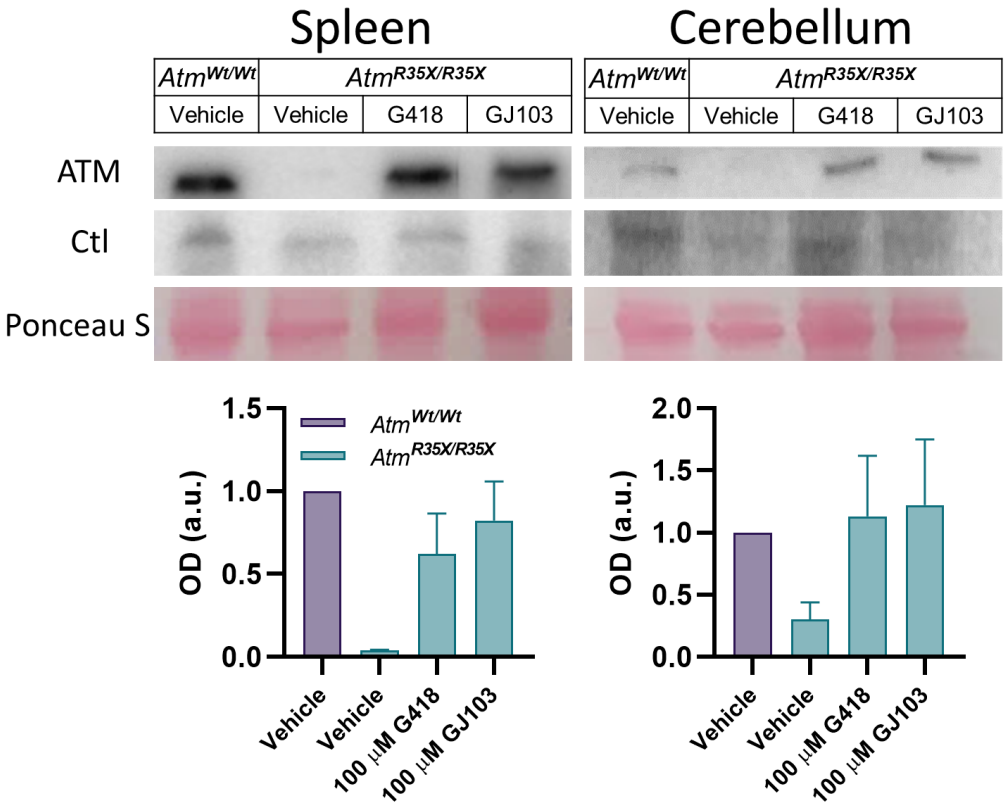
bioRxiv preprint doi: https://doi.org/10.1101/2020.11.23.394098; this version posted November 23, 2020. The copyright holder for this preprint (which was not certified by peer review) is the author/funder, who has granted bioRxiv a license to display the preprint in perpetuity. It is made available under aCC-BY 4.0 International license.